

Route towards an optical dipole trap for single atoms

Author:
Patrick Michelberger
Supervisor:
Dr. Axel Kuhn
Clarendon Laboratory
University of Oxford

Abstract

In this report a route towards setting-up a new kind of single-atom optical dipole trap is developed, including the trapping system and the imaging scheme for the trapped atom. The reliability of the optical part of the set-up has been tested. This includes an detailed experimental study of the capability of the optical system (formed by an aspheric lens, a achromatic doublet and the view- port of the vacuum chamber) to focus the trapping beam and to image small objects back. One testing scheme relies on a reversed beam path through the system, whereas the other one uses the correct illumination direction with a back-reflected beam. No geometrical aberrations are observed, when the focus of the trapping beam is displaced by as much as $45\mu m$ from the optical axis. Effects on the imaging quality, caused by the aspheric lens, are also examined. Ultimately, the changes in the trapping potential due to a beam displacement is modeled.

Contents

1 Declaration concerning intellectual property	3
2 Introduction	4
3 Theory section	5
3.1 Light matter interaction	5
3.1.1 Perturbation of atoms by electromagnetic waves and Rabi oscillations.	5
3.2 Light shift and dressed state picture	7
3.3 The optical forces	8
3.3.1 Dipole force	9
3.4 The optical dipole trap	10
3.4.1 Trapping in the dipole trap	10
3.4.2 Properties of our dipole trap	12
3.4.3 Tasks of project	17
4 Experiments	18
4.1 Experiment 1 - reversed light path	18
4.1.1 Setup and alignment description	18
4.1.2 Advantages and aims	21
4.1.3 Measurements	21
4.2 Experiment 2	29
4.2.1 Setup and alignment description	29
4.2.2 Measurements	38
4.2.3 Trap- potential	48
4.3 Experiment 3	50
5 Conclusions	56
6 Appendix	58
6.1 Mathematical derivation of Rabi- osciallations	58
6.2 Derivation of the light shift	59
6.3 Optical Bloch equations	60

6.4	Derviation of the optical forces	62
6.4.1	Further examination of the optical forces	63
6.5	Cooling mechanisms and magneto-optical trap	65
6.5.1	Doppler cooling	65
6.5.2	Magneto- optical trap (MOT)	66
6.5.3	Polarisation gradient cooling	70
6.6	Loading of optical dipole trap	72
6.7	Diode laser power characteristic	75
6.8	Additional plots for second experimental setup	76
6.8.1	Moving $50 \mu m$ aperture in the transverse plane	76
6.8.2	Displacing aspheric lens along optical axis and restoring focus by collimator movement	86

Chapter 1

Declaration concerning intellectual property

I declare, that this work has been composed by me, and is a record of work done by me, and has not previously been presented for a higher degree. This project was conducted by me at the Clarendon Laboratory (University of Oxford) from the 01/06/2007 to 31/08/2007 towards the degree of MSc in Photonics and Optoelectronic Devices at the University of St. Andrews and Heriot- Watt University under the supervision of Dr. Axel Kuhn.

I confirm that this work submitted for assessment is my own and is expressed in my own words. Any uses made within it of works of other authors in any form (ideas, results, equations, figures, test, tables, programs, etc.) are properly acknowledged at the point of their use.

Chapter 2

Introduction

Quantum computation and information processing is one of the most active research field in quantum optics. A key element is the creation of entangled states between two particles, which can be individually controlled, addressed and read out at the same time. A possible route to that goal is to place a trapped single atom inside a ultrahigh-finesse cavity, e.g. a photonic crystal one or a Fabry-Perot cavity between the tips of two optics fibres. In the cavity, an excited atom predominantly emits photons into the cavity mode. Hence these photons can be used for transmission of information between atoms, located in different cavities. A network of atoms trapped in cavities thus enables an elementary quantum information network.

To manipulate atoms in the desired way, one can use optical tweezers (dipole traps) for single atoms. In the present project, ^{87}Rb will be loaded into a trap from a cloud of cold atoms prepared in a magneto-optical surface trap (MOT). Once loaded into and confined by the dipole trap, it should be possible to move an atom to any desired location by modifying the dipole trap's beam path. In the proceedings of this project, the first steps towards such a device will be taken. In particular, the imaging system will be built and tested, and a way to thoroughly align it to generate the optical tweezers will be found.

The present report is structured as following:

1. A description of the optical tweezers and dipole force trapping of atoms will be provided.
2. The experimental characterisation of the imaging properties of the system will be discussed.
3. A discussion of the feasibility of the dipole trap system will be undertaken wherever appropriate.

Chapter 3

Theory section

3.1 Light matter interaction

For being able to understand trapping and cooling of atoms, as it will be performed in our experiment, one has to be aware of the effects, generate by the atom- light interaction. Since the main text will comprise only the main outcomes of each step of cooling and trapping theory, the appendix deals with the more thorough, mathematical treatment. Furthermore one should also notice straight away, that this report does not intend to provide a theoretical treatment of the basic optics, required for understanding the imaging system. Such a description can be found in most standard optics textbooks, e.g. [6] or [7]. References are given where appropriate.

3.1.1 Perturbation of atoms by electromagnetic waves and Rabi oscillations.

As one considers a closed system, comprising only a single atom, the Schrödinger equation for its electrons can be written as:

$$H|\Phi\rangle = -\frac{p^2}{2m}|\Phi\rangle + V_0|\Phi\rangle = i\hbar \frac{d|\Phi\rangle}{dt}$$

Here $|\Phi\rangle$ is the atomic eigenfunction and V_0 is the potential, generated by the atomic core and the other electrons in the hull. If an electromagnetic light- wave ($\vec{E}(\vec{r}, t) = \vec{E}_0 \cos(kz - \omega_l t)$) is incident on such an atom, its interaction results in a perturbation of the atoms energy levels. This can be described by induction of an electromagnetic dipole moment, whence the additional energy term in the Hamiltonian can be written, as ¹:

$$H'(t) = -e\vec{E}(r, t) \cdot \vec{r} = \hbar\Omega \cos(kz - \omega_l t)$$

$\Omega = -\frac{eE_0}{\hbar} < e|\vec{r}|g >$ is the Rabi- frequency for the atomic transition driven by the light wave ². This perturbation causes a mixture of the eigenstates of the unperturbed atom,

¹For a thorough mathematical derivation of the Ehrenfest theorem and the dipole operator, see [3]

²For a more thorough definition see the first section of the appendix.

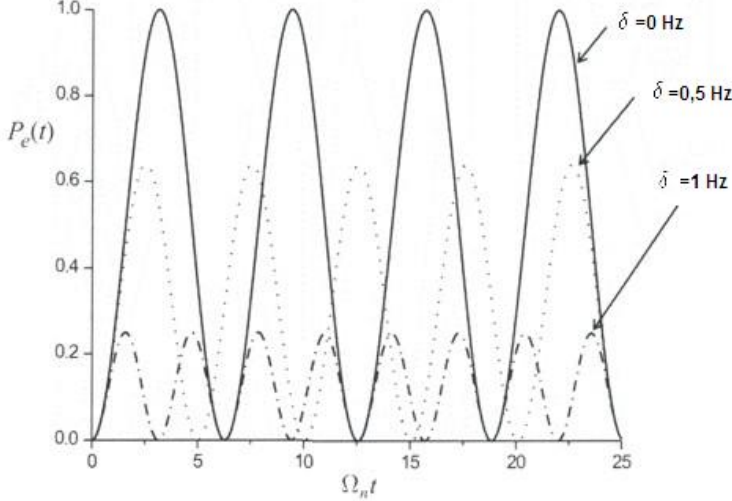


Figure 3.1: Occupation probabilities of a two level atoms due to Rabi- oscillations for different detunings; source: [1].

describable as a linear combination of the unperturbed states. As only a ground ($|g\rangle$) and excited state ($|e\rangle$) are coupled by this excitation, the resulting wavefunction can be written as:

$$|\Psi\rangle = c_g(t)|g\rangle + c_e(t)|e\rangle \quad (3.1)$$

with the appropriate coefficients ³

$$c_g(t) = \left(\cos\left(\frac{\sqrt{\omega^2 + \delta^2}t}{2}\right) - i\frac{\delta}{\sqrt{\Omega^2 + \delta^2}} \sin\left(\frac{\sqrt{\Omega^2 - \delta^2}t}{2}\right) \right) e^{i\frac{\delta t}{2}} \quad (3.2)$$

$$c_e(t) = -i\frac{\Omega}{\sqrt{\Omega^2 + \delta^2}} \sin\left(\frac{\sqrt{\Omega^2 - \delta^2}t}{2}\right) e^{-i\frac{\delta t}{2}} \quad (3.3)$$

$$(3.4)$$

For a thorough derivation of these results, the reader might be referred to the appendix.

One clearly sees these solutions containing oscillations of the excited and ground state populations, which are highly dependent on the lasers detuning δ and the Rabi- frequency Ω . A visualisation of these Rabi- oscillations can be obtained for different detunings in fig: 3.1

In general these oscillations are getting faster, the more the laser's frequency is off the atomic transition. However this also causes a smaller amplitude, as the probability for stimulated absorption and emission is reduced. So choosing a suitable laser frequency for our purposes is a trade- off between oscillation rate and transition strength. As cooling in the MOT will be achieved by stimulated absorption and subsequent spontaneous emission, whereas trapping is

³ $\delta = \omega_l - \omega_a$ is the frequency detuning of the driving laser frequency ω_l and the atomic resonance frequency ω_a .

obtained by stimulated absorption and emission, the rate between the Rabi- frequency and the natural lifetime of the excited state is rather important as well.

Nevertheless the picture introduced so far lacks the major effect of spontaneous emission of the atom. Throughout the remainder of the theory section, the atom will always be referred to as having a clear upper and lower state as well as being situated in either one of these. This requires the atomic wavefunction to be in a pure quantum state, which is not the case, as spontaneous emission mixes the two states ($|g\rangle$ and $|e\rangle$), due its randomness footnotePhotons, emitted that way, are not observed in the experiment.. A thorough description taking care of this effect would claim for the usage of the density matrix method. The reader should be aware of spontaneous emission disturbing the Rabi- oscillations as shown in fig. (3.1), which results in abrupt random transitions from the excited to the ground state.

3.2 Light shift and dressed state picture

The perturbation by the light field also mixes the eigenvalues and eigenstates of the atoms's Hamiltonian, i.e. the energy- levels and electronic wavefunctions of the electrons. This is called light shift, respectively dressed atom state.

As the reader can confirm by looking at the second section of the appendix, the light shift is:

$$\Delta E_{e,g} = \pm \frac{\hbar}{2} \sqrt{\Omega^2 + \delta^2}$$

So even if the light does not cause any excitation ($\Omega = 0$), e.g. by being too far off resonance, there is still a shift in the atomic energy levels apparent. If the detuning is greater than the Rabi- frequency ($\delta >> \Omega$) as in our case, a Taylor expansion results in a light shift of [1]:

$$\Delta E_e = \frac{\hbar\delta}{2} - \frac{\hbar\Omega^2}{4\delta} \quad (3.5)$$

$$\Delta E_g = \frac{\hbar\delta}{2} + \frac{\hbar\Omega^2}{4\delta} \quad (3.6)$$

The MOT laser, as well as the dipole trap laser ($\lambda_{dipole} = 785\text{ nm}$), are red- detuned, i.e. $\delta < 0$, which results in a negative shift of the atomic ground state, and a positive shift of the excited state as can be seen from fig. 3.2.

As the amount of shifting is also dependent on the laser's intensity ($\Omega \sim E \sim \sqrt{I}$), this will have major influence on the properties of the atomic dipole trap. Since atoms generally tend towards a minimization of their potential energy, they will be attracted towards higher intense laser fields. This will turn out to be the main characteristic for trapping atoms.

The coupling of the unperturbed eigenstates of the atom ($|g\rangle, |e\rangle$) by incident laser radiation can also be expressed via a mixing angle Θ , accounting the relevant contributions of the each original state in the eigenfunctions of the new interacting system. These new states are referred to as dressed states and can be written shortly as [1] ⁴:

⁴The exact value of Θ is not important in our context, as these states are only relevant for understanding

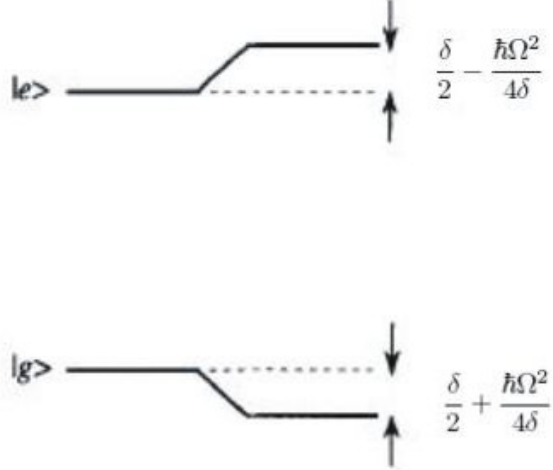


Figure 3.2: Light shift of the ground and excited state of a two level system in an electromagentic field for negative detuning $\delta < 0$; source: [1].

$$|\Phi\rangle_1 = \cos\Theta|g\rangle - \sin\Theta|e\rangle \quad (3.7)$$

$$|\Phi\rangle_2 = \sin\Theta|g\rangle + \cos\Theta|e\rangle \quad (3.8)$$

3.3 The optical forces

According to classical mechanics, the force on a particle is the time derivative of its change in momentum

$$F = \frac{d}{dt}p$$

Considering Ehrenfest's theorem, the quantum mechanical expectation values have to fulfill the same relations as the classical variables. This results the expectation value of the force operator to equal the time derivative of the momentum operator. In our experimental set-up, we are only concerned about observables, we can treat the measured force on an atom as the expectation value of its operator:

$$F = \langle \hat{F} \rangle = \frac{d}{dt} \langle \hat{p} \rangle$$

Using the formula for the time derivative of the expectation value of a time independent operator [3], we obtain for the momentum operator:

$$\frac{d}{dt} \langle \hat{p} \rangle = \frac{i}{\hbar} \langle [\hat{H}, \hat{p}] \rangle = \frac{i}{\hbar} i\hbar \langle \nabla \hat{H} \rangle$$

Resulting in:

sub- Doppler cooling, but no quantitative analysis is based on them through the reminder of this report.

$$F = - < \nabla \hat{H} >$$

So the force on an atom in a light field is the negative gradient of the interaction potential, caused by the light- atom interaction. For the dipole- interaction Hamiltonian $\hat{H}' = -e\vec{E}(\vec{r}, t) \cdot \vec{r}$, this provides a force term of ⁵:

$$F = e\nabla < \vec{E}(\vec{r}, t) \cdot \vec{r} >$$

As shown in the fourth section of the appendix, this force consists of two different components:

$$F_1 = \frac{\hbar\delta\omega}{2(\delta^2 + \frac{\Omega^2}{2} + \frac{\gamma^2}{4})} \frac{\partial\Omega}{\partial z} \quad (3.9)$$

$$F_2 = \frac{\hbar k\gamma\omega^2}{4(\delta^2 + \frac{\Omega^2}{2} + \frac{\gamma^2}{4})} \quad (3.10)$$

The first one (F_1) is conservative and due to a potential; it is the force an optical dipole trap relies on. The second (F_2) is due to scattering of photons ⁶. These two forces are examined a bit further in the appendix.

3.3.1 Dipole force

Looking at $F_1 = \frac{\hbar\delta\omega}{2(\delta^2 + \frac{\Omega^2}{2} + \frac{\gamma^2}{4})} \frac{\partial\Omega}{\partial z}$, one can see, that it vanished for entirely fulfilling the resonance condition $\omega_l = \omega_a$, i.e. $\delta = 0$. However, if the laser is considerably detuned from the natural linewidth of the atomic transition used ($\delta \gg \gamma$) as well as the detuning being of much higher frequency than the Rabi- oscillations within the atom ($\delta \gg \Omega$), one can simplify the expression above, yielding [1]:

$$F_1 = \frac{\hbar\Omega}{2\delta} \frac{\partial\Omega}{\partial z} = \frac{\partial}{\partial z} \left(\frac{\hbar\Omega^2}{4\delta} \right)$$

The expression in the last bracket exactly equals the one for the light shift (eq: 3.5,3.6) hence:

$$F_{dipole} = \frac{\partial}{\partial z} (\Delta E_{e,g})$$

As discussed already, red- detuned light causes the ground state of the atom to be lowered in energy- terms (vice versa for the excited) for higher intensity fields. This causes the gradient of the energy shift for the ground state to be negative, hence the dipole force F_{dipole} points into the direction of lower energy, pushing the atoms to the position of highest laser intensity.

Hence the atoms get trapped within a well- type potential, caused by the light shift of the laser radiation in a standing wave. So a standing wave laser beam acts like a trapping device,

⁵Here the slowly varying envelope approximation is used, i.e. the variation of the electric field over the dimensions of an atom are neglected, hence the derivative can be taken out of the expectation value.

⁶i.e. stimulated absorption and subsequent spontaneous emission

causing potential wells to occur at its antinodes, in which atoms can get trapped. However trapping is also a question of the well depth and the kinetic energy of the atoms of course. As these wells cannot be made deep enough to trap e.g. Doppler cooled atoms, a sophisticated cooling scheme has to be developed first in order to cool atoms down on a micro K scale, enabling this type of trap to work.

Furthermore the reader should note, that $F_{dipole} \propto \gamma$, i.e. this type of force is not dependent on spontaneous emission. The last point is clearly obvious, since the light shift is caused by stimulated absorption and emission⁷ and therefore no resulting momentum is transferred from the light field onto the atom. This in turn causes the dipole force not to act as a cooling force, since kinetic energy of the atomic motion is not dissipated, thus the dipole force is a conservative force. So with it, the phase space density of atoms cannot be changed, i.e. atoms cannot be cooled but therefore trapped only, as this kind of force is strongly position dependent ($f_{dipole} \sim \frac{\partial \Omega}{\partial z}$). Due to these properties, the atomic ensemble in our experiment is first cooled by the MOT and the atoms are subsequently loaded into the dipole trap, once they are cold enough.

3.4 The optical dipole trap

3.4.1 Trapping in the dipole trap

In the section about the optical forces and the appendix, it has been shown, that the light shift causes a potential landscape to occur (eq. 6.4.1). This can be simplified using the following expression for the Rabi- frequency (see [1]):

$$\Omega = \gamma \sqrt{\frac{I(\vec{r})}{2I_{sat}}}$$

I_{sat} is the saturation intensity for the atomic transition involved in the light shift. For our purposes, this transition is the $5S(F=2) \rightarrow 5P(F=3)$ at a wavelength of $\lambda_a = 780,24\text{ nm}$, having a saturation intensity of $I_{sat} = 3,576 \pm 0,004 \frac{\text{mW}}{\text{cm}^2}$ and an upper state lifetime of $\tau_e = 27,7\text{ ns}$, hence an upper state natural linewidth of $\gamma \approx 36,1\text{ MHz}$.

This results gives an expression for the dipole force of (see eq. 3.10):

$$F = -\frac{\hbar\gamma^2}{8\delta I_{sat}} \nabla I(\vec{R})$$

For the experiment, we will use the 0^{th} order laser mode of a diode laser, hence the relevant intensity profile can be expressed as⁸ $I(\vec{r}) = I_0 e^{-\frac{r^2}{w(z)^2}}$, resulting in a force [1]:

$$F = \frac{\hbar\gamma^2}{4\delta} \frac{I_0}{I_{sat}} \frac{r}{w_0^2} e^{-\frac{r^2}{w(z)^2}} \quad (3.11)$$

⁷i.e. exchange of photons between laser field and atom, sustaining the direction of emission and coherence

⁸ z is the direction of beam propagation in this case.

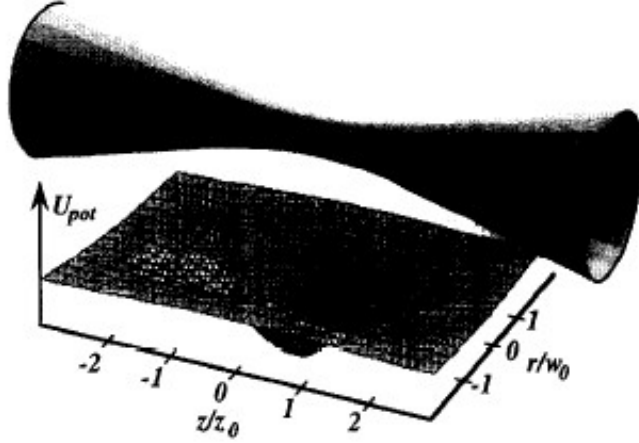


Figure 3.3: Focussing of a Gaussian beam for creating a dipol trap, from ref. [8]

This conservative force pushes the atoms towards the regions of highest intensity in the laser beam, if the light is red-detuned (here: $\lambda_l = 785 \text{ nm} \rightarrow \delta \approx 5 \text{ nm}$), therefore trapping them. For a Gaussian profile, the trapping region is formed on the optical axis at the focus of the beam, as shown in fig: 3.3.

The light shift lowers the ground state energy, since (see 3.6) the energy shift is proportional to the intensity, $\Delta E_g \sim \frac{\hbar\Omega^2}{4\delta} = -\frac{\hbar\gamma^2 I(\vec{r})}{8|\delta|I_{sat}}$. This results in the creation of a 3-dimensional potential well around the focus of the Gaussian laser beam (visible in fig: 3.3 as a pit): Quite obviously the intensity decreases as one leaves the centre of the Gaussian intensity distribution, therefore causing smaller light shifts off-axis, resulting in a shallower trapping potential. Longitudinally (i.e. along its propagation direction) we can have two effects, leading towards the creation of a confinement potential. Either there is a standing wave configuration resulting in a node-anti-node structure with a maximum in trap depth at an anti-node, hence comprising a periodicity of $\lambda_l/2$; or the divergence of a Gaussian beam itself can create an intensity decrease as one moves off the minimum beam waist w_0 . As the Gaussian beam waist develops according to [11] $w(z) = w_0 \sqrt{1 + (\frac{z}{z_0})^2}$, the intensity of axis $I(\vec{r}) = I_0 e^{-\frac{r^2}{w(z)^2}}$ decreases as well by moving out the focus. So as the intensity gets smaller, also the light shift does, leading to a potential pit along the direction of propagation. Both possibilities will be applied in our final setup, although the second way will contribute most ⁹.

A quantitative expression for the potential landscape of the ground state is given by:

$$U = \Delta E_g = -\frac{\hbar|\delta|}{2} - \frac{\hbar I(\vec{r})}{8\tau_e^2 |\delta| I_{sat}} \quad (3.12)$$

As the created potential wells are not very deep, atoms have to be cooled by the MOT to the micron Kelvin regime, before they can successfully be loaded into the dipole trap. Hence both cooling mechanisms in the MOT (see appendix) have to be applied in order to create a useful

⁹A more detailed discussion will be offered in the next subsection.

atomic ensamble for our purposes. Therefore atoms previously cooled and trapped in the MOT have to be loaded into the dipole trap, which will be tried by the simple means of simultaneous switching off the former and switching on the latter in first instance. However precisely loading atoms into a dipole trap is generally not an easy task ([12], [13], [14]), therefore the reader can find a short section about this topic in the appendix ¹⁰. Once atoms are transferred by the aforementioned means, one will probably end up with several atoms loaded into the potential well at the focus of the dipole trap. By using a digital mirror device (DMD), the focal point size can subsequently be scaled down ¹¹, also a division of the trap is feasable, both leading to a decrease in atom number per trap. If one starts with several traps and applies division and tightening of the foci, there might be the possibility of obtaining one trap, confining a single atoms. As the atomic floorescence will be imaged via a CCD camera (see fig: 3.4), a distinction between the number of trapped atoms will be obtainable via intensity and frequency of emission (e.g. as done in [5], [14]). In the case of too low/ strong loading rates or inconvenience of the aforementioned process, we can still try to engineer the loading process by variation of the trapping parameters ¹², or attempt to reach the collisional blockade regime (see appendix and [5], [13], [14]).

3.4.2 Properties of our dipole trap

Once an atom will be trapped at the focus of the laser beam, it must be possible to move it around, which corresponds to variation of the focus in a transverse plane parallel to the mirror surface. We try to achieve this by implementing a digital mirror array (DMD), consisting of small facet mirrors of $13,6\mu m \times 13,6\mu m$ in size (see fig. 3.4). These mirrors can be addressed by computer control individually, having two possible arrangements; either reflecting the beam through the imaging optics into the vacuum chamber building the dipole trap (on state), or reflecting the beam into a cavity dumb (off state). In order for the imaging to work properly ¹³, the mirror plane of the DMD has to be perpendicular to the optical axis, defined by the imaging system; as furthermore the mirrors from the DMD act as a diffraction grating, one desires to only pick up the 0^{th} order in interference. Therefore the DMD has to be illuminated by an angle of $\Phi_{on} = 22\text{ deg}$ to its normal, resulting in on- positioned mirrors reflecting light into the system, parallel to its optical axis, and off- positioned mirrors reflecting the light into the beam dump ($\Phi_{off} = 44\text{ deg}$).

The imaging system itself consists of a collimator lens (an achromatic doublet), having a focal length of $f_c = 750\text{ mm}$ and a diameter of $d_c = 59,8\text{ mm}$ [15] and an aspheric lens of effective focal length $f_a = 12\text{ mm}$ and diameter of $d_a = 15\text{ mm}$ [16], mounted into the vacuum chamber of the MOT.

The imaging optics is set- up as a 2f- system, i.e. the DMD is placed in the back- focal point

¹⁰dealing further with the dependencies on the trapping parameters and the number of atoms loaded

¹¹by simply changing the imaged object on the DMD

¹²according to the dependencies stated in the appendix

¹³Avoiding multiple foci by having a tilted object.

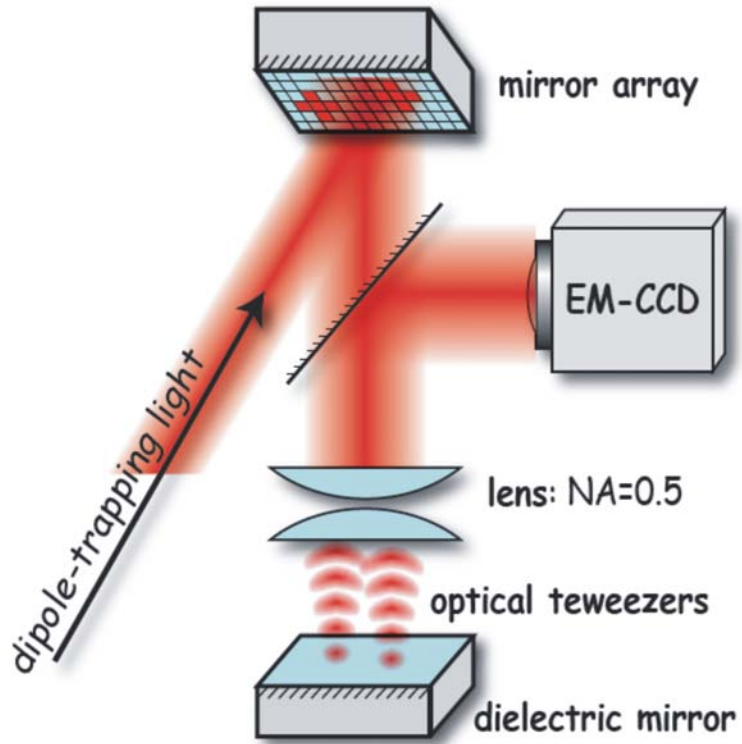


Figure 3.4: Sketch of final setup for dipole trap, including DMD, imaging and observation optics.

of the Collimator, resulting in parallel light beyond it, for the purpose of being send into the vacuum chamber through a viewport. Inside the vacuum chamber, the light is impinging onto the aspheric lens, being focussed close to the surface of the dielectric mirror on the bottom of the MOT (see fig: 3.5). The initial design of the system was done within a previous MPhys project previous using Zeemax.

Appropriately aligned, the system comprises a magnification of [6] $M = \frac{f_a}{f_c} = \frac{1}{62,5} = 0,016$. To be able to create a single atoms trap, a beam waist on focus close to the diffraction limit is desired [5], so something around $w_0 \approx 1 \mu\text{m}$ would be favourable. Therefore we will finally be using a $50 \mu\text{m}$ circle on the DMD¹⁴ in order to create one dipole trap well, having a waist of

¹⁴This circle consists of 12 pixels on the DMD.

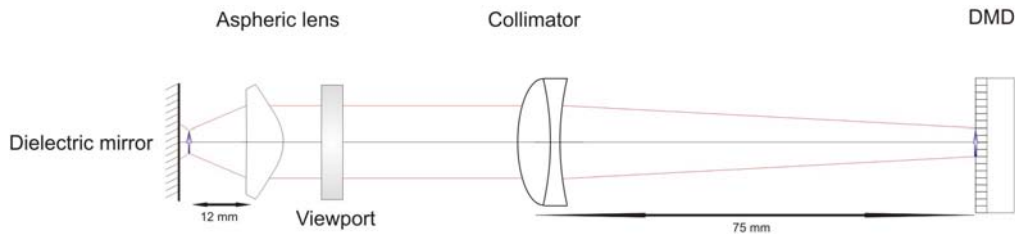


Figure 3.5: Dipole trap imaging system in its 2f configuration with associated ray path. The focus is placed slightly above the dielectric mirror in order to be within the cooled atom cloud.

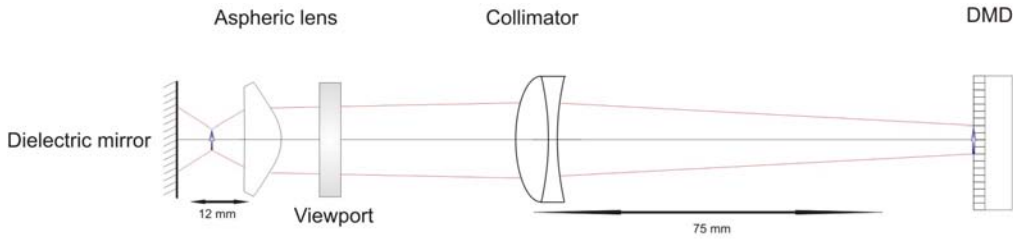


Figure 3.6: Optical dipole trap system with DMD moved further away from collimator than its focal length, causing convergent light between aspheric lens and collimator,a shorter image distance as well as a larger image.

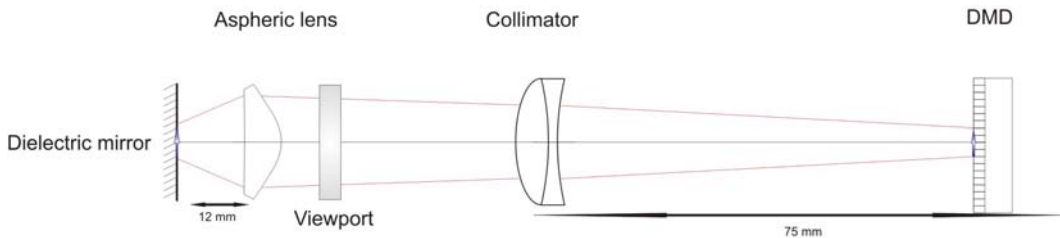


Figure 3.7: Optical dipole trap system with DMD moved closer to collimator than its focal length, causing diverging light between aspheric lens and collimator and a longer image distance but approximately the same, diffraction limited image size.

$0.8 \mu m$. As the DMD's mirror area is $2 \times 2 cm$ in size, several circular images can be displayed next to each other and so many dipole traps can be created, enabling one to trap multiple atoms and move them around independently.

Since the illuminating beam will have a wavelength of $\lambda_l = 785 nm$, this is around the diffraction limit, so physical optics will be important for understanding the system. Therefore the beam path is chosen to penetrate through the viewport collimated, so that its wavefront does not get distorted. However one interesting aspect of this project will be to find out, by how much this condition can be violated, without distorting the image. Such a property of the system is desired, as it gives one the opportunity to displace the trap along the optical axis and to change the altitude of trapped atoms later on. Since the aspheric lens will be fixed in position, a variation of the focal point can only be obtained by displacing the collimator along the optical axis (fig: 3.5), resulting in creation of a real or virtual image and hence converging or diverging ray paths beyond it. In the former case, the focus of the system will be further above the mirror surface (see fig: 3.6) and of greater size¹⁵, whereas in the latter the focus will be closer to the mirror surface (see 3.7), although the magnification will not decrease greatly in this case, as the image is diffraction limited.

The focus of the system will initially not be placed on the mirror surface, since atoms shall be trapped favourably within it, so it must be positioned within the atomic cloud. As this one

¹⁵As the magnification $M = \frac{\text{image distance}}{\text{object distance}}$ gets smaller with increasing object distance and decreasing image distance.

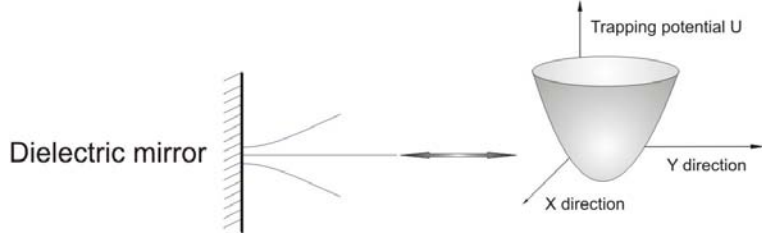


Figure 3.8: Gaußian beam focus on mirror surface, resulting in a complete standing wave geometry and an unperturbed potential well.

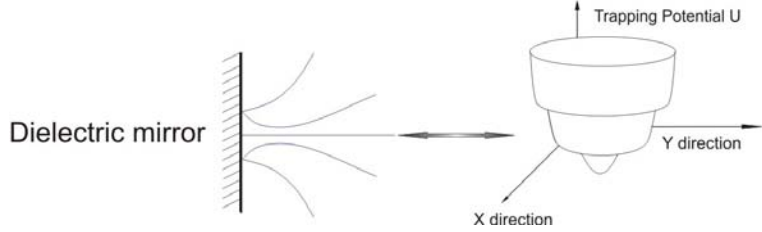


Figure 3.9: Gaußian beam focus slightly above mirror surface, creating a partial standing wave and leading to a potential well showing "sub-pits".

has an altitude of at least $h = 100 \mu m$ above the dielectric mirror, the distance between the aforementioned and the focus of the beam will be greater than the Rayleigh range $z_R = \frac{\pi w_0^2}{\lambda}$ of the beam. If we consider for convenience¹⁶ a minimum beam waist of $w_0 = 1 \mu m$, we will arrive at a Rayleigh range of $z_R(\lambda = 785 nm) \approx 4 \mu m$ ($z_R(\lambda = 780 nm) \approx 4 \mu m$)¹⁷. As the beam hits the dielectric mirror, it will have a waist of $w(z = 100 \mu m) = 25 \mu m$, according to [11]:

$$w(z) = w_0 \sqrt{1 + \left(\frac{z}{z_0}\right)^2} \quad (3.13)$$

Reflected back, it will have a waist of $w(z = 200 \mu m) = 50 \mu m$ at the former position of minimum waist¹⁸ and therefore having only a small overlap with the incident beam. In the ideal case of the beam waist placed on the mirror surface, the overlap would be 100 percent, resulting in a complete standing wave geometry and thus a longitudinal potential well width of $\lambda/2$ (see fig: 3.8). The apparent case however only established a partially standing wave, resulting in a potential pit, formed longitudinally by the divergence of the Gaußian beam, offset by the fractional overlap of both beams. A sketch of the beam path and resulting potential is given in fig: 3.9, showing little "sub- pits" in the main potential well.

As these sub- pits are created by a partial superposition of the incident and the reflected wave, we can quickly calculate the approximate depth at the centre of the trap, which is deeper

¹⁶As the magnification is quite critical to the aspheric lens- dielectric mirror distance, we consider a slightly larger minimum beam waist in order to account for a small range of unavoidable misalignment.

¹⁷In the experimental part, we will use a test laser of $\lambda_l = 780 nm$ wavelength instead of the $\lambda_l = 785 nm$ used in the actual experiment.

¹⁸Here it is assumed, that the entire beam is reflected at the front surface of the mirror, which is not true for a dielectric mirror stack.

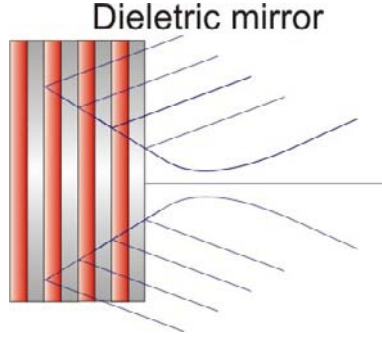


Figure 3.10: Partial reflection of Gaussian beam at different layers of dielectric mirror.

than without reflection. The intensity of a Gaussian around its centre is given by [11]:

$$I(r, z) = I_0 \left(\frac{w_0}{w(z)} \right)^2 e^{-\frac{2r^2}{w^2(z)}} \quad (3.14)$$

Resulting in a central intensity in back- reflection (at the minimum waist position) of $I(r = 0, z = 200 \mu m) = \frac{1}{2500} I_0$. Having a incident electric field strength E_0 at $z = 0$, the electric field in back- reflection will be [11]:

$$\frac{c\epsilon_0}{2} E_1^2 = \frac{c\epsilon_0}{2} \frac{E_0^2}{2500} \quad (3.15)$$

$$E_1 = \frac{1}{50} E_0 \quad (3.16)$$

Hence the superposition of the back-reflected with the incident wave has a field strength of $E_{tot} = E_0 + E_1 = \frac{51}{50} E_0$, resulting in an intensity of $I_{0,tot} = 1 \frac{101}{2500} I_0$ and an additional intensity in the centre of $\Delta I_0 = \frac{101}{2500} I_0$. Therefore, as the trapping depth $U \sim I$, we gain an relationship of the additional potential ΔU to the incident on U_0 of: $\frac{\Delta U}{U_0} = \frac{101}{2500} = 0,0404$. The complete well depth in centre turns out to be:

$$U_{tot} = U_0 + \Delta U = 1,0404 U_0 \quad (3.17)$$

Comparing this to the standing wave case, with a field amplitude of $E_{tot} = 2E_0$ and an intensity of $I_{tot} = 4I_0$ on focus, the trapping potential obviously decreases recognisably by only having a partially standing wave: so later on we desire to move the atoms as close to the mirror surface as possible. This apparent effect will be reduced by the layer structure of the mirror, resulting in a partial reflection from every second layer (see fig: 3.10).

Throughout this report we stick to the assumption of imaging a 0^{th} order Gaussian beam. In the first two experimental setups, we will generate the object by diffraction from an aperture, therefore the impinging intensity distribution on the system will be an Airy pattern, $I \sim \frac{\sin^2(x,y)}{(x,y)^2}$, instead of $I \sim e^{-\frac{(x,y)^2}{w_0^2}}$. In the last setup, we will reflect a Gaussian laser beam from a microscopic object on the DMD, thus having a superposition of both intensity distributions. Despite this, we will stick to the common approximation of the central lobe of the Airy function being approximately describable by a Gaussian [11].

3.4.3 Tasks of project

The overall questions the project are twofold: First, we desired to find out, how exactly the imaging system behaves; i.e. how e.g. the waist of a $50\mu m$ object (as it is used later for creating a single dipole trap) changes as it is imaged by our system. Therefore we examined the system by displacing the object in its transverse plane¹⁹. Furthermore we checked the effects of slight defocussing (alike fig. 3.6, 3.7) by aspheric lens displacements on both parameters stated above. In the last days of the project, we also tried the complete experimental setup²⁰, providing interesting outcomes. The other major issue of the project was the practical examination of its alignment. As later on, the aspheric lens will be at a fixed position inside the vacuum chamber, displacement along the optical axis or tilts can only be cured by movement of the collimator. Especially since the alignment and illumination of the DMD is very critical to its angle, the collimator will be the only degree of freedom. So we checked the required movements of the collimator for certain aspheric lens defocusings. Also tilts of the aspheric lens have been examined and an alignment procedure was found, which opens up the path to installment of the dipole trap into the MOT setup in the near future.

¹⁹Object plane \perp to optical axis given by imaging system.

²⁰i.e. including the DMD

Chapter 4

Experiments

In this chapter we will state the three experimental setups built during this project; we will justify their use for our purposes, explain the alignment, provide the measured data and discuss the latter. For all experiments we relied on a diode laser [17] with a wavelength of $\lambda = 780\text{ nm}$ and a maximum power of $P_{max,780} = 120\text{ mW}$, which is 5 nm shorter than the one used in the final setup.¹

4.1 Experiment 1 - reversed light path

4.1.1 Setup and alignment description

Our first testing setup is based on a reverse² in the desired beam path (see fig. 3.5). Therefore the laser beam is focused through a $d_a = 1\text{ }\mu\text{m}$ aperture, which is placed in the focal point of the aspheric lens. Light collimated by this lens subsequently impinges on the collimator and gets focussed on a CCD camera [18], positioned at the focal point of the latter. In order to create a suitable illuminating beam, the output of the laser is reshaped by an anamorphic prism pair and focussed onto the aperture by an illumination lens [19] ($f_i = 30\text{ mm}$, $d_i = 25,4\text{ mm}$). The real setup can be seen in fig: 4.1 and a schematic figure is shown in fig: 4.2

The output of the diode laser beam after reshaping with the anamorphic prism pair, had resulting divergence angles of $\theta_x^+ = (18,53 \pm 0,03) \cdot 10^{-3}\text{ deg}$ in positive x- direction, $\theta_x^- = (-9,96 \pm 0,03) \cdot 10^{-3}\text{ deg}$ in negative x- direction, $\theta_y^+ = (17,01 \pm 0,03) \cdot 10^{-3}\text{ deg}$ in positive y- direction and $\theta_y^- = (11,49 \pm 0,03) \cdot 10^{-3}\text{ deg}$ in negative y- direction. The light has subsequently been focussed down by an appropriately positioned lens ($f_i = 30\text{ mm}$) to a spot size of

¹The power- characteristic for this laser was measured and is presented in the appendix.

²For the nomenclature throughout the remainder of this report, the reader should notice the x- direction to be parallel to the optical table's surface and perpendicular to the optical axis, the y- direction to be perpendicular to both the optical table's surface as well as the optical axis of our imaging system and z to represent the optical axis. A right- handed coordinate system is used, whereas z always points into the propagation direction of the light.

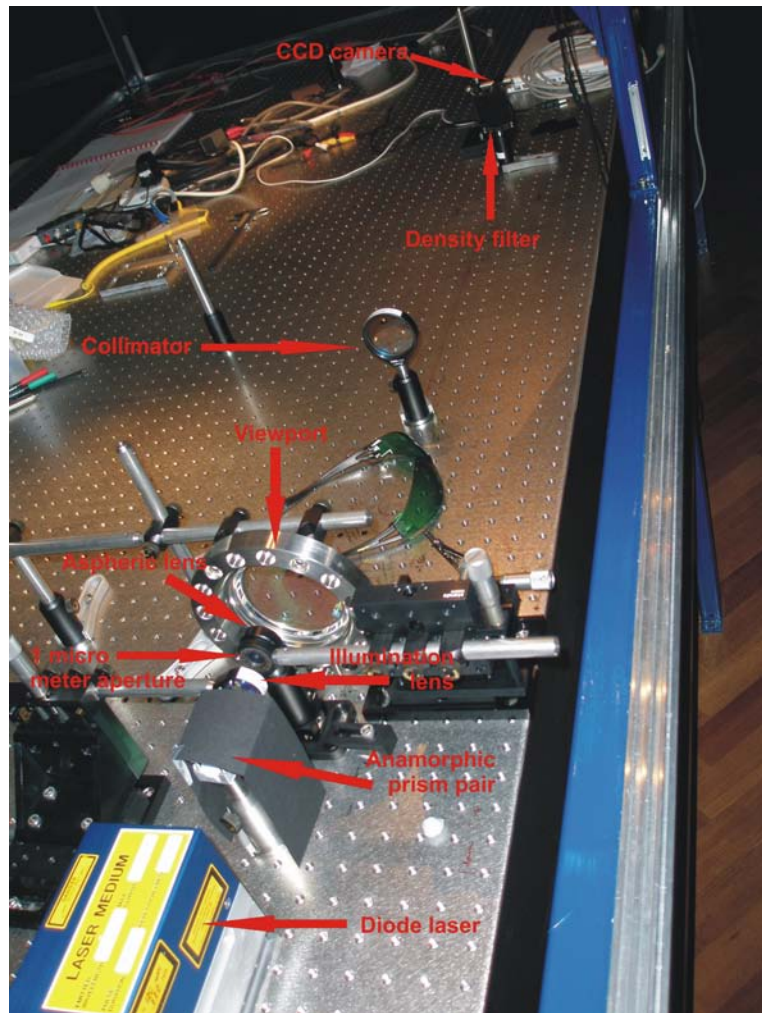


Figure 4.1: Picture of our setup showing all relevant components. The screening paper on top of the anamorphic prism pair acts to block stray- light.

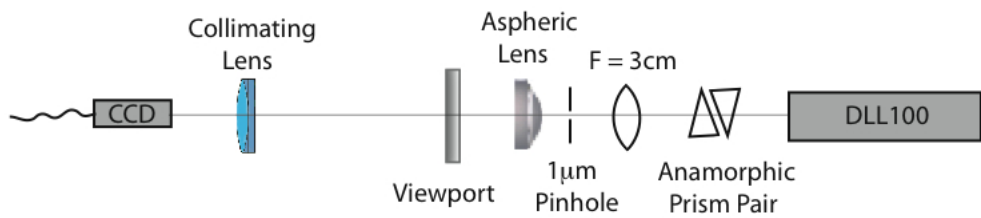


Figure 4.2: Schematic sketch of our first experimental setup, showing all relevant optical components.

$$w_i^j = \frac{\lambda f_i}{\pi w_3^j} \quad (4.1)$$

$$w_i^x = 19,65 \pm 1,04 \mu m \quad (4.2)$$

$$w_i^y = 18,76 \pm 0,95 \mu m \quad (4.3)$$

for illumination of the $1 \mu m$ aperture. There is a slight drawback here, since as soon as the aperture is going to be displaced in the transverse plane. Due to the tight focussing, a recognizable intensity loss will occur quite quickly, whence the illuminating lens is going to be moved as well, simultaneously to the aperture. This can result in slight displacements of the aperture with respect to the focus of the lens, due to the hysteresis of our translation stages. However we do not have to worry about changes in the illumination by this displacement, as we will not use the peak intensity values, obtained from our observed images, anyway. This is due to the kind of CCD camera we used, which has an automatical γ -curve adjustment. I.e. the camera will adjust its sensitivity in order to use its entire range of contrast for the particular image observed. That is particularly convenient for imaging spots of low intensity, as given in this experiment.

There is also neither a problem resulting from a tilt of the wavefront with respect to the aperture in the focus of the lens, nor do higher spatial frequencies on top of laser profile cause trouble, since the $1 \mu m$ aperture has a size approximately equal to the illuminating wavelength and is therefore acting as an ideal point source and spatial filter in transmission [6].

To align the aspheric lens, we used a $d_{10} = 10 \mu m$ aperture in the focal point of f_i and positioned the aspheric lens in order to have the aperture placed in its front focal point, providing collimation of the light beyond it. Using a $1 \mu m$ aperture in this step was not feasible, as the transmitted intensity was too small for proper adjustment. Since larger apertures are worse in providing point source behaviour, we pick up an uncertainty here, but the beam's divergence angles was only $\theta_{(x,y)} \approx 27,59 \cdot 10^{-3}$ deg, so the light originating from d_{10} can be assumed as collimated beyond the aspheric lens. Subsequently the viewport was added and the collimator was adjusted to a distance of $L_{2,3} = 35 cm$ from the aspheric lens.

One important point to mention here is Zeemax indicating $L_{2,3}$ to be uncritical, i.e. free to adjust in the experiment, which was taken for granted in all our experiments. So we set this distance to a convenient value for having a sufficient displacement range for the collimator, required in later measurements.

Finally the aperture was swapped to the $d_1 = 1 \mu m$ one, which was positioned at the combined focal points of f_i and f_a , therefore having a distance to aspheric lens of $L_{1,2} \approx 8,1 \pm 0,2 mm$, corresponding to its $BFL^3 = 8 mm$ (fig. 4.2).

Unfortunately our apertures also had little holes besides the desired aperture, which resulted in serious stray-light.

At last the CCD camera was positioned with a distance to the collimator of $L_{3,4} \approx 75 cm$, by

³BFL= back focal length

observing the recorded images while displacing it along z and looking for an image with the smallest magnification. It is important to note, that the purpose of the system is not to provide a perfect imaging system giving a certain spot size. In general, we want to focus the light down as tightly as possible, in order to create narrow, but deep potential wells. Hence having an exact magnification of $M = 62,5$ is not important; the spot has to be as small as possible.

4.1.2 Advantages and aims

The obvious reasons for building this system are easy to grasp:

- The curvature and spatial frequency content of the illuminating beam is not critical.
- The magnification is a directly accessible parameter here.
- It guarantees a $1 \mu m$ spot to start with, i.e. operating the system at its diffraction limit, which can only be concluded in the other setups.
- It provides an indication of the system's behaviour in terms of geometrical aberrations. As our translation stages were only precise to $\Delta(x, y) = 10 \mu m$, displacement step sizes of this value have been used. Due to the transverse magnification ($M = 62,5$) of the system, each step would correspond to a dislocation of a spot on the DMD of $(\Delta(x, y) = (625 \mu m, 625 \mu m))$. Therefore we can utilize the range of our stages to map farer off axis as obtainable in the two following experiments.

These far off-axis displacements guaranteed appearance of geometrical aberrations and allowed an approximation of an aberration free range.

The measured parameters in this system were:

- Changes of the maximum and minimum beam waist for the imaged spot, as the $1 \mu m$ aperture is displaced in its transverse plane.
- Ability to restore the focus ⁴ by movement of the collimator, as the aspheric lens is displaced along z.

4.1.3 Measurements

Image shape: Imaging the $1 \mu m$ aperture with this setup resulted in a circular spot, which was surprisingly surrounded by a ring pattern, see fig: 4.3, .

This ring pattern can obviously not be generated by Fraunhofer diffraction from the aperture, as this would result in an diffraction angle of [6]:

$$\Delta\theta = 1,22 \frac{\lambda}{d_{1\mu m}} = 0,9516 \text{ deg} \quad (4.4)$$

⁴i.e. can a position be found, for which the imaging condition is fulfilled again

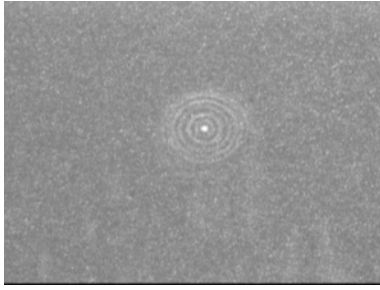


Figure 4.3: Image of a $1 \mu m$ aperture, comprising a ring pattern surrounding the central spot.



Figure 4.4: Image of a $1 \mu m$ aperture, with ring pattern attenuated by density filters.

which corresponds to a radius between the central maximum and the first minimum of the Airy disk, at the entrance pupil of the aspheric lens, of [6]:

$$r_{diff} = 1,22 \frac{f\lambda}{d_{1\mu m}} = 7,6 \text{ mm} \quad (4.5)$$

thus the diameter of the central spot $d_{Airydisk} = 15,22 \text{ mm}$ is larger than the lens itself. So we examined our imaging situation using the *Fresnel explorer*[©] simulation software. This provided the Fresnel diffraction pattern in the proximity of the aperture along the optical axis. The interesting part is here, that even with an aperture displacement of less than $10 \mu m$ along z, one had already proceeded through dark and bright spots on axis.

As the aperture translation stage had a scale- size of $10 \mu m$, a similar uncertainty of the aspheric lens' focal point position was thus unavoidable.

Therefore we treated this ring pattern as a systematical alignment error, generated by not having the $1 \mu m$ aperture in the exact focal point of the aspheric lens, hence imaging the Fresnel diffraction pattern in the proximity of the aperture instead of the aperture circle itself, resulting in imaging of the associated ring pattern as well. In the second experiment, as alignment of the object aperture was not critical, we however observed a similar ring pattern, whose origin was figured out to result from the aspheric lens. Nevertheless this experiment, both effects might have been superimposed on each other.

Movement of the aperture in its transverse plane We first displaced the $1 \mu m$ aperture in the focal plane of the aspheric lens, using a step size of $\Delta(x,y) = 10 \mu m$. This would correspond to an displacement on the DMD of $0,625 \text{ mm}$ ⁵ for generating this. We used these to have the opportunity to operate the system at its extremities in order to see, whether aberration effects are visible in the way we anticipated.

This clearly turns out, if one takes a look at an image on axis (fig: 4.3, fig: 4.4), and compares these images with the ones recorded at a distance of $\Delta x = 140 \mu m$ off axis (fig: 4.5, 4.6): The central images have a circular focus and a high intensity at their centres with very little

⁵anticipating an ideal system with a magnification of 62,5

intensity in its surrounding ring pattern; whereas the off axis images, peu a peu comprise a more elliptical shape, ending up in a pattern expected for comatic abberation. Intensity gets redistributed from the centre into the ring pattern, so a trap displaced this far from the optical axis would be very shallow and broad, thus not able to confine atoms for a longer time.

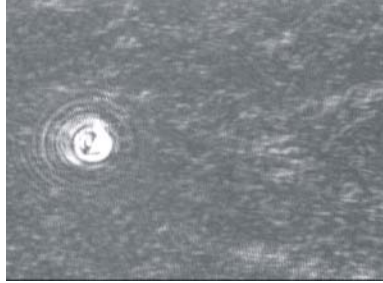


Figure 4.5: Off axis spot recorded with CCD camera operated in saturation, clearly showing the coma- like aberrations of the spot.



Figure 4.6: Off axis spot recorded with CCD camera, showing the redistribution of intensity away from the central spot. Density filters have been applied to avoid saturation.

In order to get more quantitative estimations, we processed all our files using *MatLab*[©]. Here a Gaußian fit of the central spot was made ⁶ (fig: 4.7), the underground noise was modeled as a Fourier- series (fig: 4.8) and subsequently got subtracted from the data (fig: 4.9), so a noise free fit could be obtained. The sizes of the spots were determined by the maximum and minimum Gaußian beam waists (fig: 4.10). For achieving the latter, a coordinate transformation was required, as both extremities in the beam size generally did not correspond to our CCD's screen orientation.

For off- axis values, showing recognisable abberations, the fit turned out to be challenging, as the central peaks became quite small and often showed ambiguous summits (fig: 4.11, 4.12). Nevertheless, they were approximated the same way (fig: 4.13) and side-lopes, originating from abberations have been neglected (fig: 4.14).

The results from transverse displacement measurements in the focal plane of the aspheric lens are shown in the figures 4.15 (providing the behaviour of the fitted intensity), 4.16 (providing the fitted maximum waist) and 4.17 (providing the behaviour of the fitted minimum waist).

Looking at fig. 4.15, one sees the trend of the intensity to drop of, as the aperture is displaced from an on axis position. This is clearly the expected behaviour if geometrical abberations appear: Since these comprise different magnification effects for the different planes (sagittal and meridional) of the lens (see chapters on coma and astigmatism in [6]) as the object wanders off axis, the image spot is not focussed as tightly to a circle anymore. Caused by coma, intensity is removed from the centre of the spot, resulting in a decrease of the Gaußian peak value, as obtained in 4.15. With the automatic γ - adjustment of the camera, the intensity plots

⁶As indicated in the theory section, we approximate the central lobe of the Airy disk as a Gaußian function.

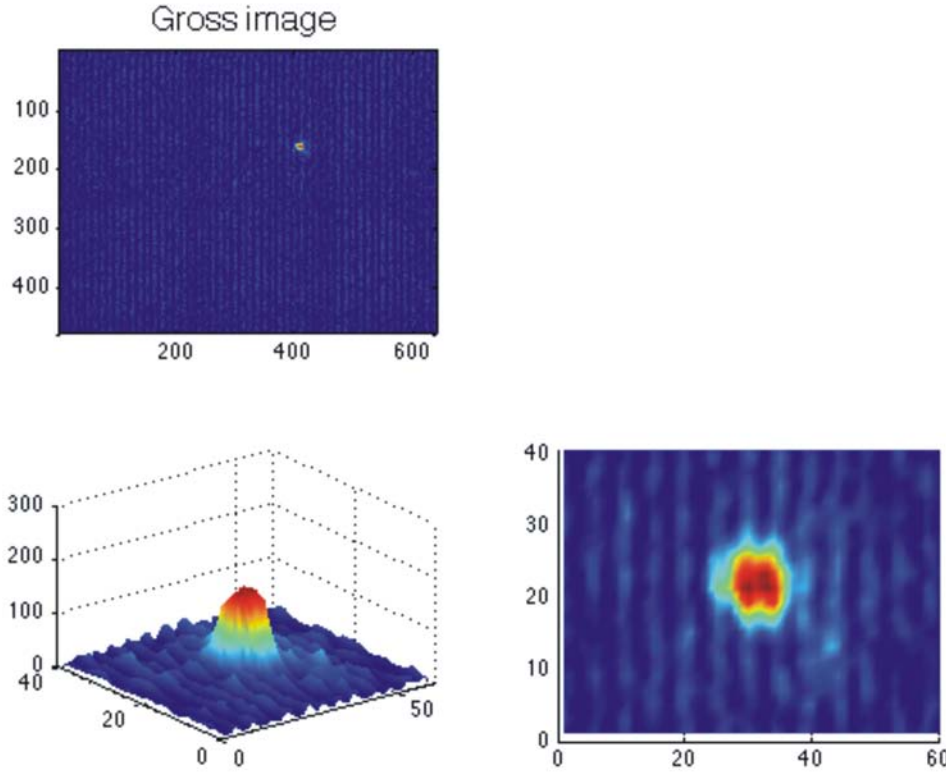


Figure 4.7: Plain on axis CCD camera image, read into *MatLab*[©].

do not inevitably show the correct behaviour, as for decreasing intensity, the camera might have switched to another sensitivity range. Therefore we will ignore the behaviour of the intensity for the remainder of this report, as it does not provide a reliable basis for obtaining conclusions about the system.

Besides changes in peak intensities, one also expects the beam waist to increase for larger displacements, which is very nicely obtained in fig: 4.16 for the maximum waist. Since aberrations are caused by different magnification factors in the meridional and saggital plane, we know, that for geometrical aberrations the maximum beam waist should increase. The minimum waist however provides much less relative increase than the maximum (fig: 4.17), which again ties in with our expectations: Since e.g. coma does provide a comet- tail like image shape, one would expect an elliptical image profile, thus the maximum beam waist has to increase further than the minimum waist; otherwise no elliptical image can be obtained. Nevertheless both waist values should increase, as geometrical aberrations cause the imaging quality to deteriorate, hence leading to inability to focus as tightly as with the object on axis. So an aberration like coma or astigmatism should always affect the maximum beam waist to greater extend, as obtained for the apparent situation. As far as the overall magnification is concerned, we expected a waist value of $w = 62,5 \mu\text{m}$, if the system is perfectly adjusted to the 2f- situation. Referring to the maximum beam waist, this is obtained for the on axis position (fig: 4.16). However the

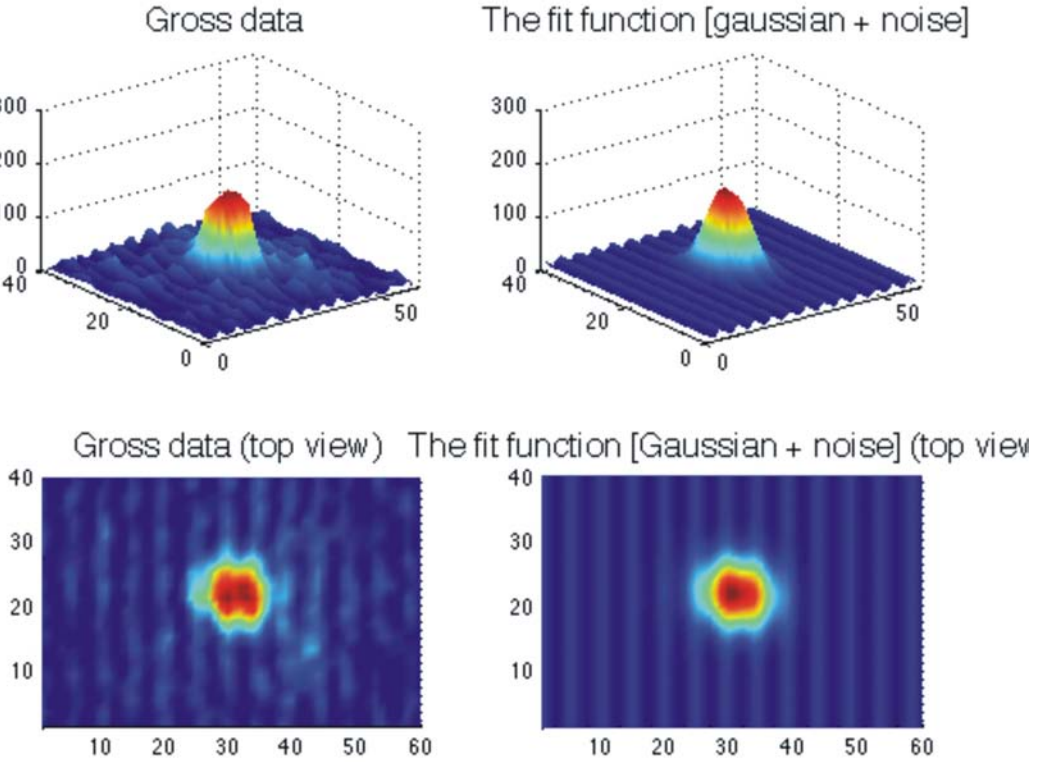


Figure 4.8: Noise and Gaußian profile of central image fitted by *MatLab*[©].

minimum beam waist does have an on axis value in the $w_{min} \approx 50 - 55 \mu m$ regime and is thus smaller in diameter. The origin of this feature and even the fact of having an elliptical beam with two different waist values on axis, does neither depend on the aperture, the illumination or the object and image distances nor on the lenses being hit slightly off axis. If one of these points was the source of this effect, it would vanish if we either spatially filter the illuminating beam, use a different aperture or change the relevant distances, which is done later on ⁷. However during the second experiment, we discovered effects like these being due to tilts of the aspheric lens (see next section), so we anticipate to have the aspheric lens slightly tilted here, especially as we did not know about the sensitivity of the system on such misalignments while performing this measurement ⁸. Looking at the magnifications once more, we can directly compute those from the beam waists, as the object is a $1 \mu m$ aperture. Obtaining a result around the expected values of 62,5 proves, that we are able to operate our system in the diffraction limited regime and in turn we will be able to focus down to an image size $\leq 1 \mu m$ by using the real beam path

⁷We changed the pinhole size and the quality of the illuminating beam in the second experiment, and varied the object and image distances by displacing the aspheric lens, nevertheless the same elliptical shape was observed.

⁸The two spikes in fig. 4.17 are due to an assignment error in the *MatLab*[©] code, as these two values should normally be among the w_{max} data, since they are larger than the appropriate ones in the w_{max} plot. This happens sometimes, as especially at the extremities of the displacement ranges, the spot is far from being Gaußian. Therefore our fit is not a really good approximation anymore, causing errors like these to occur.

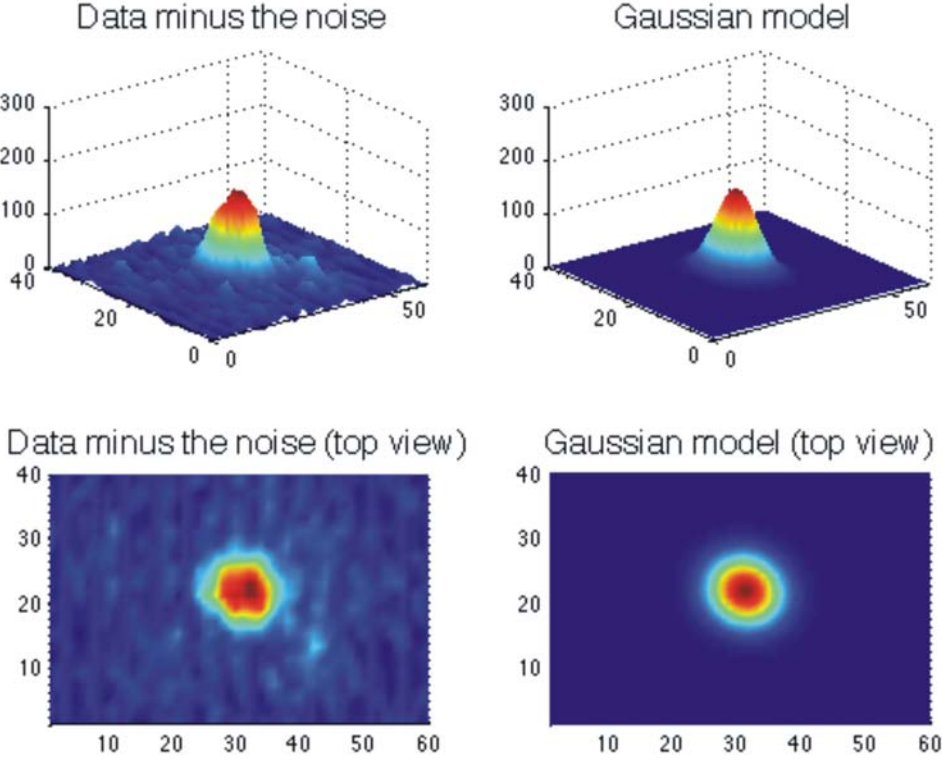


Figure 4.9: Noise subtracted from on axis image.

and a $50 \mu m$ object.

We furthermore see, that the aberration effects start to become serious for a displacement of approximately $\Delta(x, y) \approx 40-50 \mu m$ away from the optical axis. This looks particular promising, as it is quite a large distance over which we can move our dipole trap without running into strong distortion effects.

One drawback in this measurement, as far as geometrical aberrations are concerned, is our inability to measure field curvature effects precisely and distinguish them from coma/ astigmatic effects, since we only have a small circular spot available.

Displacement of aspheric lens and restoring focus by movement of collimator In order to check our ability to move the focus along the optical axis, we now changed the position of the aspheric lens along the optical axis and observed the quality of the system again by moving the aperture along x and y subsequently (step size $\Delta(x, y) = 20 \mu m$). Positive z -displacements correspond to an increase of the aperture- aspheric lens distance $L_{1,2}$, hence an effective positioning of the former in front of f_a , whereas negative z - values correspond to a decrease in $L_{1,2}$ leading to an aperture position beyond f_a .

Pictures of the resulting unfocussed image and the restored focus after moving the collimator along z can be obtained from fig. 4.18, 4.31.

The results of our measurements with an aspheric lens displacement of $\Delta z = \pm 20 \mu m$ can be

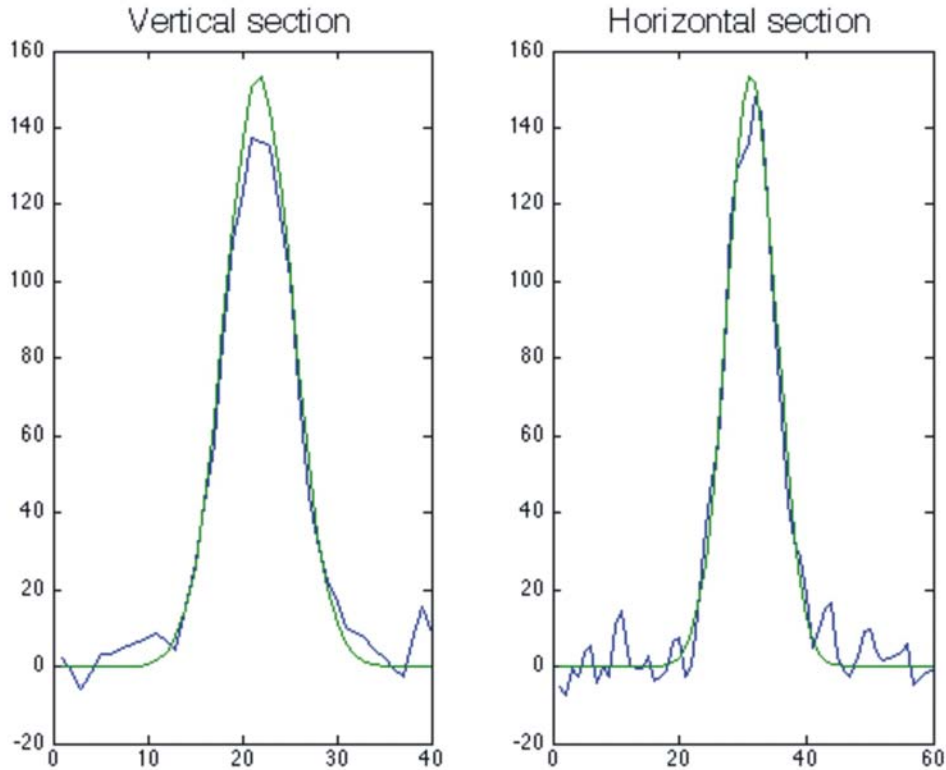


Figure 4.10: Gaußian fit in directions of minimum and maximum beam waist for on axis image.

obtained in the fig: 4.22, 4.23 (showing the minimum waist behaviour), 4.20 and 4.21 (showing the maximum waist behaviour).

In the minimum waist data (fig: 4.22, 4.23) we again see approximately constant behaviour as expected from our way of data processing. The maximum beam waist values (fig: 4.20, 4.21) comprise the anticipated development for the $z = -20 \mu m$ data, especially in the y direction. The deviation of the minimum waist from $x = 0$ in fig: 4.21 as well as the lack of trend in 4.20 might be correlated with our aspheric lens and subsequent collimator movement: If the translation stage, holding the aspheric lens, is not perfectly parallel to the optical axis, the beam will start to hit the lens off axis. The collimator was furthermore moved by hand, without being able to see the incident light ⁹; so a misalignment effects occur here quite rapidly. As the system does have an abberation free range in the micro metre regime, it is clear, that dislocations of optical components during the measurement cause the alignment to deteriorate and this regime to wander off axis, since the optical axis is displaced. This is also indicated by the sequence of taking the measurements: starting with y at $z = -20 \mu m$ and ending with x at $z = +20 \mu m$ results the latter to have a high probability for alignment errors.

The distances the collimator had to be moved along the optical axis in order to restore the foci (see table 4.1) were within the cm regime, which is expected from geometrical optics, providing

⁹As the transmitted intensity from a $1 \mu m$ aperture is simply too small

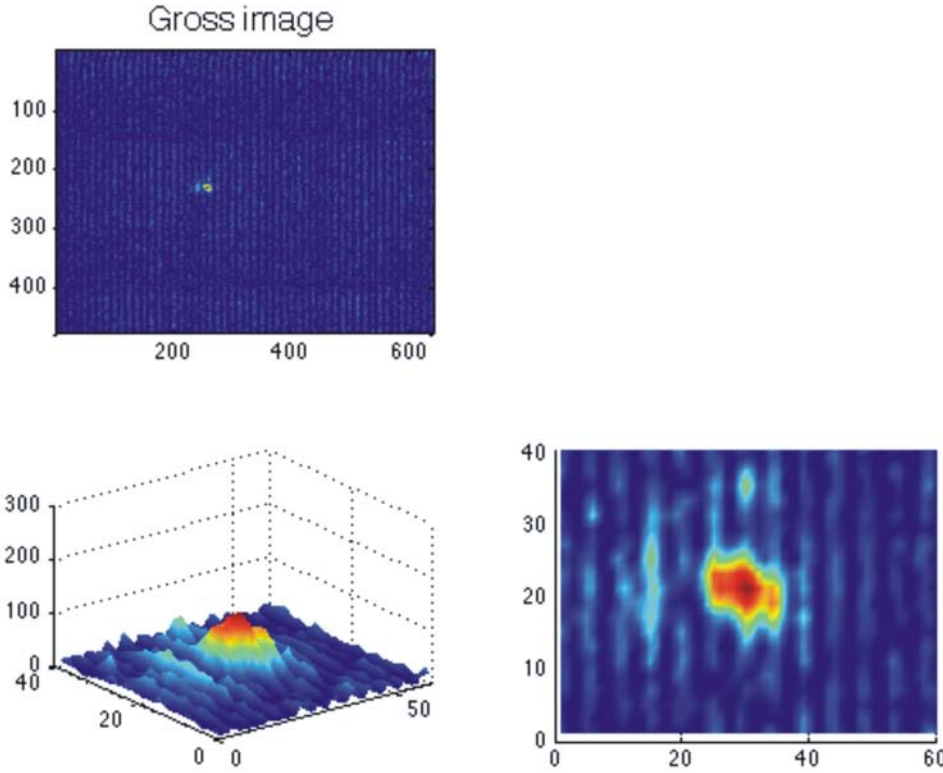


Figure 4.11: Plain off axis CCD camera image, read into *MatLab*[©], showing much smaller and broader peak with unclear summit.

aspheric lens displacement [μm]	collimator displacement [cm]
20	$-10, 35 \pm 0, 1$
-20	$+6, 5 \pm 0, 1$

Table 4.1: Collimator displacements needed for restoring focus.

a longitudinal magnification of [6]:

$$M_{long} = M_{trans}^2 = 62,5^2 = 3906,25 \quad (4.6)$$

So one would expect a required change of the collimator's position in the region of $d_c \approx 7,8 \text{ cm}$ for $\Delta z_{asph.lens} = 20 \mu\text{m}$. Deviations can be understood by crudely thinking of the system as one thin lens: Object movements in front and beyond the focal point of a lens do not provide linear image displacements. Because the lens equation [6] $\frac{1}{f} = \frac{1}{|s_{obj}|} + \frac{1}{|s_i|}$ contains these distances reciprocally, the above stated values (table 4.1) are not expected to be equal. However these values provide us with an estimation of the required size for the collimator delay-line to change the atom's altitude in the final trapping setup.

Summary The results from this experiment look quite promising. They indicate a broad range of aberration free imaging (of about $\Delta(x, y) \approx 45 \mu\text{m}$ to either side of the optical axis)

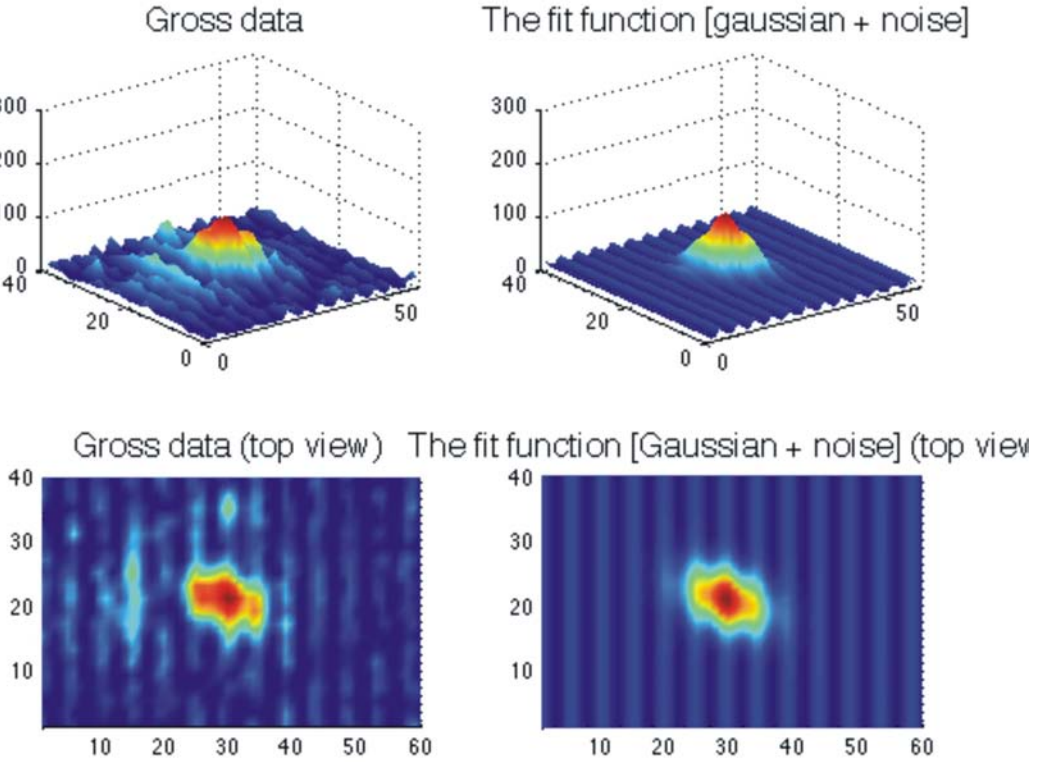


Figure 4.12: Noise and Gaußian profile on off axis image fitted by *MatLab*[©].

and show our ability to align the reversed beam path, achieving an image spot size in the region of the diffraction limit. They also indicate an insensitivity of the setup to slight deviations from the 2f- condition¹⁰ and provide an idea of the required longitudinal displacement of the collimator to move atoms along the optical axis.

Furhter investigations now aim for a more precise testing of the system around its abberation free region and a way for alignment, which is also applicable to the final trap.

4.2 Experiment 2

4.2.1 Setup and alignment description

Setup Our second experiment illuminates the system in its correct operating direction, i.e. light is impinging on the collimator first and afterwards focussed down by the aspheric lens. For testing purposes, we image a $50 \mu m$ aperture, positioned in the focus of the collimator this time, hence we mimic the effect of the DMD by using the aperture. The light transmitted by the aperture is therefore focussed down to an approximate spot size of $d_i \approx 0,8 \mu m$, which is not observable directly on our CCD camera with a pixel size of $7,8 \times 7,8 \mu m$. Therefore we reflect the light back through the system by using a mirror, positioned in the focal point of

¹⁰i.e. object and image distances differing from the focal lengths of the lenses

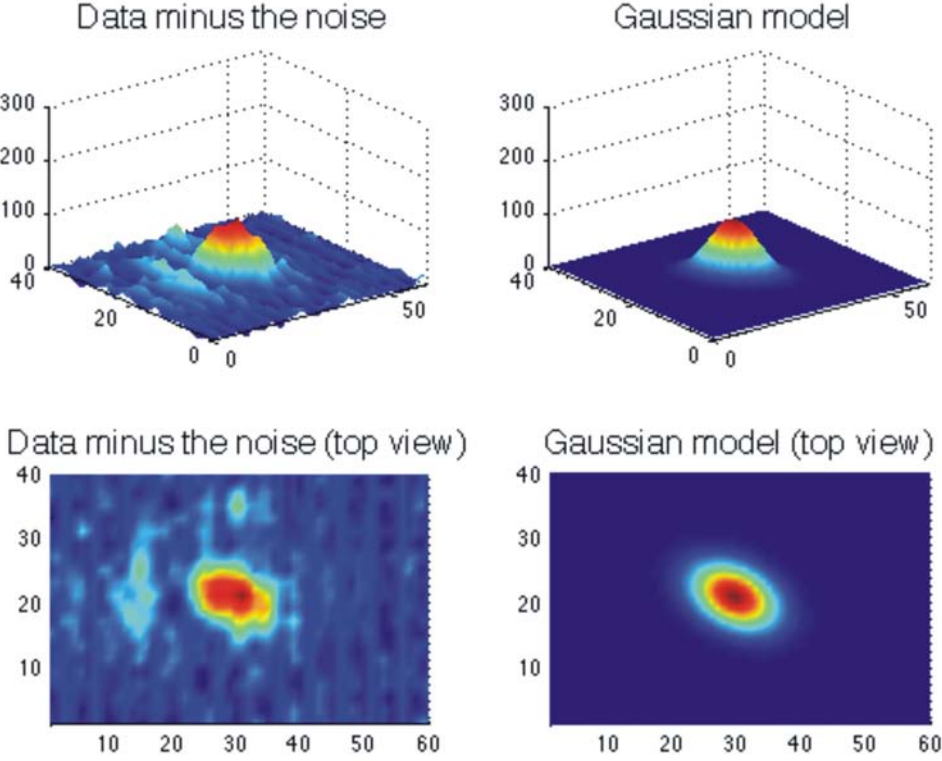


Figure 4.13: Noise subtracted from off axis image.

the aspheric lens. The back- reflection is afterwards read out by a polarising beam splitter, requiring the usage of polarisation optics within the setup. In order to receive a 2f- system in back- reflection as well, the collimator- CCD distance $L_{C,CCD}$ is equal to the collimator-aperture distance $L_{C,50} = 750\text{ mm}$. The final setup can be seen in fig: 4.24.

In this system, we will displace the $50\text{ }\mu\text{m}$ aperture in its transverse plane to simulate the effects of the DMD, therefore we require an available macroscopic range (about 6 mm in the end) and a large illuminating beam with nearly constant intensity throughout it. Furthermore the aperture is now not small enough anymore to be approximated as a diffracting point source [6] ($d_{aperture} > \lambda_l$), so we require an illuminating beam of high quality to exclude higher spatial frequencies, messing up our images otherwise (by appearing like additional distortion effects). So the initial laser beam from the anamorphic prism pair must be spatially filtered, which is achieved by a 300 mm lens $f_{1,sp}$ [21], focussing down on a $50\text{ }\mu\text{m}$ aperture ¹¹, providing a focussed beam waist (according to eq: 4.1, with the waist values after transmission through the prism pair at the position of $f_{1,sp}$: $w_x = 0,379\text{ mm}$, $w_y = 0,397$) of $w_x = 196,5\text{ }\mu\text{m}$ and $w_y = 187,6\text{ }\mu\text{m}$, thus the $50\text{ }\mu\text{m}$ aperture only transmits the 0^{th} order mode of the laser beam. The profile of the transmitted beam beyond the aperture was determined to pure Gaussian, with divergence angles of $\Theta_x \approx 0,716\text{ deg}$ and $\Theta_y \approx 0,764\text{ deg}$.

¹¹The focussing lens was placed at the position of the former illuminating lens, the aperture was obviously placed in the lens's focus.

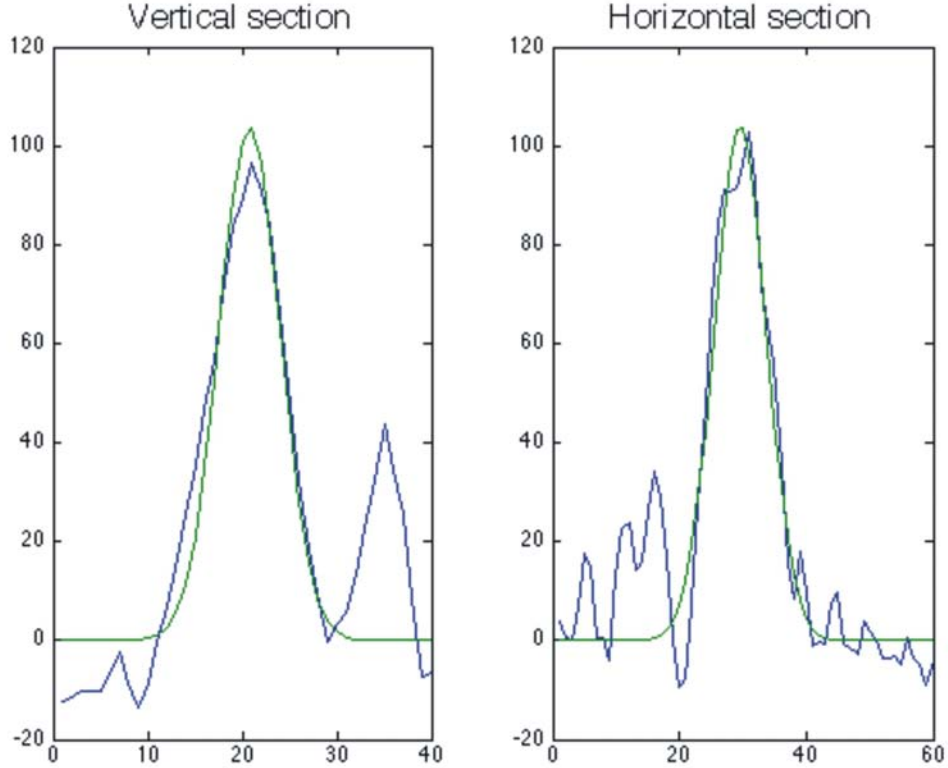


Figure 4.14: Gaußian fit in directions of minimum and maximum beam waist for off axis image; sidelops due to coma have been disregarded.

The beam is subsequently collimated by another $f_{2,sp} = 300\text{ mm}$ [21] lens, providing a collimated beam waist of $w_x \approx 7.5\text{ mm}$ and $w_y \approx 8\text{ mm}$ and a divergence angle of $\vartheta \leq 2 \cdot 10^{-4}\text{ deg}$, which is convenient for illuminating the $50\text{ }\mu\text{m}$ test-aperture. The focal length of this last lens has been chosen, in order to achieve a suitable beam diameter and also an appreciable peak intensity.

The incident light on the $50\text{ }\mu\text{m}$ testing aperture was linearly polarised by a $\lambda/2$ plate. In order to couple out the back-reflected beam, a polarising beam splitter (PBS1) has been placed beyond the aperture, followed by a $\lambda/4$ -plate, generating circular polarised light. By reflecting from the mirror, the polarisation is shifted by 180 deg , resulting in circular polarisation of opposite handedness in back-reflection and after propagation through the PBS1 in linear polarisation \perp to the incident one. This "reads out" all light back-reflected and therefore enables sufficient intensity for observation, see 4.24. For alignment purposes a second PBS (PBS2), followed by a $\lambda/4$ -plate has been placed in front of the $50\text{ }\mu\text{m}$ aperture position for observing the light reflected through the aperture.

Alignment In order to align the system, a sophisticated scheme, guaranteeing both paths to be on axis and as coincident as possible, had to be developed.

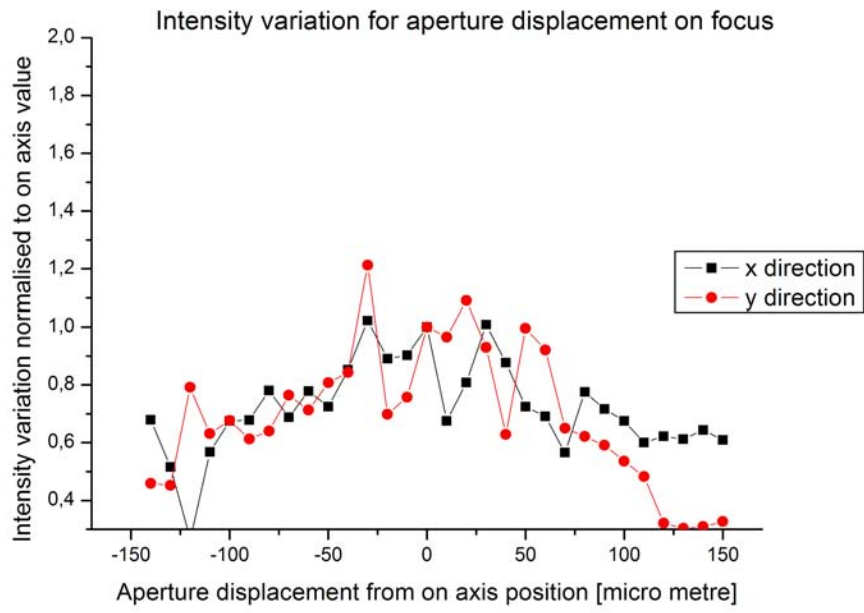


Figure 4.15: Intensity measurement due to aperture displacement in transverse plain, showing larger intensities in on axis position.

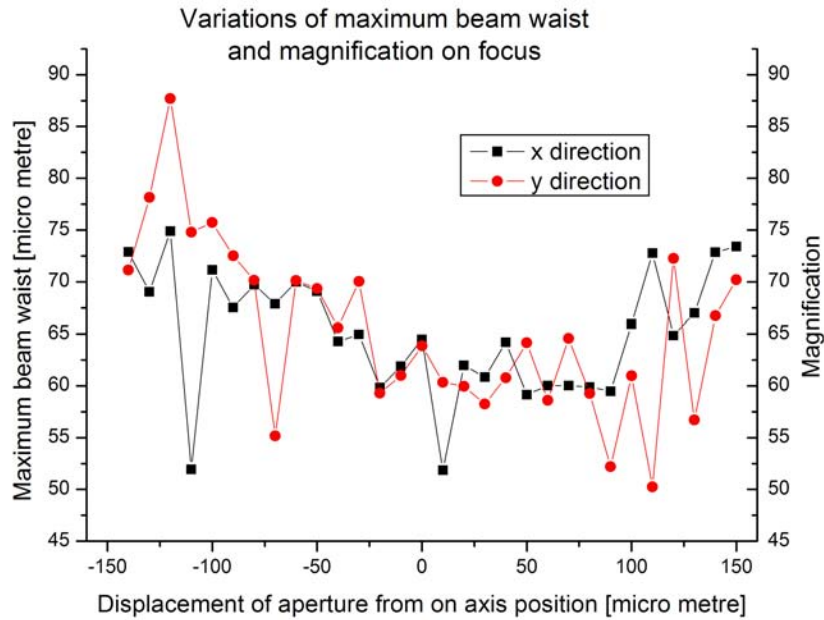


Figure 4.16: Maximum beam waist measurements for aperture displacement in transverse plain, showing increasing values for going off axis.

1. The collimator was adjusted to be hit by the unperturbed laser light first, i.e. no aperture or lens was included after collimation of the beam in the spatial filter. Furthermore its position has been adjusted to best alignment over the entire delay-line, needed for the

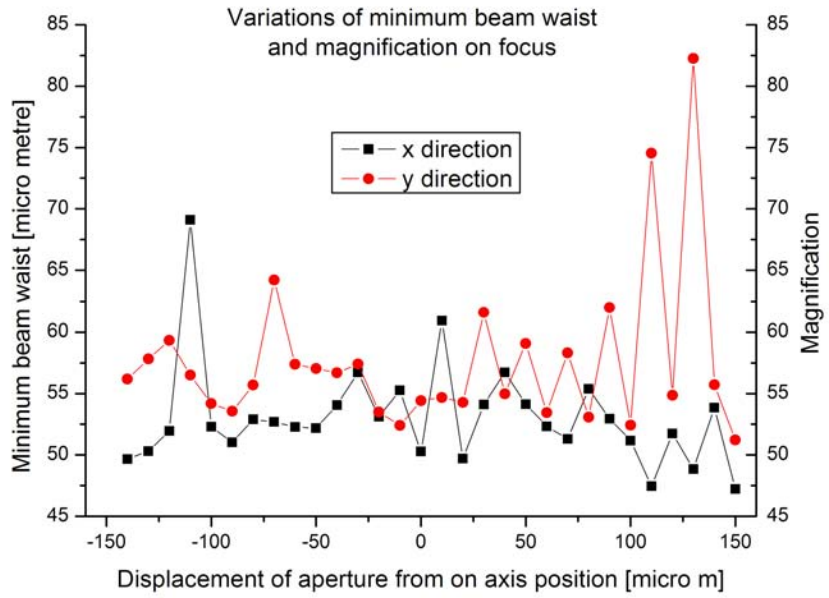


Figure 4.17: Minimum beam waist measurements for aperture displacement in transverse plain, showing nearly constant behaviour, slightly increasing towards off- axis.

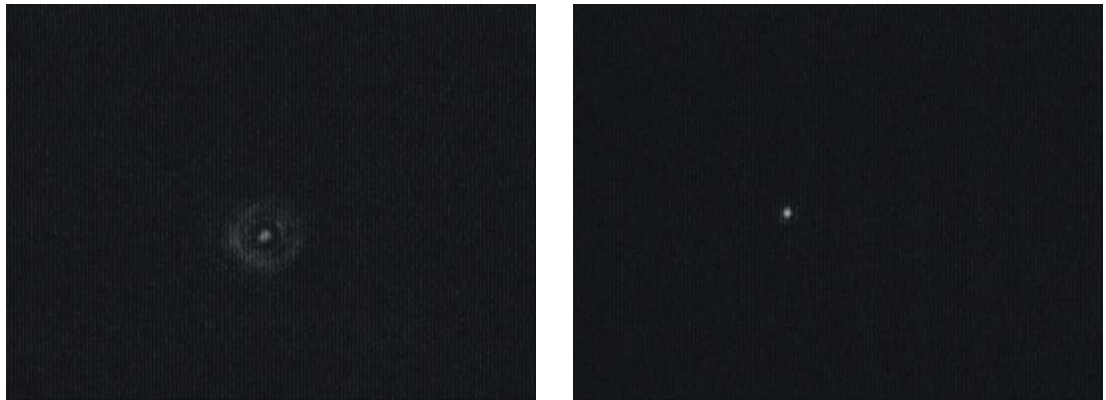


Figure 4.18: Defocussed image after moving aspheric lens by $\Delta z = 20 \mu\text{m}$.

Figure 4.19: Focus restored by appropriate collimator movement along z.

later displacement measurements of the aspheric lens ¹².

2. After aligning the collimator, a mirror was introduced in order to reflect the beam back. Its tilting angle was fine- adjusted by first observing the unperturbed laser beam and then adding an adjustable diaphragm in the focal point of the collimator; this was done by simply measuring the distance, as the system is very insensitive to slight deviations from the ideal distance of $d_{C,50} = 750 \text{ mm}$ on the object site ¹³, due to the large longitudinal magnification. In the last case, light diverging from the diaphragm gets collimated by the

¹²Equal to the ones done in the first setup with displacing the aspheric lens and restoring the focus by collimator movement

¹³see displacement results for collimator obtained in the last experiment

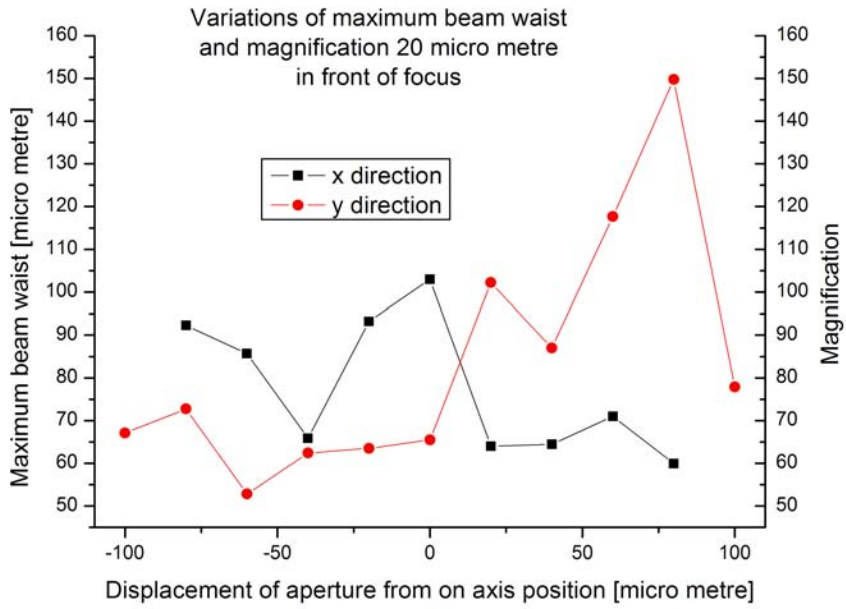


Figure 4.20: Maximum beam waist for $z = +20 \mu\text{m}$ aspheric lens displacement; showing increasing waists to either side from on axis position.

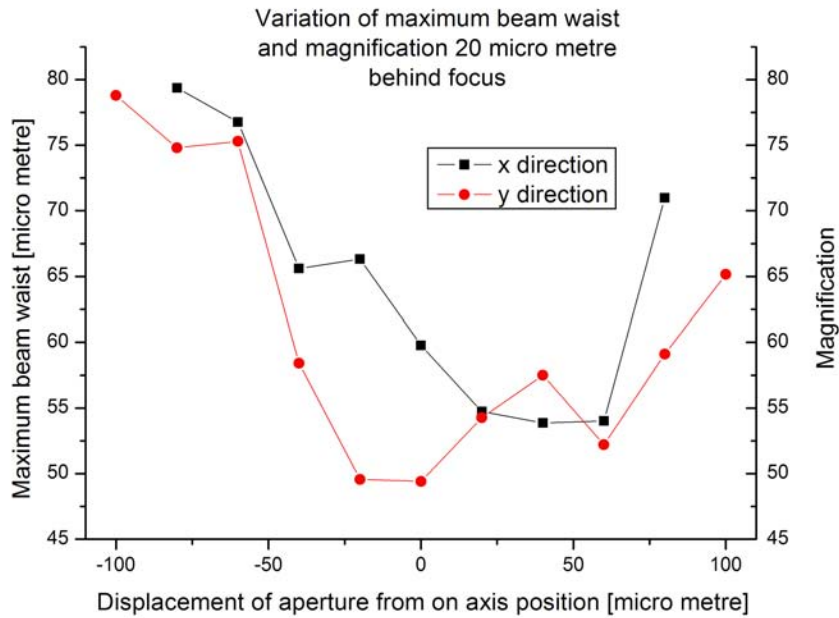


Figure 4.21: Maximum beam waist for $z = -20 \mu\text{m}$ aspheric lens displacement; showing no clear trend in either direction of aperture displacement.

lens (f_C). If the mirror is aligned perpendicular to the collimated beam, the light gets reflected and focussed down by the collimator exactly to the same position it originated

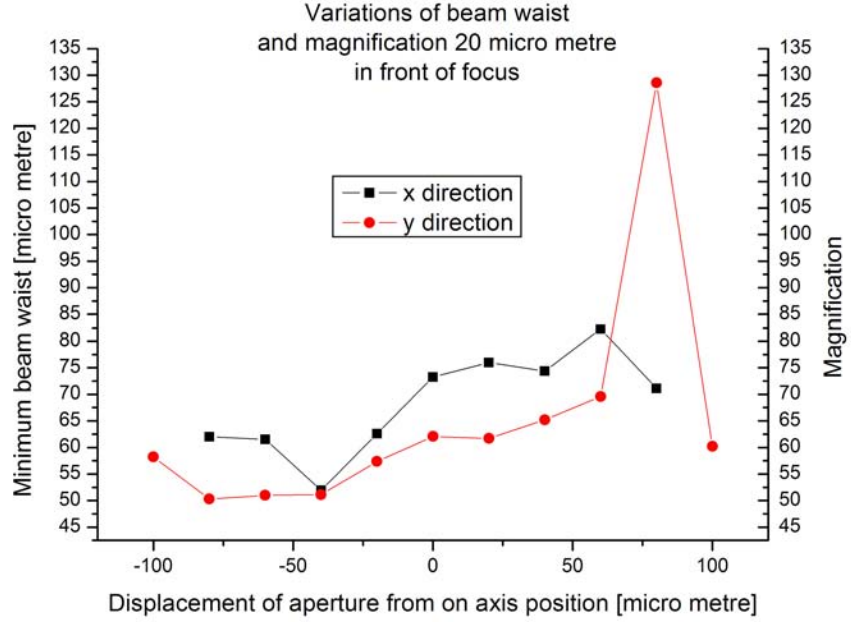


Figure 4.22: Minimum beam waist for $z = +20 \mu\text{m}$ aspheric lens displacement; showing approximately constant waist size over displacement range. Spike at $z = 0,8 \mu\text{m}$ results from a the failure of the fitting routine.

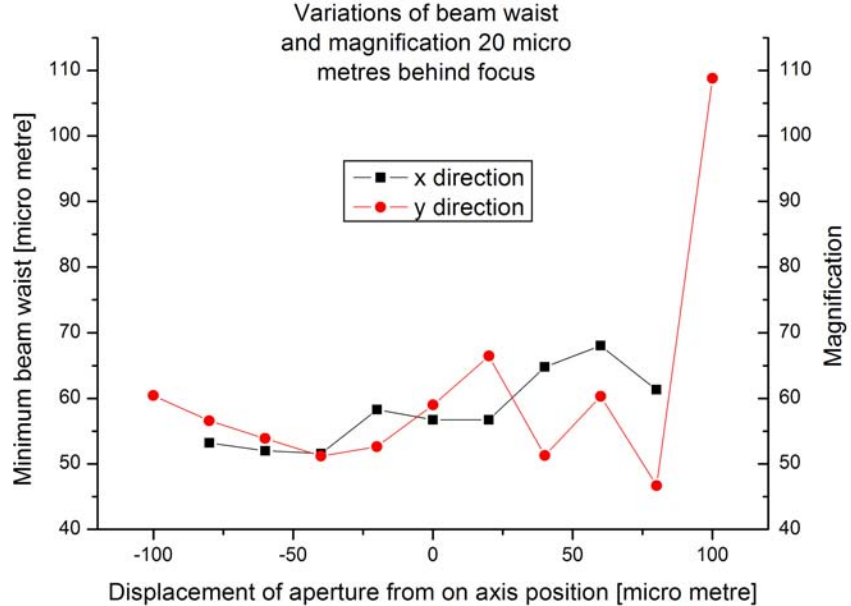


Figure 4.23: Minimum beam waist for $z = -20 \mu\text{m}$ aspheric lens displacement; showing constant behaviour. The spike at $z = 1 \mu\text{m}$ results from a the failure of the fitting routine.

from ¹⁴. This was observed by reflecting the transmitted light with the PBS2 through an

¹⁴We also tried to use the $50 \mu\text{m}$ aperture itself for alignment, which required an additional focussing lens to see

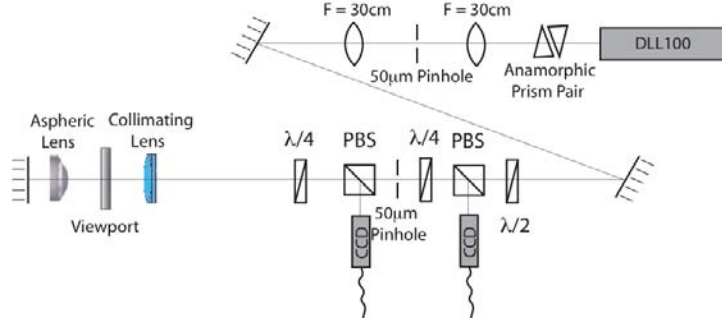


Figure 4.24: Final setup for the second experiment, showing all relevant components for aligning and measuring the system.

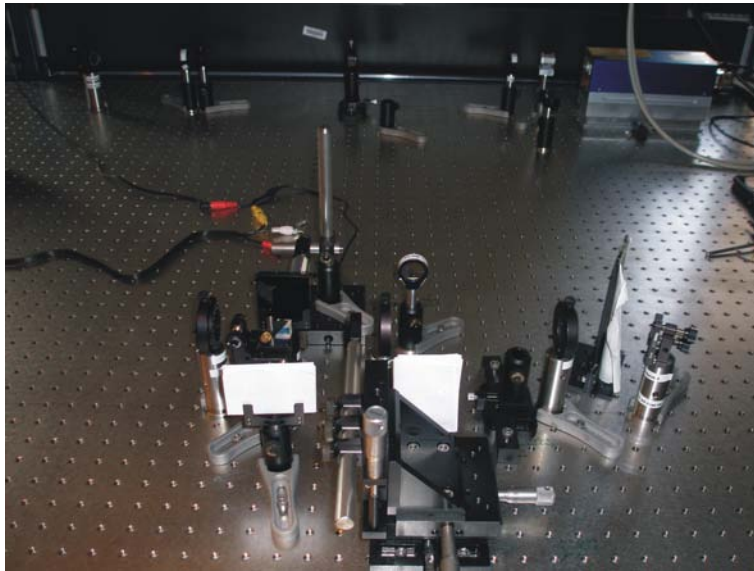


Figure 4.25: Picture of spatial filter and components, needed for alignment.

imaging lens ($f_i = 100\text{mm}$ [23]) onto the CCD camera (see fig. 4.25).

3. Subsequently the aspheric lens was included and adjusted to be hit on axis. Also tilts were erased as good as possible in later setups ¹⁵, after we discovered their influence. This alignment was done by observing the back- reflected light through the PBS1 with the CCD camera and adjusting for least distortion of the image.
4. The next step was to set the aspheric- lens mirror distance to have the focus of the lens on the mirror surface ¹⁶. This was accomplished by observing the back- reflected light, transmitted through the diaphragm with a power- meter and setting the distance to the

the transmitted back- reflection. However this lens changed the optical axis due to even slightest misalignment, resulting in a wrong positioning of the mirror.

¹⁵i.e. as soon as we endeavoured their effects

¹⁶As described in the theory chapter, the trap will later have its focal point slightly above the mirror. Despite this fact, we wanted to observe the systems imaging qualities and therefore we require to image the focus in back- reflection through the system with the same magnification as on the incident path, which constrains it to be placed on the mirror.

position of maximum power. Since the image will then be generated in the focus of the collimator, we can conclude the light between the latter and the aspheric lens to be collimated and hence the mirror to be positioned in the focal point of the aspheric lens, generating the 2f- configuration.

5. In the last step, the variable diaphragm was simply swapped to the $50\mu m$ aperture, which was positioned transversely in the collimator's focal plane by adjusting for maximum power transmittance. Furthermore the CCD camera was positioned to a distance $L_{C,CCD} = 750\text{ mm}$, while observing the light reflected by PBS1.

The main advantage of this procedure is its applicability to the actual trap alignment. One can also start off with aligning the collimator on the optical axis and then subsequently guiding the beam into the MOT via a periscope. As the bottom- mirror in the MOT is fixed in position, the alignment, which was done here by tilting the mirror itself, can be accomplished by adjustment of the periscope mirrors. Once this system is set, one can include the aspheric lens into the MOT, and then centre the beam path by appropriate adjustment of the periscope mirrors. The only problem in this scheme are tilts of the aspheric lens. In the testing setup, we had this lens sitting on a tilting stage (as used for mirrors), in the real setup, tilts can be erased by changing the angle of the incident beam by the periscope mirrors. Unfortunately an angle- change will result in the mirror not to be perpendicular the optical axis anymore, thus the back- reflected beam has a smaller overlap with the incident one, resulting in a smaller contribution of the partial standing wave to the trapping potential ¹⁷. Hence if the aspheric lens cannot be positioned precisely with respect to the mirror surface, we either lose potential depth by curing this tilt with the periscope mirrors, or we are required to use a piezo- stage for the lens to tilt it automatically ¹⁸.

One should also note here our mirror in this setup to be a metallic one, which was chosen on the initial estimation, that a dielectric mirror could provide ambiguity in finding the focal point and cause interference between the partially reflected beams with the incident one (see fig: 3.10), due to its multiple layer structure. We also checked this by setting up the system with the dielectric mirror at the end of this experiment and did not find any of the anticipated diffraction grating- like effects or difficulties in finding the appropriate focus. So we do not expect this difference to cause severe problems in the real setup.

Advantages and aims After finding an appropriate alignment procedure for the imaging system, we desired to test the following properties:

- Effects of displacing the $50\mu m$ aperture in its transverse plane. Using a range of $\Delta(x,y) \approx 6\text{ mm}$ in total, we will have a image displacement range on the mirror of ¹⁹ $\Delta(x',y') =$

¹⁷see theory section

¹⁸As the time of the project was unfortunately too short to try the real setup, this question still has to be examined experimentally

¹⁹Anticipating an ideally aligned system, comprising a magnification of $M_{transverse} \approx 62,5$.

$96\ \mu m$, with which we will be in the region of nearly zero geometrical aberrations, according to experiment 1. This is chosen particularly in order to check for additional effects, deteriorating the imaging quality, which have previously been masked by geometric aberrations.

- Ability to restore the focus, if the aspheric lens is displaced along z , by moving the collimator (analog to experiment 1), checking the image quality in these restored case by transversely displacing the $50\ \mu m$ aperture in the proposed region of 0 aberrations. Thus obtaining an idea for the feasibility of changing an atom's altitude, while still keeping it trapped and moving it around.

The real major advantages of this setup are:

1. It represents the actual dipole trap system, so in order to simulate the final version, we only have to replace the $50\ \mu m$ aperture by the DMD, which is done in the 3rd experiment.
2. It is proposed to work in the regime of zero geometric aberrations, providing the opportunity to see the influence of other effects in the system, like diffraction from finite apertures or tilts of the lenses included.
3. Of course, in the case, that there were any geometrical aberrations apparent, these would also show up in the results, so we can cross- check our conclusions from the first experiment.

4.2.2 Measurements

Image shapes, properties of the aspheric lens Before looking at the measured data, a qualitative glance at the images shall be taken here, as these led us to a variety of sub-experiments, telling us more about the individual optical items in the setup.

With the aligned system, we obtained images on centre, which still comprised ring patterns surrounding the focus- spot, as in fig: 4.26.

As we do not have a situation that sensitive on longitudinal displacements of the aperture as in experiment 1 anymore, we would not expect them to originate from an aperture misalignment. In order to figure out the source of these rings, a couple of tests have been performed:

1. First the light beyond the collimator ²⁰ has been observed by imaging with a standard lens of focal length $f_i = 500\ mm$ [20], which resulted in a single spot on the CCD camera, without a ring pattern along the optical axis at all. Therefore we can conclude, that this pattern is neither generated by the collimator nor by diffraction from the aperture, as both would result in visible rings.
2. To underline this and check the influence of the mirror as well as a double path through the collimator, the normal imaging system without the aspheric lens was set up and the light reflected by PBS1 was observed. Again, no diffraction ring pattern was apparent.

²⁰transmitted through the $50\ \mu m$ aperture



Figure 4.26: Image on CCD camera for double pass through system and $50 \mu m$ aperture on axis.

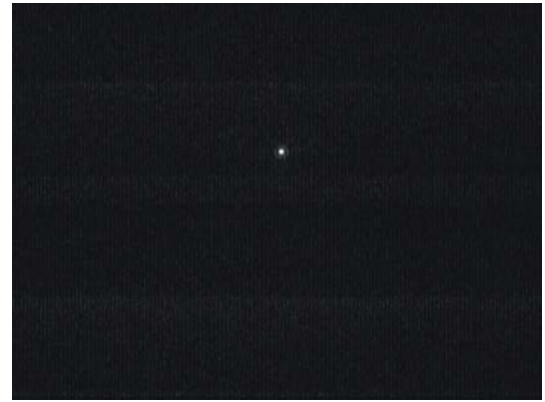


Figure 4.27: Image obtained by single pass through system on focus of aspheric lens, imaged by using a $f_i = 30 mm$ [21] lens.

3. Now we introduced the aspheric lens and created a single path system by magnifying the focus of the aspheric lens with an imaging lens ($f_i = 30 mm$ [21]), providing the image in fig: 4.27 containing rings.
4. To check, that this was not caused by the imaging lens, we observed the light $\Delta z = 10 mm$ beyond the aspheric lens with a CCD camera, showing also a ring pattern ²¹. This indicated the aspheric lens to be its source.
5. For proofing the last point, we imaged an adjustable diaphragm with the aspheric lens, so we did not have collimated light incidence on the lens. This also provided us with a ring pattern on the image, which can be treated as evidence for the claim above.
6. Trying to find out, which part of the aspheric lens caused this ring pattern, we have set the single path system again (including collimator and $50 \mu m$ aperture), observing the aspheric lens focus with a $f_i = 30 mm$ lens. This time, a variable diaphragm was positioned directly in front of the aspheric lens (object side) and the effects of closing the aperture peu a peu on the ring pattern were observed. The ring pattern decreased in intensity for smaller openings (smallest is about $d_{vd} = 850 \mu m$).
7. To check, whether this pattern can be related to an interference effect, e.g. due to bad anti- reflection coatings on the lens, creating a Fabry- Perot interferometer, the reflectivity of both aspheric lens surfaces were measured, providing an approximate reflection of $R = 0,35\%$, for nearly perpendicular incidence. Therefore an interferometer effect is highly unlikely, as after two reflections, only $12,5 \cdot 10^{-3} I_0$ would be available to interfere with the an original beam of intensity I_0 .

At the moment, we assume this pattern might be caused by the phase effects, the light experiences by propagating through the lens, related to its NA to be the limiting one for the

²¹But of low intensity, as the beam is very diverging around the focus.

system. This estimation is further discussed in the context of experiment 3. However we can conclude for sure, that our diffraction effects result from the aspheric lens and are neither subject to misalignment errors nor interference effects.

While aligning the system a couple of times, we also observed a strong dependence of the images on the tilts of the aspheric lens. If the lens is not properly adjusted, the images obtained on focus of our system get heavily distorted, see e.g. fig: 4.28, 4.29 and 4.30, showing the effects of increasing tilt ²².



Figure 4.28: Effects of a small tilt, about 1 deg, on image of focus.



Figure 4.29: Effects of a small tilt, about 5 deg, on image of focus.

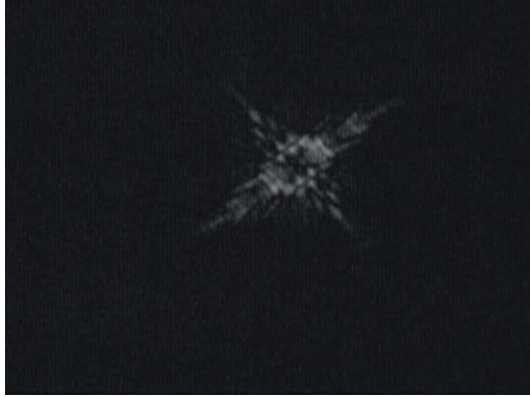


Figure 4.30: Effects of a small tilt, about 10 deg, on image of focus.



Figure 4.31: Image of focus obtained after cur-ing tilt.

However a proper image of the focus can be restored by having the aspheric lens on a tilting stage, providing images as good as fig: 4.31. To check the dependance of different parts of the lens to tilts, we performed the following experiments:

1. We illuminated the aspheric lens with the collimated, filtered light from the laser beam and observed the focus with a $f_i = 30\text{ mm}$ imaging lens. This set-up showed a high sensitivity to tilts.
2. A variable diaphragm was imaged by the lens, showing an insensitivity over a broad range

²²But keeping the tilt angle smaller than $\vartheta \approx 10\text{ deg}$.

of angles.²³

3. In the imaging system, we generated converging beam incidence on the aspheric lens, thus having a smaller spot size on its entrance pupil, by choosing $L_{C,50} = 109,5\text{ cm}$ and $L_{asph,C} = 91,5\text{ cm}$, providing insensitivity to tilts.
4. Having divergent light incidence, thus a greater spot size on the entrance pupil, by choosing $L_{C,50} = 26\text{ cm}$ and $L_{asph,C} = 89,5\text{ cm}$, serious sensitivity appeared.

This leads to the conclusion of a stronger dependence on tilts for off- axis components. It also agrees with our estimation, that the finite numerical aperture of the aspheric lens might cause the observed diffraction- like pattern. Since in the case of tilts, the off axis path- length and thus phase shifts experienced by the relevant components are influenced stronger, a tilt would result in a change of their interference at the focus. If we observe tilting effects especially for small values 4.28, we see the central spot remaining still nearly circular. The ring pattern surrounding it however rapidly shows a transition from a circular pattern into a dot pattern (as normally observed for diffraction gratings, see 4.29). As our experiments show the higher sensitivity of off- axis components to tilts, we can expect, that the ring pattern is generated by those ,since it is the most tilt- sensitive part of the image.

Displacement of the $50\mu\text{m}$ aperture in its transverse plane Starting the analysis of the quantitative data, we observed the variations of the maximum and minimum beam waist values again. We displaced the $50\mu\text{m}$ aperture for particular y- values and recorded the behaviour along x. The data for the on- axis position in y ($y == 10,65\text{ mm}$), together with values at the extremities of the observed y- range can be observed in the fig. 4.32, 4.33, 4.34 (showing the maximum beam waist) and fig: 4.35,4.36,4.37 (showing the minimum beam waist). Plots for all other data points collected, can be found in the appendix (see table 4.2 for references).

Minimum beam waists	fig: 6.22 - 6.31
Maximum beam waists	fig: 6.12 - 6.21

Table 4.2: References for additional maximum and minimum beam waist files in appendix.

As far as the trend behaviour of the minimum and maximum beam waists is concerned, we obtain interesting effects. In the minimum case, a rather constant waist in positive x- and smaller, linearly decreasing waist in negative x- direction (for negative y displacements) develops through a nearly constant region into a the opposite trend (for $\Delta y \approx 0\text{ mm}$) back to constance (for $y = approx11,20\text{ mm}$). The fluctuations are about 10% in order of magnitude. The maximum beam waist shows approximately parabolic behaviour around a central point, which is located at $x = 0\text{ mm}$ for negative y- displacements (i.e. $y < 10,65\text{ mm}$, fig: 4.32). The parabola's center moves towards positive x values (fig: 4.33), breaking the symmetry in x, and the graphs get's rather square, shaped. Positive y- values ($y > 10,65\text{ mm}$) lead to a nearly linear

²³Even with $\vartheta = 10\text{ deg}$, a nearly undistorted focus was obtainable.

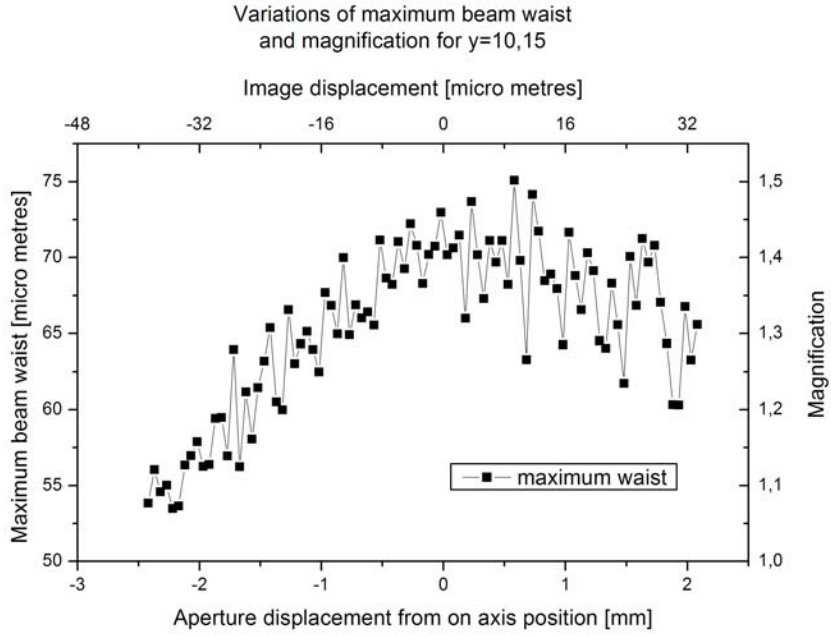


Figure 4.32: Variations of maximum beam waist along x- direction for $-0,5\text{ mm}$ relative y displacement.

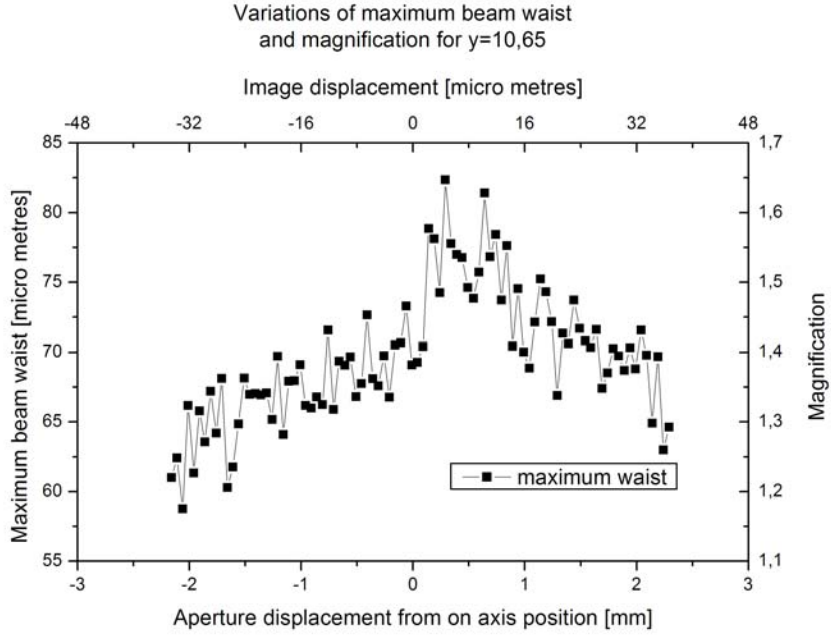


Figure 4.33: Variations of maximum beam waist along x- direction for 0 mm relative y displacement (on axis).

decrease of the overall maximum (fig: 6.16), which is not located at $x = 0\text{ mm}$. Ultimately a rather constant trend is observed for the upper bound of the y- range (fig: 4.34). Fluctuations can here be as strong as 20%. The beam waist hence shows the opposite behaviour, one would

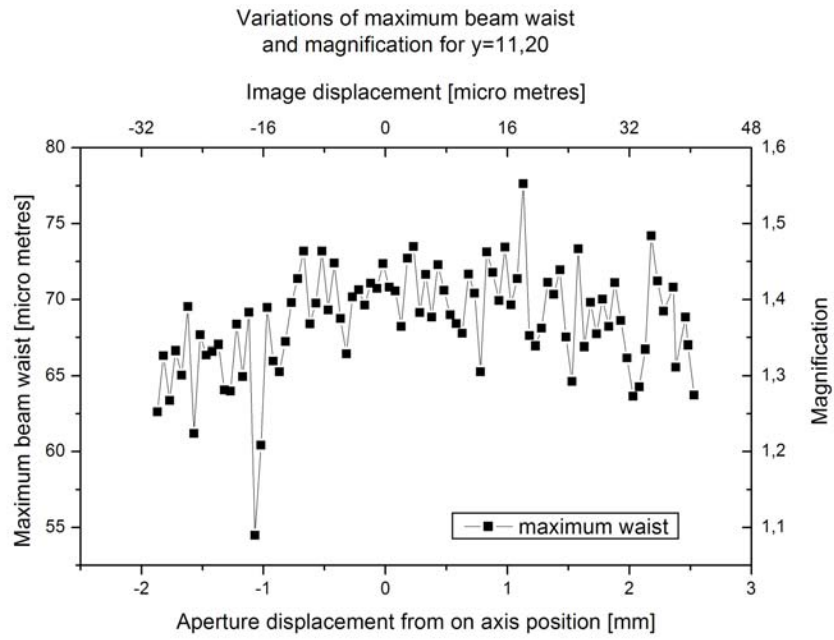


Figure 4.34: Variations of maximum beam waist along x- direction for $0,55\text{ mm}$ relative y displacement. Values for $x = -1,07\text{ mm}$, $x = -1,02\text{ mm}$ and $x = -1,13\text{ mm}$ were treated as spikes and hence neglected for further analysis.

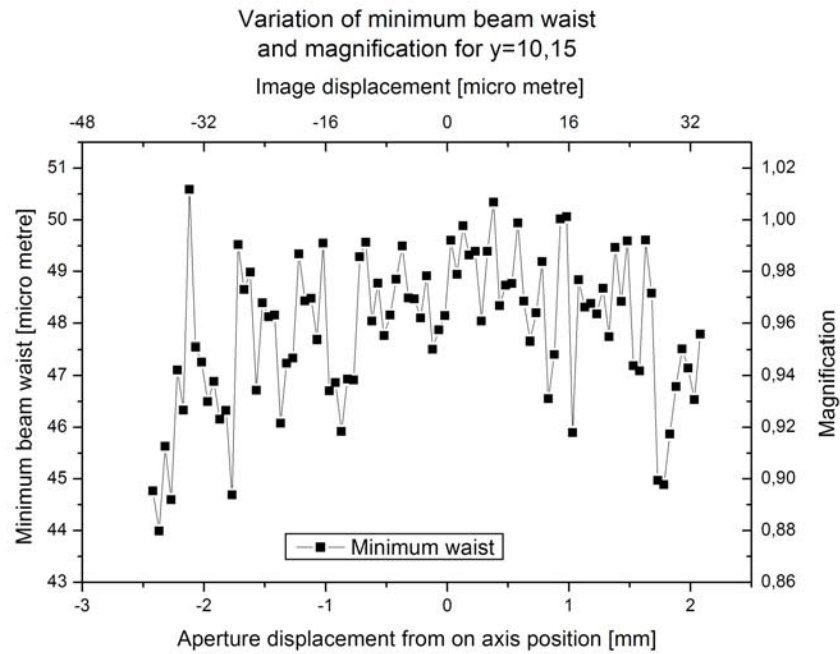


Figure 4.35: Variations of minimum beam waist along x- direction for $-0,5\text{ mm}$ relative y displacement. The value for $x = -2,12\mu\text{m}$ was treated as a spike and hence ignored for further analysis.

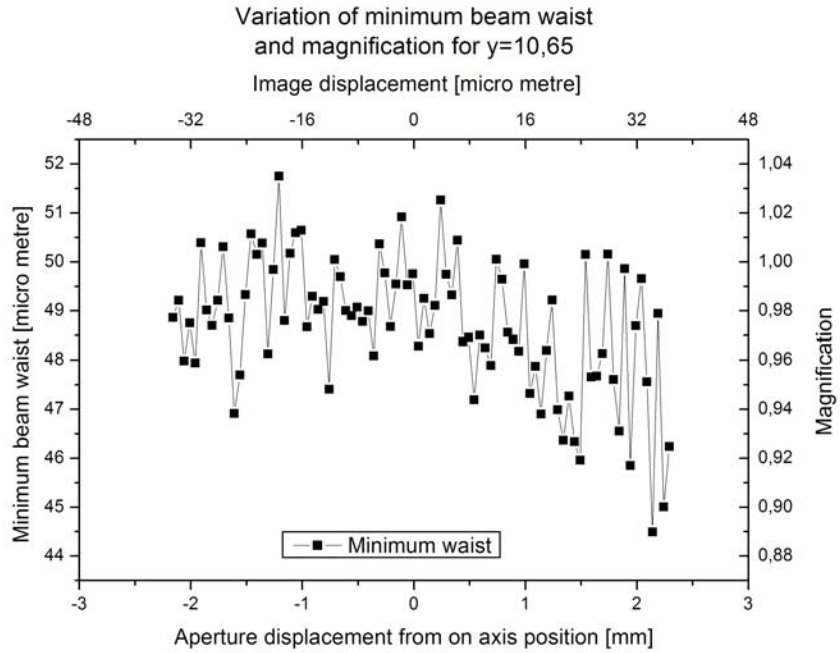


Figure 4.36: Variations of minimum beam waist along x- direction for 0 mm relative y displacement (on axis).

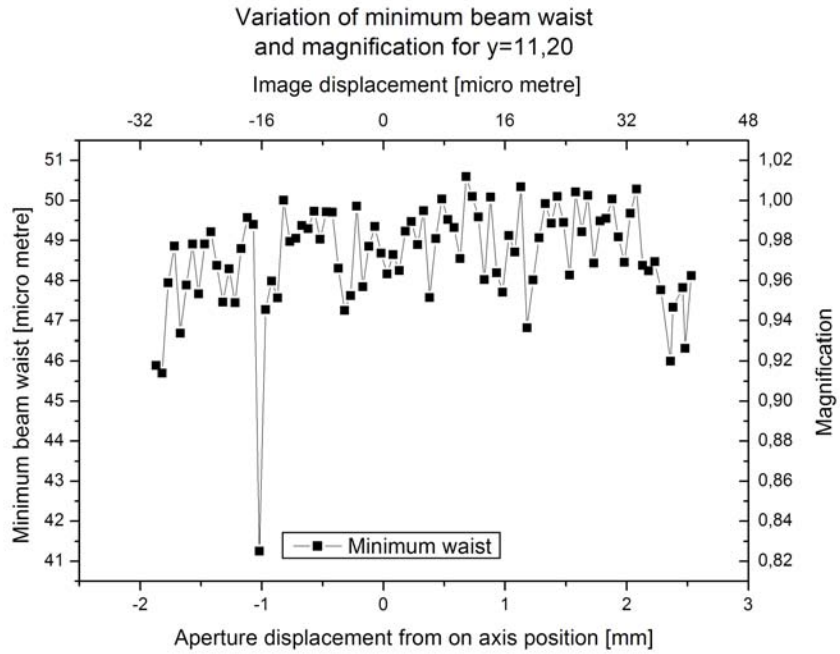


Figure 4.37: Variations of minimum beam waist along x- direction for 0,55 mm relative y displacement. The value for $x = -1,02 \mu m$ was treated as a spike and hence ignored for further analysis.

expect from geometrical aberrations; i.e. the waist values tend towards lower values further off- axis than on axis. It is obvious, that the data is subject to serious fluctuations, however

the trends in the values show a lack of symmetry around the on axis position in x. Although it is not really clear, where the specific changes in shapes of the trend- behaviour²⁴ originate from, i.e. whether they are only due to a tilt or maybe comprise some superimposed diffraction effects, the lack of symmetry around $x = 0$ for centre values in y ($y \approx 10, 4 - 10, 85$), but with having this symmetry at the boundaries of the observed y range ($y = 10, 15$ and $y = 11, 20$), raises the estimation of tilting to play a major role for the non- constance of the beam waist. The latter would have been expected, if only geometrical abberations were apparent in our system and sticking to a measurement range of their influence vanishing, would result in the aforementioned expectation. For the next part of the experiment, we can obtain a verification of this claim., but we clearly see geometrical abberations not having any influence in applied displacement ranges. That validates the data, observed in the first experiment.

Displacement of aspheric lens and restoring focus by collimator movement We have now recorded another set of data in the transverse direction for displacements of the aspheric lens along the optical axis of $\Delta z = -5 \mu m, \pm 10 \mu m, \pm 20 \mu m$. The two parameters in the x and y direction for $\Delta z = \pm 10 \mu m$ can be seen in the plots fig: 4.41, 4.40 and fig: 4.39, 4.38. Plots for $\Delta z = -5 \mu m$ and $\pm 10 \mu m$ in x and y, are obtainable in the appendix (see table 4.3)

x direction	fig: 6.33, 6.36, 6.34
y direction	fig: 6.32, 6.35, 6.37

Table 4.3: Reference table for additional beam waist plots in the appendix.

The data is very interesting in terms of its trends: If we look at the beam waist plots (fig: 4.41, 4.40 and 4.39, 4.38) and go for a direct comparison in terms of maximum beam waists, we can see for $\Delta z = +10 \mu m$ displacement the waist in y to be approximately symmetric to $y = 0 \mu m$, decreasing slightly off centre²⁵. The waist in x however increases linearly and is not symmetric to the on-axis position. This asymmetry is even better obtained for the $\Delta z = -10 \mu m$ dislocation, in which case we have linear increase in waist towards positive x displacements (fig: 4.41) and linear decrease towards positive y values (fig: 4.40).²⁶

That means, the system is not symmetric in x and y; geometrical abberations cannot break the cylindrical symmetry of a lens system (despite their already proven absence), neither can diffraction effects from circular lenses. The only effect which is able to provide these features are tilts of the individual lenses. This strongly makes us anticipate a tilt to be a reason for the severe deviations from constant behaviour in the data sets from this experiment: If the beam waist variations were due to abberation or diffraction effects, they would be symmetric in x and y, like it was obtained in the first experiment. But as they are clearly not, this indicates

²⁴e.g. parabolic in x for $y = 10, 15 mm$, but square shaped for $y = 10, 20 mm$

²⁵looking like a very shallow parabolic

²⁶Please note here, that the $\Delta z < 0 \mu m$ values have been recorded first, so the $\Delta z > 0 \mu m$ data might be subject to increased systematic errors.

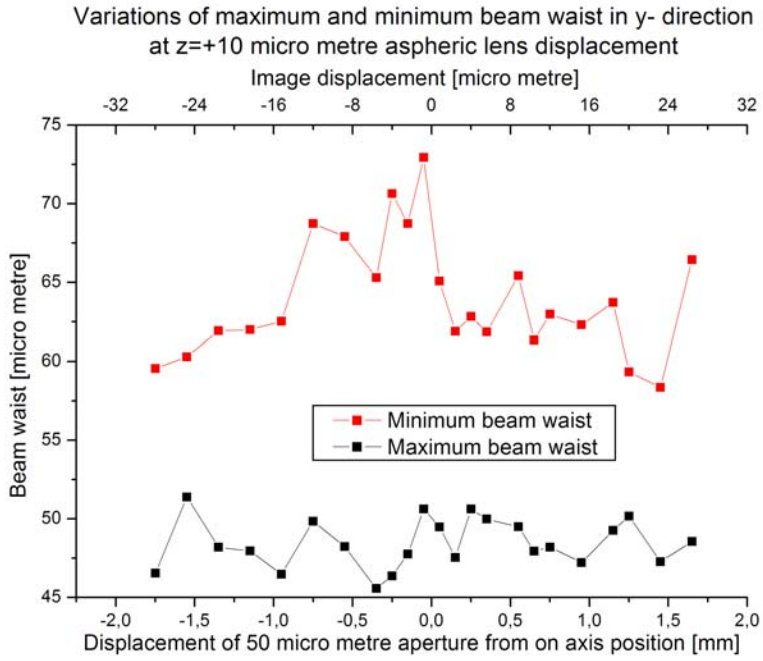


Figure 4.38: Maximum and minimum beam waists as a function of y- displacement with aspheric lens $z = 10 \mu\text{m}$ displaced.

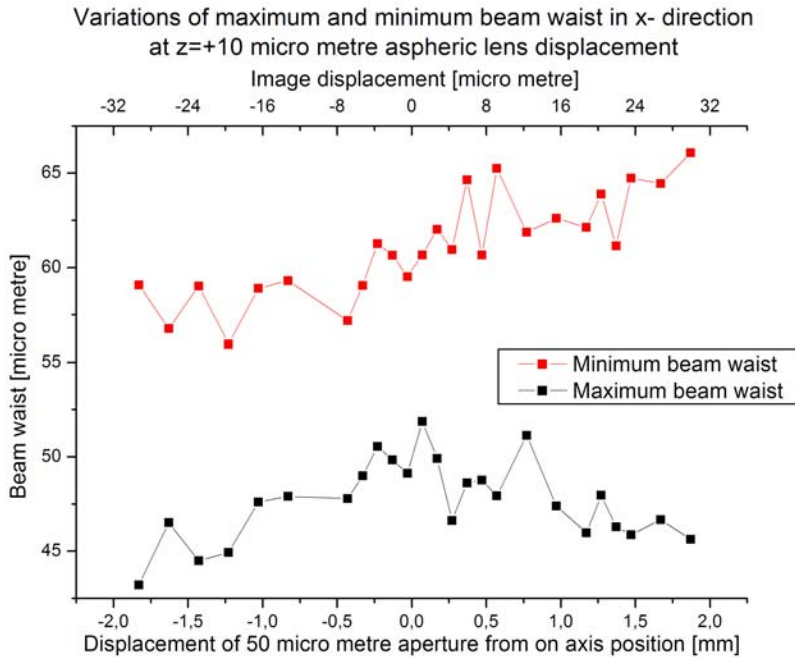


Figure 4.39: Maximum and minimum beam waists as a function of x- displacement with aspheric lens $z = 10 \mu\text{m}$ displaced.

breaking of symmetry, which can only be caused by a tilt in the aspheric lens ²⁷.

²⁷Tilts in the collimator alignment have been proven negligible, due to the lever effect, resulting from the system's magnification

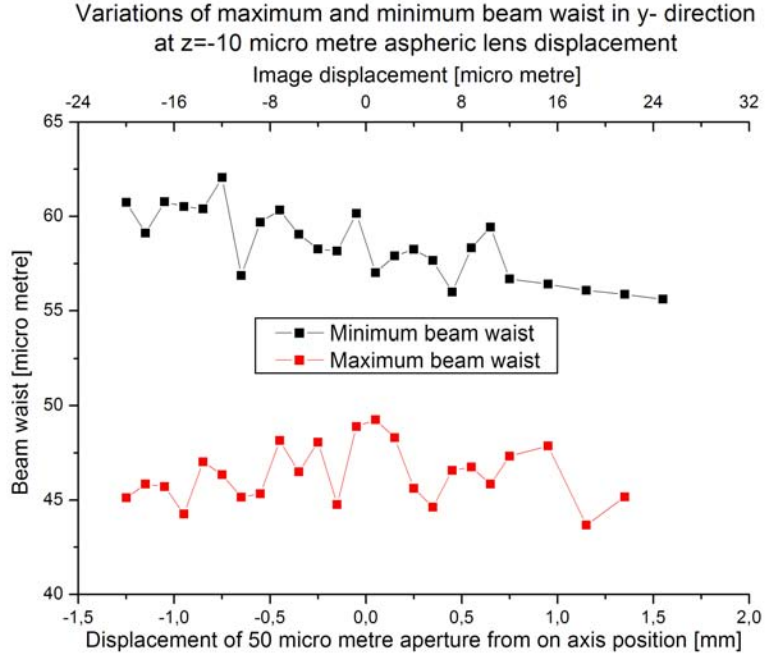


Figure 4.40: Maximum and minimum beam waists as a function of y- displacement with aspheric lens $z = -10 \mu\text{m}$ displaced.

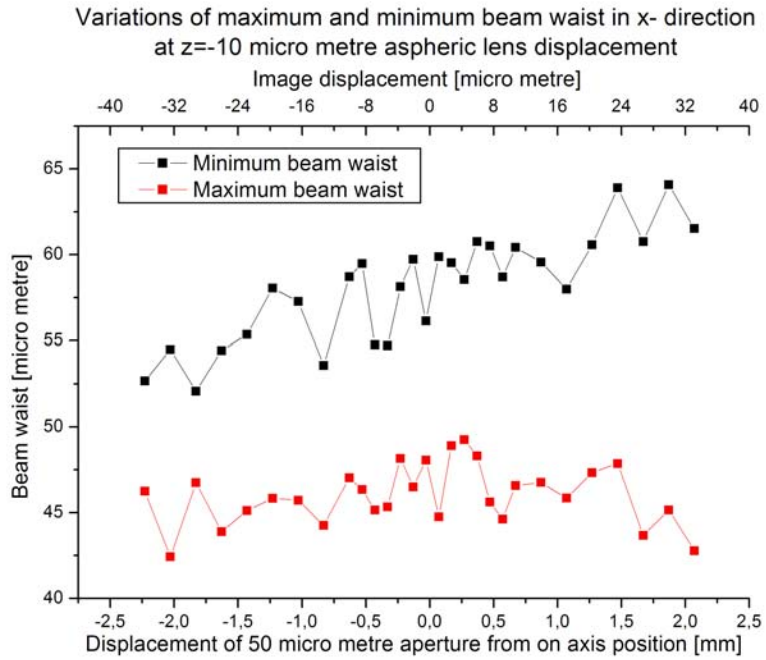


Figure 4.41: Maximum and minimum beam waists as a function of x- displacement with aspheric lens $z = -10 \mu\text{m}$ displaced.

This shows the high sensitivity of the imaging system on misalignment. Particularly since we have adjusted this system for zero tilts, as far as one could tell from the back- reflected beam shape on the CCD, the apparent values indicate the requirement of doing a testing measurement,

like the one presented, in order to control the alignment.

The good news however is, that we can conclude the absence of geometrical aberrations for different positions of the focus along the optical axis; i.e. we will be able to change the altitude of the trapping potential above the mirror surface in the MOT without having aberrations apparent, causing the loss of the trapped atom. This also means, that we will be able to compensate for a misalignment in the height of the aspheric lens above the mirror²⁸ without running into trouble with the quality of the trapping potential.

The distances required to restore the focus can be found in table 4.4.

$\Delta z[\mu m]$	Displacement of collimator [cm]
+20	$9,25 \pm 0,1$
+10	$3,95 \pm 0,1$
0	$1,47 \pm 0,1$
-5	$2,35 \pm 0,1$
-10	$4,9 \pm 0,1$
-10	$8,95 \pm 0,1$

Table 4.4: Distances required to restore the system's focus by displacement of the aspheric lens along the optical axis.

We also measured the displacement from the original position in order to restore the focus for $\Delta z = 0 \mu m$, after measuring all other values. The deviation of $1,47 cm$ provides an idea of the uncertainties, obtained from the translation stage hysteresis. The data indicates this systematical error to be $\Delta z_{sys} \approx 3,76 \mu m$, still large enough however to cause a severe uncertainty for displacements on the image side (aspheric lens- mirror- system). Comparing the values with the ones from experiment 1, we obtain coincidence within the uncertainty range of $\approx 1,5 cm$. This shows the reproducibility for specific focus dislocations of the imaging system and therefore indicating our ability to change the altitude of the trap- potential by the collimator in a controlled manner.

4.2.3 Trap- potential

The collected data from the displacements of the $50 \mu m$ aperture in its transverse plane can now be applied to calculate the changes of the trap- potential as the tweezers focus is moved around. According to 3.12 and 3.14 we obtain for the potential:

$$U = -\frac{\hbar\delta}{2} - \frac{\hbar I_0(x, y) w_0^2(x, y)}{8\tau_e^2 |\delta| w^2(x, y, z) I_{sat}} \exp\left(-2\left(\frac{\sqrt{x'^2 + y'^2}}{w(x, y, z)}\right)^2\right) \quad (4.7)$$

This equation comprises two independent coordinate systems, one for the atom (x', y'), providing the potential values it experiences in the trap, and a second one for the position of the trap (x, y), which gives the relevant trapping parameters as it is dislocated in 3d. For

²⁸e.g. due to lacking precision in manufacturing the lens holder

the calculation we will limit ourselves to displacements of the trap along the x- axis and only consider atomic motion along x' . Further the potential will be modeled in the focus of the laser beam, i.e. $w(x, y, z) = w_0(x, y)$. Unfortunately we cannot deal with the real values of I_0 here, as we could not measure them with the CCD. Therefore we made the rough approximation of a constant intensity over the traps dislocation range, yielding:

$$U \approx -\alpha \exp \left(-2 \left(\frac{x'}{w_0(x)} \right)^2 \right) \quad (4.8)$$

Although appearing crude, it is sensible, as the beam waist is not changing massively: so as the energy within the image spot must be conserved, the peak intensity does approximately not vary too much either. The additional term $\frac{\bar{\omega}}{\hbar\delta}2$, relying on the laser- frequency detuning, has been neglected, as it only provides a potential offset, but no trapping. We have also set the constant $\alpha = 1$, to receive relative values.

Inserting the data obtained for $\Delta y = 0 \mu m$ and using the minimum beam waist values for $w_0(x)$ results in a change of the potential as shown in fig: 4.42, the graph for applying the maximum waist can be found 4.43.

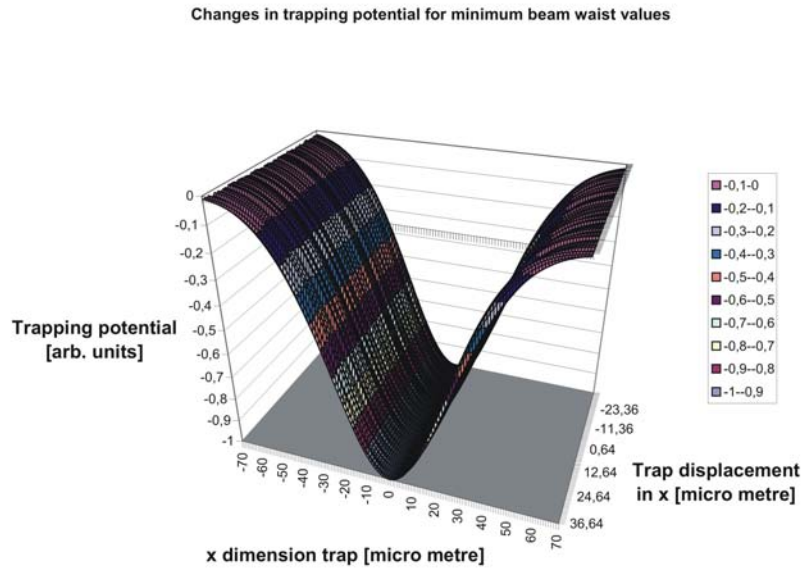


Figure 4.42: Resulting changes in the trapping potential in x' - direction for trap displacement in x, with y- position on axis, using minimum waist values.

We see, that despite the measured waist fluctuations, the width of the potential is approximately constant over the displacement range ²⁹. The changes of the oscillation frequencies of the atomic motion in the trap, as well as the energy level values, both depending on the well width, can therefore be anticipated from these plots to be also nearly constant over the displacement region, which is good news. So moving an atom around should not perturb its excitation levels and hence information stored that way will not be lost by dislocating the atom.

²⁹which corresponds to the expectations, since w_0 shows up in the exponential term only

Normalised trapping potential variations for maximum beam waist values

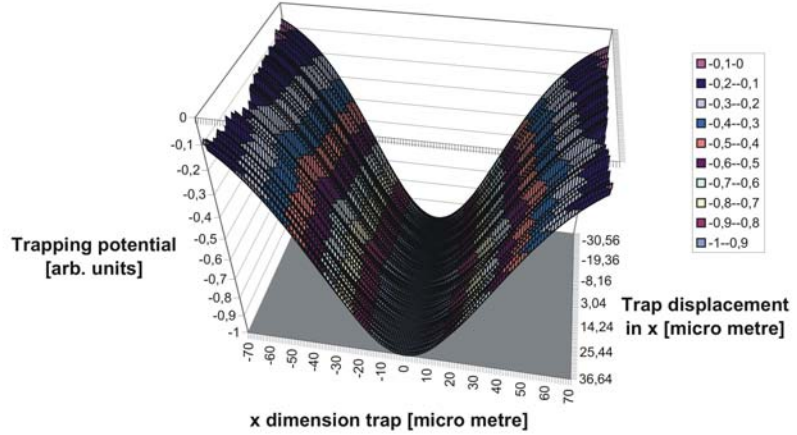


Figure 4.43: Resulting changes in the trapping potential in x' - direction for trap displacement in x , with y - position on axis, using maximum waist values.

4.3 Experiment 3

Alignment This last experiment deals with the replacement of the aperture by the DMD (see fig: 4.44). In order to set-up the final experiment, alignment of the optical components according to the developed scheme is favourable, requiring a means to swap the aperture by the DMD, which is developed here.

The DMD must be aligned under an illumination angle of $\vartheta = 22$ deg to the imaging system's optical axis. Enabling feasibility in practice, this angle cannot simply be adjusted by measuring distances with a tape. To obtain the desired illumination, we applied the following scheme:

1. We mark the previous beam path for the $50\mu m$ aperture illuminating by using adjustable

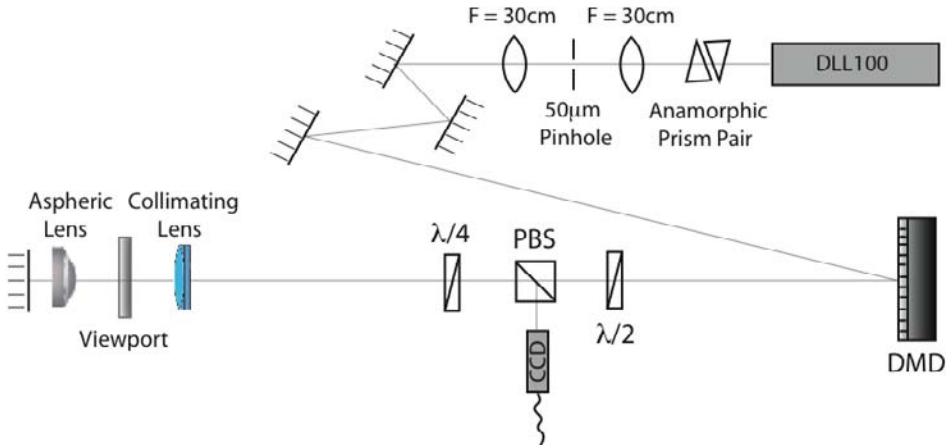


Figure 4.44: Setup sketch for system including DMD

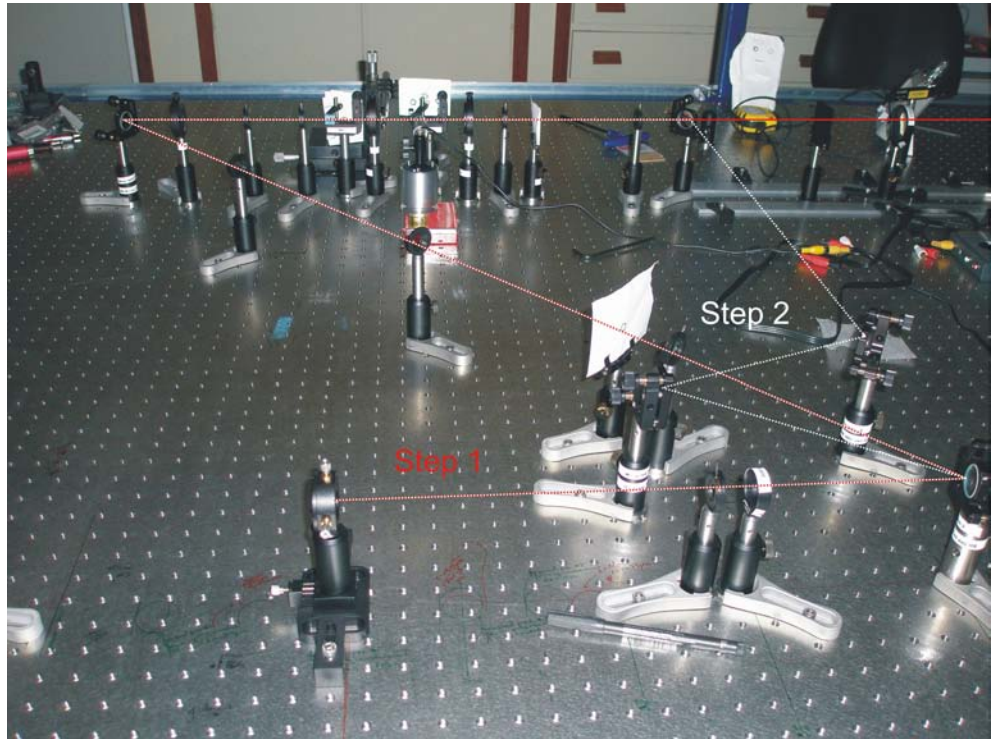


Figure 4.45: First part of the DMD alignment: Reversing the path of the incident light.

- diaphragms along the beam line and withdraw the $50\ \mu m$ aperture (see fig. 4.45).
2. This path is reversed by including a mirror (M_{rev}) in front of the collimator, which is adjusted to reflect the light through the exact same path, indicated by the diaphragms (fig. 4.45).
 3. Then the DMD is included at the focal point of the collimator with its screen \perp to the optical axis.
 4. The light path of the reversed beam reflected off the DMD screen is marked by diaphragms as well (fig. 4.46).
 5. Thereafter M_{rev} is taken out and the DMD gets illuminated through the beam path marked in 3. (fig. 4.46).

This scheme resulted in appropriate imaging, obtained by the system, and offers a convenient last step in building the dipole trap later on, as it allows the imaging system to be aligned separately with subsequent inclusion of the DMD. Therefore we know now how to built the real system and align it properly ³⁰.

Imaging with the DMD In order to check the system's imaging qualities including the DMD, we applied a $50\ \mu m$ spot and got it displaced in its transverse plain along the x- direction. An image of the spot, as seen on the CCD, is given in fig: 4.47, similar to the ones obtained

³⁰Unfortunately this was not feasible within the limitations of this project anymore

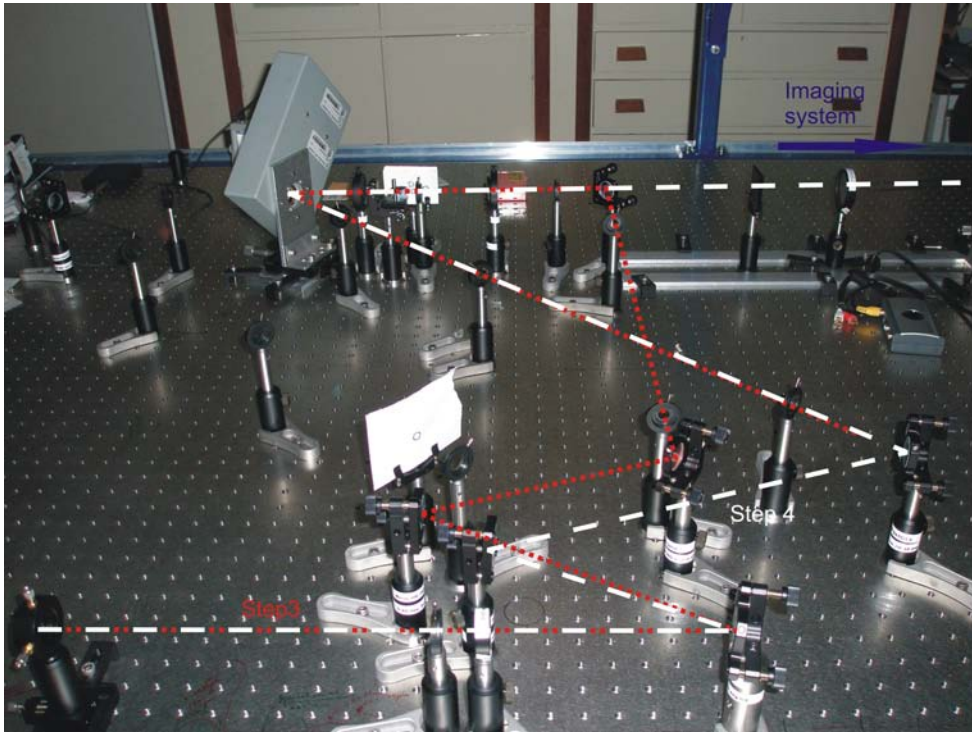


Figure 4.46: Second part of DMD alignment: Reversed beam, incident from the imaging system side, gets reflected on DMD screen and its path is marked by diaphragms.

from imaging the $50 \mu\text{m}$ aperture. The results of the dislocations on the beam waists are shown in fig: 4.49, which are in the correct order of magnitude and comprise the fluctuations seen previously, but no indication for geometric aberrations,³¹as we operate in a regime, which should be free those, according to our previous experiments.

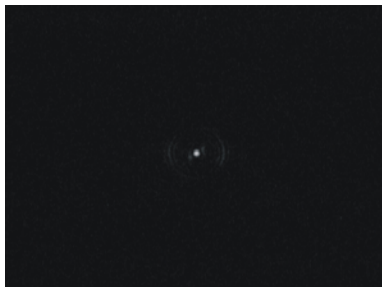


Figure 4.47: Image obtained by applying $50 \mu\text{m}$ circle on DMD screen.



Figure 4.48: Oxford physics logo, as applied on the DMD for imaging; source: [29]

To obtain a more complicated and fancier image, we tried to image the "Oxford Physics" logo, as shown in fig. 4.48, and separately the φ within it. The measured images are provided in fig. 4.51 and fig. 4.50, comprising distortion effects on top of them combined with unsharpened

³¹Note here the error resulting from the fitting routine once more, mixing up maximum and minimum beam waist between $-0,8 < x < -0,7$ and $0 < x < 0,6 \text{ mm}$ displacement.

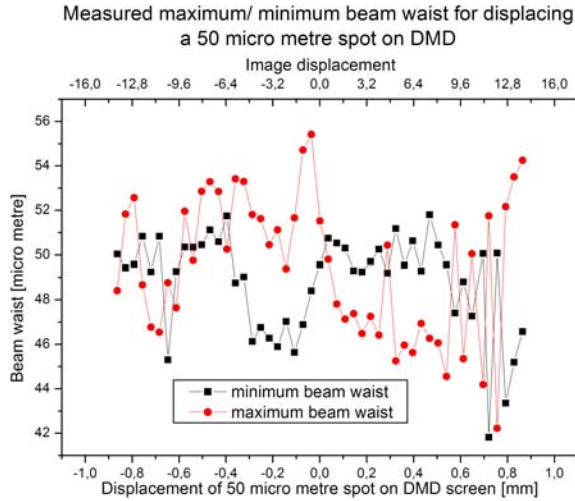


Figure 4.49: Maximum and minimum beam waists for moving $50 \mu\text{m}$ circle in x- direction on DMD screen.

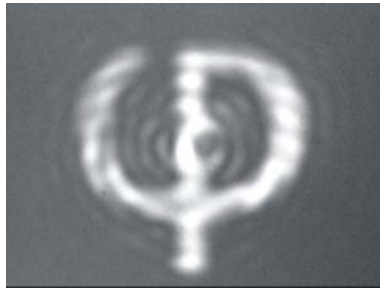


Figure 4.50: Image of the Oxford physics phi.

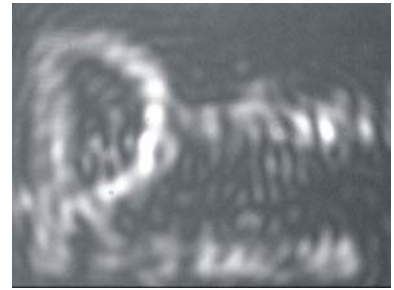


Figure 4.51: Image of the Oxford physics logo.

edges.

The latter can be easily understood by applying the Rayleigh criterion for imaging. As the system operates like a microscope, the resolution limit (r_{min} = minimum distance between two points for them to be resolved) on the image plane³² is limited by the NA of the system, provided by the boundaries of the aspheric lens (NA=0,546), giving [25]:

$$r_{min} = 0,6098 \frac{\lambda}{NA} = 0,871 \mu\text{m} \quad (4.9)$$

In back reflection, this has to be multiplied by the magnification [25], yielding:

$$r_{min,back} = 62,5 \cdot r_{min} \approx 54,5 \mu\text{m} \quad (4.10)$$

So items on the DMD can only be resolved, if they are $\Delta r \geq 4 \text{ pixels}$ apart from one-another³³. Henceforth it is clear, why we do not get clear image edges, as these would require

³²i.e. the mirror

³³The reader should note here, that this resolution was desired on purpose. As we require an object size of $50 \mu\text{m}$ on the DMD (corresponding to 4 pixels in diameter) to obtain the desired single atom trap, we do not

resolving every single pixel, having a $r_{min,back} \leq 13,6 \mu m$.

The distortion seen by a superimposed ring- pattern- like structure is more complicated and originates from the aspheric lens once more.

Currently we anticipate all of these effects to be caused by the limited NA of the aspheric lens. In terms of Fourier optics, propagating through a lens always requires solving an integral over the aperture containing the object's transparency and the transfer function of the lens. In this expression, resulting from various distance vectors, quadratic phase terms are apparent [26], containing the coordinates of the aperture. By propagating through the lens and thus solving this integral, these terms normally get neglected on the basis of the limiting aperture to be large compared to the incident beam diameter. In our system, this is not the case, as the diverging beam from e.g. the $50 \mu m$ spot has a large diameter once it is collimated and impinging on the lens. Unfortunately, the original simulation of the system using *Zeemax*[©] did not take this effect into account, so a simulation in terms of physical optics was written in *MatLab*[©], relying on the full propagation forth and back through the system, but still using the thin lens approximation and the paraxial approximation ³⁴.

The results so far show this ring pattern effect (see fig. 4.53 for the original object, 4.52 for the image, obtained on the mirror, and 4.54 for the image in back-reflection) at the edges, which get enhanced during back- reflection, as well as some distortion within the image. These effects are smaller than the ones observed experimentally, but the simulation still relies on the above stated approximations ³⁵, which are most- likely not valid in the experiment. So further investigation will be required here.

want a higher resolution, since otherwise the single pixels, contributing to the object, will be resolved and we do not obtain a homogeneous trapping potential.

³⁴These simulations were performed by the post- doc in our group, Edouard Branis.

³⁵Deviations from these two approximations could not be performed yet, as the simulations were constrained by the computational power available.

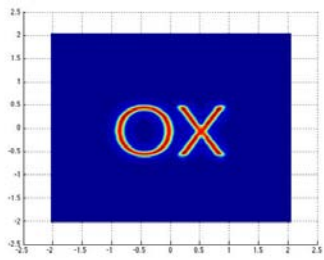


Figure 4.52: Image obtained from the simulations after a single pass through the system on the mirror surface.

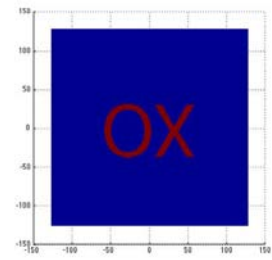


Figure 4.53: Object applied to be imaged by the system in the simulations, showing its field amplitudes.

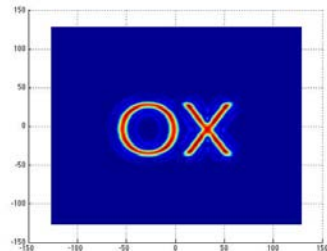


Figure 4.54: Image obtained from the simulations in back-reflection through the system, showing its field amplitudes.

Chapter 5

Conclusions

This MSc project dealt with setting up and testing of the imaging optics for creating an optical dipole trap. The future trap should be able to move single atoms in 3D for applications in cavity QED and quantum information processing. The basic principles of the optical dipole trap have therefore been developed in the first place, clearly stating the fundamental principles behind optical trapping and cooling as well as the special requirements for our experiment. In addition our system is described in further detail.

The optical system, consisting of a collimator lens ($f_C = 750\text{ mm}$) and an aspheric lens ($f_{asph} = 12\text{ mm}$), is supposed to operate in its 2f- configuration, with a digital mirror array (DMD) placed in the collimators' focal point, creating the trapping potential in the focal point of the aspheric lens. For testing this system, 2 different experiments were performed. First a $1\mu\text{m}$ aperture has been placed into the focal plane of the aspheric lens, and the light imaged by the collimator was observed. As a function of the position of this aperture, the associated image was analysed to obtain the waists. Thus an idea of geometric abberations within the system was obtained, showing an abberation- free range of $\Delta(x, y) \approx 90\mu\text{m}$ in tital around the optical axis. Furthermore the ability to displace the systems' focus along the optical axis was checked by dislocating the aspheric lens a certain distance and restoring the focus with the collimator. Providing approximately a required movement for the collimator of $\Delta z_C \approx 9\text{ cm}$ for an aspheric lens dislocation of $\Delta z_{asph} \approx 20\mu\text{m}$ this also provided the expected value for the longitudinal magnification. Second, the system was operated by placing a $50\mu\text{m}$ aperture in the focal plane of the collimator and reflecting the light back through the system with a mirror placed in the focal plane of the aspheric lens. Setting- up this system resulted in a possible route to align the imaging system in the dipole trap set-up. Observing the images in back- refction through the system, offered information about the systems behaviour in a regime free of geometrical abberations. A ring structure surrounding the central focal point was endavoured to originate from the aspheric lens, whose tilts appeared to severely influence the ability to obtain clear images. This ring structure is subject to limitations due to the NA of the aspheric lens and associated effects on the phases of the light. The ability to move the focus along the optical

axis was verified in this setup as well, showing the displacements for the collimator to coincide with the expectations for longitudinal magnifications and providing an insensitive lever to focus the system.

The last achievement was to include the DMD into the aligned imaging setup and to observe the imaging properties of the system with the DMD, which enabled us to resolve simple images and also showed further evidence for effects of the aspheric lens on the phase of the light.

Overall, the outcome of this project provides a route towards an optical dipole trap for single atoms, operating in the diffraction limited regime. Although the final step in building the trap and moving around a single atom is still pending, sufficient knowledge has been obtained to create a single atom trapping potential. Due to the complexity of the diffraction limited microscope setup, it was not possible to analyse all the effects, comprised by the aspheric lens within the limited time-frame of this project.

Chapter 6

Appendix

6.1 Mathematical derivation of Rabi- oscillations

Starting from the Schrödinger equation with the appropriate interaction term for a dipole transition, driven by an external electro-magnetic field

$$H|\Phi\rangle = -\frac{p^2}{2m}|\Phi\rangle - eE(r,t) \cdot r$$

the atomic wave-function for the perturbed case can be written as a linear combination of the unperturbed Eigenstates $|\Phi_i\rangle$ of the atom:

$$|\Psi\rangle = \sum_i c_i(t)|\Phi_i\rangle e^{-i\omega_i t}$$

Inserted into the Schrödinger- equation, this yields:

$$i\hbar \frac{d}{dt} \sum_i c_i(t)|\Phi_i\rangle e^{-i\omega_i t} = (H_0 + H') \sum_i c_i(t)|\Phi_i\rangle e^{-i\omega_i t} \quad (6.1)$$

$$i\hbar \sum_i |\Phi_i\rangle \frac{d}{dt} (c_i(t)e^{-i\omega_i t}) = (H_0 + H') \sum_i c_i(t)|\Phi_i\rangle e^{-i\omega_i t} \quad (6.2)$$

$$i\hbar \sum_i \langle \Phi_k | \Phi_i \rangle \frac{d}{dt} (c_i(t)e^{-i\omega_i t}) = \sum_i c_i(t) \langle \Phi_k | H_0 | \Phi_i \rangle e^{-i\omega_i t} + \sum_i c_i(t) \langle \Phi_k | H' | \Phi_i \rangle e^{-i\omega_i t} \quad (6.3)$$

$$i\hbar \sum_i \delta_{i,k} \frac{d}{dt} (c_i(t)e^{-i\omega_i t}) = c_k(t) E_k e^{-i\omega_k t} + \sum_i c_i(t) H'_{k,i} e^{-i\omega_i t} \quad (6.4)$$

$$i\hbar \frac{d}{dt} c_i(t) - c_k \hbar \omega_k = c_k(t) \hbar \omega_k + \sum_i c_i(t) H'_{k,i} e^{i(\omega_k - \omega_i)t} \quad (6.5)$$

$$i\hbar \frac{d}{dt} c_i(t) = \sum_i c_i(t) H'_{k,i} e^{i\omega_k t} \quad (6.6)$$

Opposing to the normal quantum mechanics approach, treating all higher order probabilities $|c_k| << 1$, in the case of laser cooling this cannot be accomplished since stimulated absorption from a narrow bandwidth, high intense laser beam definitely causes upper state excitations

of recognizable quantity. However laser beams for cooling of atoms generally only couple one specific ground state to one well defined excited state; hence the sum in 6.6 will only consist of two contributing states, defined as $|g\rangle$ for ground state, and $|e\rangle$ for excited state:

$$i\hbar \frac{d}{dt}c_g(t) = c_e(t)H'_{g,e}e^{-i\omega_a t} \quad (6.7)$$

$$i\hbar \frac{d}{dt}c_e(t) = c_g(t)H'_{e,g}e^{i\omega_a t} \quad (6.8)$$

where ω_a is the energy splitting between ground and excited state: $\omega_a = \frac{\omega_e - \omega_g}{\hbar}$. An incident monochromatic light- wave of the form

$$E(\vec{r}, t) = \vec{E}_0 \cos(kz - \omega_l t)$$

leads to an interaction- Hamiltonian of:

$$H'_{e,g} = -eE_0 < e|\vec{r}|g > \cos(kz - \omega_l t) = \hbar\Omega \cos(kz - \omega_l t)$$

with $\Omega = -\frac{eE_0}{\hbar} < e|\vec{r}|g > = \Omega^*$ being the Rabi- frequency of the particular atomic transition under view ¹.

The coupled differential equation (6.7,6.8) can be solved for the time evolution of the excited and ground states by differentiating one and insertion in the other, which yields (see Ref: [1]):

$$\frac{d^2c_g(t)}{dt^2} - i\delta \frac{dc_g(t)}{dt} + \frac{\Omega^2}{4}c_g(t) = 0 \quad (6.9)$$

$$\frac{d^2c_e(t)}{dt^2} + i\delta \frac{dc_e(t)}{dt} + \frac{\Omega^2}{4}c_e(t) = 0 \quad (6.10)$$

where $\delta = \omega_l - \omega_a$ is the laser's detuning from the actual atomic resonance frequency. These equations have the solutions ([1]):

$$c_g(t) = \left(\cos\left(\frac{\sqrt{\omega^2 + \delta^2}t}{2}\right) - i\frac{\delta}{\sqrt{\Omega^2 + \delta^2}} \sin\left(\frac{\sqrt{\Omega^2 - \delta^2}t}{2}\right) \right) e^{i\frac{\delta t}{2}} \quad (6.11)$$

$$c_e(t) = -i\frac{\Omega}{\sqrt{\Omega^2 + \delta^2}} \sin\left(\frac{\sqrt{\Omega^2 - \delta^2}t}{2}\right) e^{-i\frac{\delta t}{2}} \quad (6.12)$$

$$(6.13)$$

which are the Rabi- oscillations in the occupation constants for the ground and the excited state.

6.2 Derivation of the light shift

The equations 6.7and 6.8 can be written as ²

¹In order to be able to take the oscillation term $\cos(kz - \omega_l t)$ out of the integral $< e|\vec{r}|g >$, the dipole approximation has been made. This consists of neglecting the oscillations of the electromagnetic field over the dimensions of the atom. As for our purposes light of around $\lambda = 780 nm$ wavelength being used, and the typical size of an atom being within the Angstroem regime, this approximation tends to be very suitable.

²The spatial varying part $\sim \cos(kz)$ is neglected in this case.

$$i\hbar \frac{d}{dt} c_g(t) = c_e(t) \frac{\hbar\Omega}{2} (e^{i(\omega_l - \omega_a)t} + e^{-i(\omega_l + \omega_a)t}) \quad (6.14)$$

$$i\hbar \frac{d}{dt} c_e(t) = c_g(t) \frac{\hbar\Omega}{2} (e^{i(\omega_l + \omega_a)t} + e^{-i(\omega_l - \omega_a)t}) \quad (6.15)$$

In both equations, one can neglect the oscillating part proportional to $e^{i(\omega_l + \omega_a)t}$, as this one varies at such high a frequency, that it averages out over the interaction time. This is known as the rotating wave approximation [1]. Hence only terms with $\omega_l - \omega_a = \delta$ remain:

$$i\hbar \frac{d}{dt} c_g(t) = c_e(t) \frac{\hbar\Omega}{2} (e^{i\delta t}) \quad (6.16)$$

$$i\hbar \frac{d}{dt} c_e(t) = c_g(t) \frac{\hbar\Omega}{2} (e^{-i\delta t}) \quad (6.17)$$

In order to obtain the eigenvalues of this couple system, getting rid of the oscillating terms would be desirable. This can be yielded by using the following transformation (see also [2]):

$$c'_g = c_g e^{-i\frac{\delta t}{2}} \quad (6.18)$$

$$c'_e = c_e e^{i\frac{\delta t}{2}} \quad (6.19)$$

Insertion of this into 6.16 and 6.17 results after some simplifications in

$$i \frac{dc'_g}{dt} = \frac{\delta}{2} c'_g + \frac{\Omega}{2} c'_e \quad (6.20)$$

$$i \frac{dc'_e}{dt} = -\frac{\delta}{2} c'_e + \frac{\Omega}{2} c'_g \quad (6.21)$$

Which can be written in the eigenvalue- matrix [2]:

$$\begin{pmatrix} \frac{\delta}{2} - \lambda & \frac{\Omega}{2} \\ \frac{\Omega}{2} & -\frac{\delta}{2} - \lambda \end{pmatrix} \cdot \begin{pmatrix} c'_g \\ c'_e \end{pmatrix} = 0 \quad (6.22)$$

Leading to the characteristic polynomial of

$$\lambda = \pm \frac{1}{2} \sqrt{\Omega^2 + \delta^2}$$

As λ is in frequency terms, this causes a shift in the energy levels of:

$$\Delta E_{e,g} = \pm \frac{\hbar}{2} \sqrt{\Omega^2 + \delta^2}$$

This is known as the light shift.

6.3 Optical Bloch equations

For cooling down atoms and trapping them, force has to be applied on the atom. This can be achieved by photon absorption and emission, resulting in momentum transfer or establishing of

a potential landscape. As the effects of cooling and trapping also include spontaneous emission³ we will have to deal with these effects by referring to the density matrix description⁴.

For a two level system, the density matrix contains only mixture terms of the upper and lower states:

$$\rho = \begin{pmatrix} c'_e c_e^{'} * & c'_e c_g^{'} * \\ c_g' c_e^{'} * & c_g' c_g^{'} * \end{pmatrix} = \begin{pmatrix} \rho_{ee} & \rho_{eg} \\ \rho_{ge} & \rho_{gg} \end{pmatrix}$$

Within the matrix ρ , the diagonal elements describe to occupation probabilities of the ground or excited states. The nondiagonal elements are referred to as coherences, indicating the strength of transitions from ground to excited state or vice versa.

Our equations system 6.20 and 6.21 can now be transferred into a set of coupled equations, describing the development of the coefficients in the density matrix, which is called the optical Bloch equations. This set also includes the decay of the upper state, due to spontaneous emission, via an exponential decay described by a probability γ , which equals the natural linewidth of the excited state⁵. Unfortunately the derivation of this is rather tedious and does not gain any further insight into the subject; therefore the Bloch equations will simply be stated here and the reader might be referred to the ref. [2] and [1]:

$$\frac{du}{dt} = \delta v - \frac{\gamma}{2} u \quad (6.23)$$

$$\frac{dv}{dt} = -\delta u + \Omega w - \frac{\gamma}{2} v \quad (6.24)$$

$$\frac{dw}{dt} = -\Omega v - \gamma(w - 1) \quad (6.25)$$

Here the variables (u, v, w) are linear combinations of the various coefficients in the density matrix:

$$u = \rho_{eg} + \rho_{ge} \quad (6.26)$$

$$v = -i(\rho_{eg} - \rho_{ge}) \quad (6.27)$$

$$w = \rho_{gg} - \rho_{ee} \quad \text{population difference} \quad (6.28)$$

$$(6.29)$$

In the steady state, i.e. $\frac{d(u,v,w)}{dt} = 0$, these equations have the solutions [2]:

$$\begin{pmatrix} u \\ v \\ w \end{pmatrix} = \frac{1}{\delta^2 + \frac{\Omega^2}{2} + \frac{\gamma^2}{4}} \begin{pmatrix} \Omega\delta \\ \Omega\frac{\gamma}{2} \\ \delta^2 + \frac{\gamma^2}{4} \end{pmatrix} \quad (6.30)$$

Furthermore it will become useful to express the upper state excitation in terms of w ⁶ [2]:

³Doppler cooling results form spontaneous emission entirely.

⁴The reader can find the fundamental properties of the density matrix method in the references [3] and [4]

⁵ $\gamma \sim \frac{1}{\tau}$, where τ is the upper state lifetime.

⁶Bearing in mind there, that $\rho_{ee} + \rho_{gg} = 1$, as the electrons have to be in one of the two states.

$$\rho_{ee} = \frac{1-w}{2} = \frac{\Omega^2}{4(\delta^2 + \frac{\Omega^2}{2} + \frac{\gamma^2}{4})} \quad (6.31)$$

6.4 Derviation of the optical forces

Starting from the quantum mechanical expression of the dipole force

$$F = -e\nabla <\vec{E}(\vec{r}, t) \cdot \vec{r}>$$

and using the expression for the Rabi- frequency $\Omega = \frac{e}{\hbar} E(\vec{r}, t) < e|\vec{r}|g >$ as well as the formula for the expectation value of an operator working on mixed states (see [4]) $< \hat{a} > = Tr(\rho \hat{a})$, we obtain for the force ⁷ [1]:

$$F = \hbar \left(\frac{\partial \Omega}{\partial z} \rho_{ge} + \frac{\partial \Omega^*}{\partial z} \rho_{eg} \right) \quad (6.32)$$

One trick here, in order to distinguish between scattering and dipole force, is to separate the derivative of the Rabi- frequency into its real and imaginary parts [1]:

$$\frac{\partial \Omega}{\partial z} = (q_r + iq_i)\Omega$$

Insertion of this expression into 6.32 leads to:

$$F = \hbar\Omega(q_r\rho_{ge} + iq_i\rho_{ge} + q_r\rho_{eg} - iq_i\rho_{eg}) \quad (6.33)$$

$$= \hbar\Omega(q_r(\rho_{ge} + \rho_{eg}) - iq_i(\rho_{eg} - \rho_{ge})) \quad (6.34)$$

$$= \hbar\Omega(q_r u + q_i v) \quad (6.35)$$

Now one can consider two cases, the first one being a traveling wave incident on the atom, the second the atom situated in a standing wave field. The first one is also equivalent to a moving atom in a standing wave field. However, in the former case, the electromagnetic field can be described as:

$$E(z, t) = \frac{E_0}{2} e^{i(kz - \omega_l t)}$$

which corresponds to a wave, incident from the positive z-direction. This results in $\frac{\partial \Omega}{\partial z} = ik\Omega + eE(z, t) \underbrace{< e|g >}_{=0} = ik\Omega$, therefore $q_r = 0$ and $q_i = k$.

In the latter case, the wavefunction looks like the following:

$$E(z, t) = E_O(z)(e^{i\omega_l t} + e^{-i\omega_l t})$$

⁷Here the induced dipole is considered along the z- direction, furthermore one should bear in mind, that the dipole operator only has non- diagonal elements.

Differentiating results in

$$\begin{aligned}\frac{\partial \Omega}{\partial z} &= e \frac{\partial E_0(z)}{\partial z} \langle e|z|g \rangle + eE(z) \underbrace{\langle e|g \rangle}_{=0} \\ &= e \frac{\partial E_0(z)}{\partial z} \langle e|z|g \rangle = \frac{\partial E_O(z)}{\partial z} \frac{1}{E_0(z)} \Omega\end{aligned}$$

which provides $q_r = \frac{\partial E_O(z)}{\partial z} \frac{1}{E_0(z)}$ and $q_i = 0$.

Both of these cases anticipated the atom to be static, however as the third law of thermodynamics excludes such a situation, an atom placed in a standing wave field (as it will be apparent for both of our trapping set-ups), always experiences a traveling and a standing wave part. Therefore both solutions can be introduced into eq. 6.35, yielding ⁸:

$$F = \frac{e \langle e|z|g \rangle}{2} \left(u \frac{\partial E_0(z)}{\partial z} - v E_0(z) k \right) = F_1 + F_2$$

Using the definition of the Rabi- frequency $\Omega = \frac{e}{\hbar} E(z) \langle e|z|g \rangle$ and the relations for the coherences u, v , given in eq. 6.30, both force terms can be written as:

$$F_1 = \frac{\hbar \delta \omega}{2(\delta^2 + \frac{\Omega^2}{2} + \frac{\gamma^2}{4})} \frac{\partial \Omega}{\partial z} \quad (6.36)$$

$$F_2 = \frac{\hbar k \gamma \omega^2}{4(\delta^2 + \frac{\Omega^2}{2} + \frac{\gamma^2}{4})} \quad (6.37)$$

It turns out, that the first one can be considered as the dipole force, whereas the second one represents the scattering force.

6.4.1 Further examination of the optical forces

Dipole force Looking at $F_1 = \frac{\hbar \delta \omega}{2(\delta^2 + \frac{\Omega^2}{2} + \frac{\gamma^2}{4})} \frac{\partial \Omega}{\partial z}$, one can see, that it vanished by entirely fulfilling the resonance condition $\omega_l = \omega_a$, i.e. $\delta = 0$. However, if the laser is considerably detuned from the natural linewidth of the atomic transition used ($\delta \gg \gamma$) and the detuning is of much higher frequency than the Rabi- oscillations within the atom ($\delta \gg \Omega$), one can simplify the expression above, yielding [1]:

$$F_1 = \frac{\hbar \Omega}{2\delta} \frac{\partial \Omega}{\partial z} = \frac{\partial}{\partial z} \left(\frac{\hbar \Omega^2}{4\delta} \right)$$

The expression in the last bracket exactly equals the one for the light shift (eq: 3.5,3.6) hence:

$$F_{dipole} = \frac{\partial}{\partial z} (\Delta E_{e,g})$$

As discussed already, red- detuned light causes the ground state of the atom to lower in energy- terms for higher intensity fields. This causes the gradient of the energy shift for the

⁸The factor of $\frac{1}{2}$ is introduced here, as we have an induced dipole, see [2].

ground state to be negative, hence the dipole force F_{dipole} points into the direction of lower energy, pushing the atoms to the position of highest laser intensity.

Thus atoms get trapped within a well- type potential, caused by the light shift of the laser radiation. E.g. a standing wave laser beam acts like a trapping device, causing potential wells to occur at its antinodes, in which atoms can get trapped. Also the divergence of a Gaussian beam besides its minimum waist position generates such a potential, since the intensity along its propagation axis decreases as one moves out of the aforementioned position. However trapping is also a question of the well depth and the kinetic energy of the atoms of course. As these wells cannot be made deep enough to trap e.g. Doppler cooled atoms, a sophisticated cooling scheme has to be developed first in order to cool atoms down on a micro K scale, enabling this type of trap to work.

Scattering force In order to explain the second force F_2 (eq. 3.10), we will have a look on the scattering process of photons on atoms in general. Photons scattered on atoms transfer a momentum of $p = \hbar k$.

This is due to stimulated absorption in the first place and subsequent spontaneous emission⁹. As spontaneous emission is random in direction, the average over all directions is equal to 4π , hence the recoil the atom experiences during reradiation averages out over time, resulting in an effective momentum absorption of $\hbar k$. The proportionality constant between the momentum of the absorbed photon and the force on the atom is the excitation rate, which is proportional to the natural linewidth γ as well as the upper state population ρ_{ee} (see 6.31 and the third section of the appendix for further explanations about this density matrix element)¹⁰. Hence the scattering force can be written as [1]:

$$F_{scat} = \hbar k \gamma \rho_{ee}$$

Making use of the equations 6.30 and 6.31, this force can be rewritten as [2]:

$$F_{scat} = \frac{\hbar k \gamma \omega^2}{4(\delta^2 + \frac{\Omega^2}{2} + \frac{\gamma^2}{4})}$$

which is equal to the term F_2 obtained from the quantum- mechanical approach. Therefore we can treat this second term as the scattering force, which can either heat or cool the atoms. As mentioned above, it works via stimulated absorption and subsequent spontaneous emission of photons, therefore it is maximal as the exciting laser beam is resonant with the atom, i.e. $\delta = 0$. Its global maximum can be achieved at transparency, i.e. $\rho_{ee} = 1/2$ or saturated excitation, which gives a max. force of $F_{scat,max} = \hbar k \frac{\gamma}{2}$. Furthermore we can see, that this force is not dependent on the light shift, hence stimulated emission does not contribute to

⁹If reradiation occurs via stimulated emission, the photon's direction of propagation is equal to the one prior absorption, hence no effective scattering has taken place.

¹⁰Here the upper state population has to be used in order to account for saturation of the transition, appearing as $\rho_{ee} \rightarrow 1/2$.

it. As it is velocity dependent this force cools atoms, since energy can be dissipated and the phase-space density of an ensemble of atoms can be changed this way. But besides this, the scattering force is not able to trap atoms alone, as the force does not depend on position, like the dipole force. Therefore an auxiliary device has to be introduced in order to generate the aforementioned dependence, which will be achieved by including a magnetic field, resulting in a magneto-optical trap, whose operating principles can be found in the next section of the appendix.

6.5 Cooling mechanisms and magneto-optical trap

6.5.1 Doppler cooling

In order to cool an atom, we must have stimulated absorption and subsequent spontaneous emission. Therefore incident light must be close to the atomic resonance frequency ω_a , i.e. for recognisable effects within the natural linewidth γ . If atoms are not cold yet, their motion towards/opposed to the incident light causes a Doppler-shift of the light's frequency, resulting in $\omega'_l = \omega_l - \vec{k} \cdot \vec{V}$ ¹¹, thus the Doppler-shifted frequency has to fulfill the above stated resonance condition. As we desire to cool atoms down, the absorption of photon-momentum has to be opposite to their direction of motion, whereby the scalar-product $-\vec{k} \cdot \vec{V}$ becomes positive and the cooling laser beam must be red-detuned with respect to the atomic transition, i.e. $\delta < 0$. Cooling relying on this Doppler shift is referred to as Doppler cooling.

While atoms absorb photons in the aforementioned way, their velocities change, causing a smaller Doppler shift and therefore loss of resonance.

This problem can be cured by applying a constant, inhomogeneous magnetic field B , forcing a Zeeman shift in the atomic energy levels. If the ground and excited state are chosen to have different Zeeman splittings, the resonance condition can be maintained.

As atoms in a thermal ensemble do not move in one direction only, applying counter-propagating laser beams in all three dimensions can take care of random directions of motion. Those laser beams generate a redirecting force towards $\vec{V} = 0$ velocity of the atoms, which can be seen in fig: 6.1.

According to the scattering force, the detuning for both counter-propagating laser beams is $\delta_{\mp} = \omega_l \mp \vec{k} \cdot \vec{V}$ ¹². This results in a force in the atoms of [2]:

$$F_{total} = F_{scat+}(\omega_l - |k| \cdot |V| - \omega_a) - F_{scat-}(\omega_l + |k| \cdot |V| - \omega_a)$$

A Taylor expansion of the $F_{scat\mp}$ terms simplifies this expression to¹³:

¹¹ \vec{V} is the velocity of the atom.

¹² – refers here to opposite directions of atomic motion and light incidence, whereas + symbolises equal directions.

¹³ As the deviation in frequency terms due to the Doppler shift is rather small compared to the absolute frequencies ω_l and ω_a , this approximation is valid

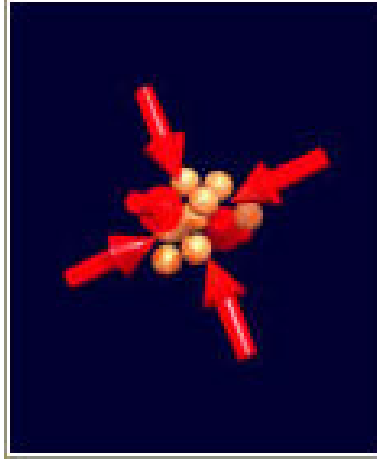


Figure 6.1: Scheme for an optical molasses; the force laid onto the cloud of atoms by the laser radiation is illustrated as red arrows; source: [8]

$$F_{total} = F_{scat}(\omega_l - \omega_a) + |k| \cdot |V| \frac{\partial F}{\partial \omega_l} - F_{scat}(\omega_l - \omega_a) + |k| \cdot |V| \frac{\partial F}{\partial \omega_l} = - \underbrace{2|k| \frac{\partial F}{\partial \omega_l}}_{:=\alpha} |V|$$

One now clearly sees the last expression representing a damping term $F_{total} = -\alpha|V|$, which is linearly velocity dependent. This force cools atoms towards 0 velocity, independent of their initial direction of motion, since it consists of 2 counter- propagating beams in each dimension. An apparatus like this is called an optical molasses. But again, as the force is not position dependent, this set- up is not able to trap atoms.

6.5.2 Magneto- optical trap (MOT)

In order to maintain the resonance throughout a useful velocity range, the molasses is now placed within an inhomogeneous quadrupole- magnetic field. For simplicity, we will focus on the z- dim. only, requiring a field $B = Az$ ([1]), which is generated by coils conducting current of opposite direction, as depicted in fig. 6.3.

In our experiment, we will use Rb^{87} , whose energy level scheme can be seen in fig. 6.2. As the transition used for cooling, we will take the hyperfine splitted states $|F = 2, m_F = 2 > \rightarrow |F = 3, m_F = 3 >$, having a resonance wavelength of $\lambda = 780nm$. Therefore the upper state has three degenerated states ($m_F = \pm 1, 0$), which will be split in B according to their magnetic quantum number, i.e. $m_F = 1$ raised, $m_F = -1$ lowered and $m_F = 0$ unchanged in energy terms along pos. values of z. This behaviour is visualised in fig: 6.4.

If there are counter- propagating, red- detuned laser beams applied along the z- axis, having σ^- polarisation as incident from pos. z values and σ^+ polarisation by neg. z incidence, the Doppler- shifted laser frequency will be resonant with the Zeeman- shifted atomic resonance

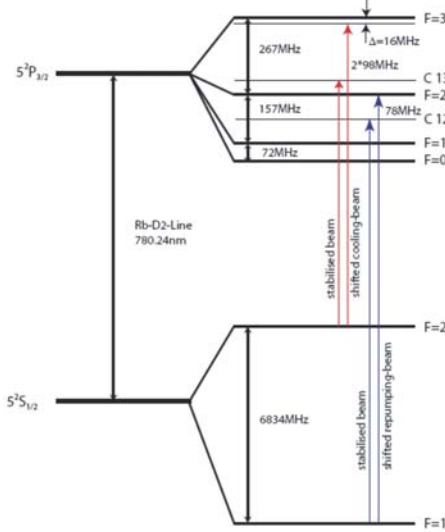


Figure 6.2: Level- scheme for Rb^{87} ; the red arrows correspond to the cooling and trapping beam, the blue ones to the re- pumping laser. Both are stabilised to a frequency slightly lower than the actual transition frequency, whereas the additional off-set required for resonance is generated by acusto- optical modulators.

frequency, whereby absorption and hence cooling can take place (see fig. 6.4). The variation in the Zeeman splitting also assures, that all atoms with a velocity below a critical value, will fulfill the resonance condition from a certain point along the z- axis onwards.

The detuning now comprised another term due to the Zeeman effect ¹⁴: $\delta_{\mp} = \omega_l - \vec{k} \cdot \vec{V} - \omega_a - \beta z$, which results in a molasses force of ([2]):

$$F_{MOT} = F_{scat+}^{\sigma+}(\omega_l - |k| \cdot |V| - \omega_a - \beta z) - F_{scat-}^{\sigma-}(\omega_l + |k| \cdot |V| - \omega_a + \beta z)$$

which results, after a Taylor expansion, in the expression:

$$F_{MOT} = -\alpha|V| + 2 \frac{\partial F}{\partial \omega_a} \beta z$$

From this we see on the already encountered velocity dependant term $F_{cool} \sim \alpha|V|$ and a new, position dependent term $F_{trap} \sim \beta z$. Therefore we end up with a system, that is also able to trap atoms around its central position at $z = 0$. As atoms are displaced from this position, although they do not have a velocity, they experience a force, pushing them back to the centre of the trap. A typical device working in all three dimensions can bee seen in fig: 6.3.

Although the previous description of the MOT raises the expectation of being able to cool the atoms to a temperature $T = 0 K$, this clearly violates thermodynamics. An effect, which has been totally neglected so far is the randomness in direction of the spont. emission process. Notwithstanding it canceling out on time- average, it leads to a recoil of the atoms and therefore

¹⁴ $\beta = \frac{(g_e m_F, e - g_g m_F, g) \mu_B A}{2\hbar}$, see [3]

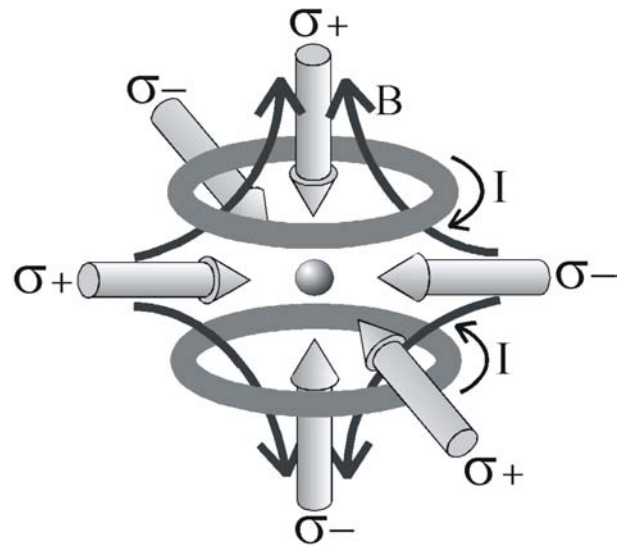


Figure 6.3: Typical setup for a magneto-optical trap. The laser beams are σ^+ , or respectively σ^- polarised. The inhomogeneous magnetic field is illustrated as black arrows; source: [27].

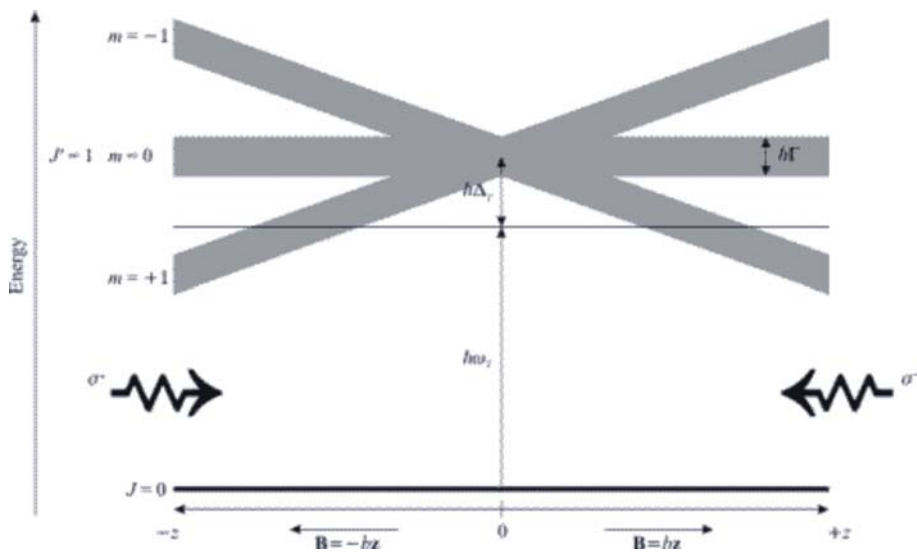


Figure 6.4: Scheme of Zeeman-shifted excited state levels with appropriately detuned and polarised laser light, incident from either side along one dimension of MOT; source: [28].

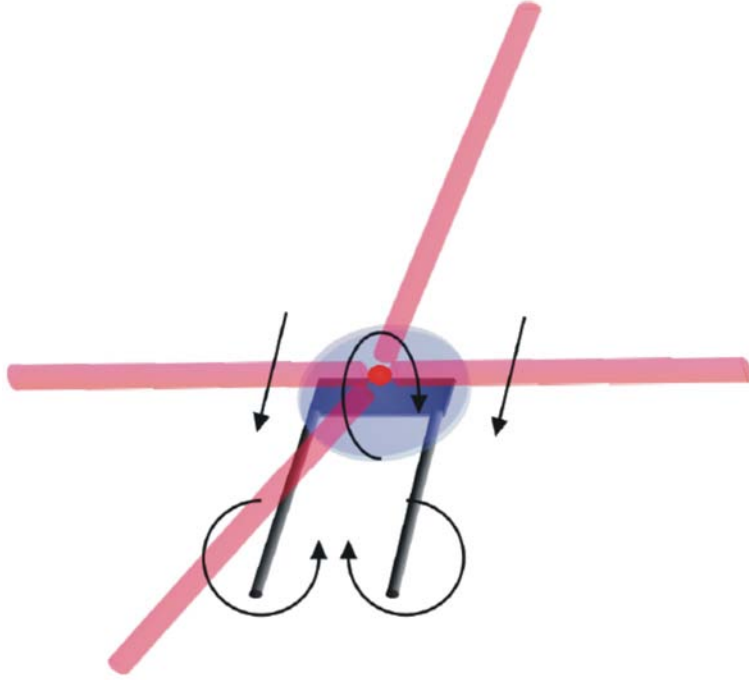


Figure 6.5: Scheme of beam alignment for our MOT setup. Beams are reflected back into themselves, σ^+ polarised in the one, σ^- polarised in the other direction. The vertical beam is reflected by the dielectric mirror on the bottom of the trap. Magnetic field directions are indicated by black arrows.

to a movement corresponding to a random walk. Since the Doppler- cooling relies on the spont. emission effect, atoms cannot be cooled to temperatures colder than given by the kinetic energy within this random walk process. This relates to a temperature of (see ref. [2] or [1] for a derivation)

$$T = \frac{\hbar\gamma}{2k_B}$$

which is normally within the regime of several $100 \mu K$. However within a standing wave MOT, temperatures of several μK can been reached, so far lower than via Doppler cooling alone. This is caused by polarisation gradient effects, explained in the next paragraph.

In our particular set-up, we use two laser beams, for generating the MOT, both incident on a vacuum chamber with a mirror covered bottom. One orientated parallel to the mirror, entering the MOT from one side with σ^+ polarisation and getting back- reflected into itself by a mirror on the other side, therefore being σ^- polarised, resulting in one of the molasses beams. The second beam is again σ^+ polarised and incident under an angle of approximately $\vartheta = 50 \text{ deg}$ to the mirror surface, as visualised in fig. 6.5. It gets reflected from the mirror with a phase shift of π , resulting in σ^- polarisation under an angle of $\vartheta = 50 \text{ deg}$ to the opposite side of its incidence.

Subsequently the beam gets reflected again by a mirror, causing it to take approximately

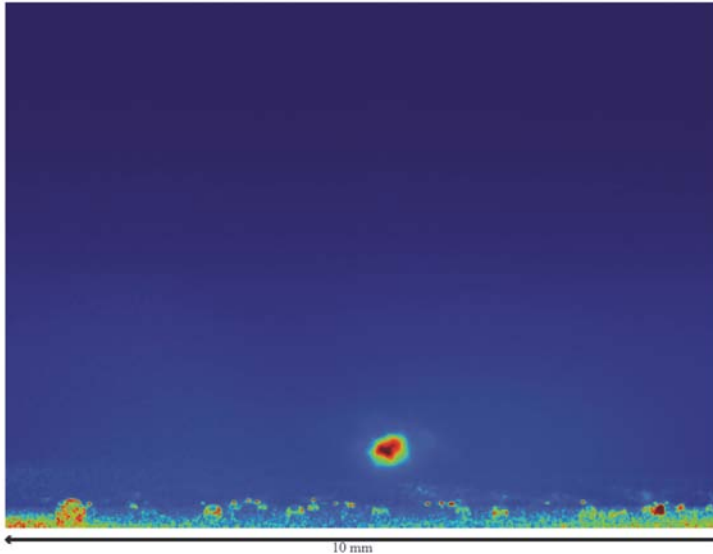


Figure 6.6: Image of cold atomic cloud in our MOT, cooled down to the Doppler limit and approximately $50 \mu m$ in diameter. Picture taken in the infra-red via a CCD camera.

the same beam path in the reverse direction with a polarisation of opposite handedness. As both beams have a waist in the mm- regime, this causes a small volume, close to the mirror surface, to fulfill the conditions of having 3 standing- wave laser beams, generating cooling and trapping forces in all 3 dimensions. Therefore we can achieve trapping of atoms close to the mirror surface, with a distance of approximately $100 \mu m$ in between, while the trapped atomic cloud has a diameter of roughly $50 \mu m$ the same dimension. The fluorescence of a Rb ensemble in the IR, captured by a CCD camera, can be seen in fig. 6.6

6.5.3 Polarisation gradient cooling

For loading atoms into the dipole trap, atoms have to be colder than achieved by Doppler cooling alone. A further step to lower temperatures is comprised by polarisation gradient cooling, an effect relating to the hyperfine structure of atoms and a standing wave field of perpendicular polarisation¹⁵, as in our case achieved by $\sigma^+ - \sigma^-$ polarised light in the optical molasses. Unfortunately the $\sigma^+ - \sigma^-$ case is the harder one to grasp, so the reader might be pointed out to the references [2], [1], [8] and [9] in order to see the easier case of linear \perp linear polarisation gradient cooling (also referred to as Sysiphus cooling) in the first place. However the two counter- propagating, circular polarised beams overlap and generate a standing wave with rotating linear polarisation, as depicted in fig. 6.7.

In general, an atom in such a light field would adjust the axis of its dipole moment parallel to the direction of polarisation, as this minimises its energy [8], which corresponds to the lowest light shifted state. Considering a resting atom, this will be the $m_F = 0$ state for linear light-polarisation, see fig. 6.8.

¹⁵ Alternatively also a standing wave of a single polarisation in combination with a magnetic field can be used.

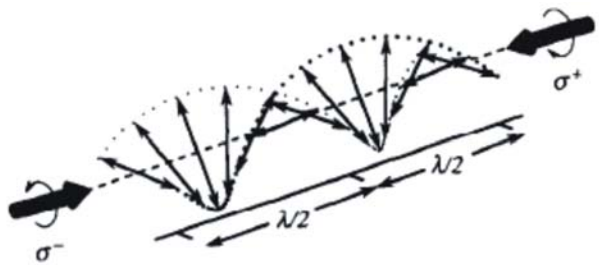


Figure 6.7: Superposition of a σ^+ - and a σ^- - polarised wave, opposing each other, which leads to a spatially rotating, linear polarised light field; source [8].

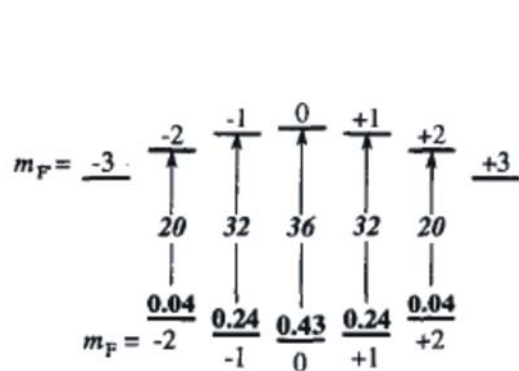


Figure 6.8: Energy level scheme for non-moving atoms in standing wave of rotating linear polarisation; source: [8]

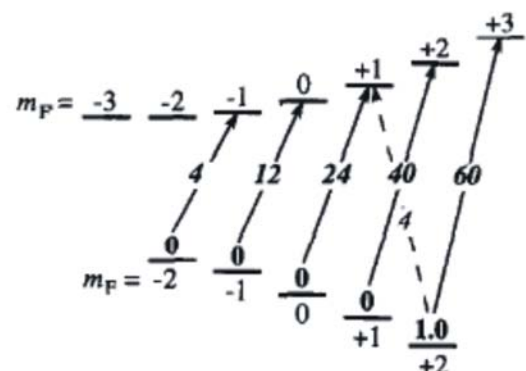


Figure 6.9: Redistribution of energy levels and their occupation for atoms moving opposite to the σ^+ - polarised beam incidence; source [8].

Having further only π - excitations (i.e. $\Delta m_F = 0$), optical excitation cycles tend to populate the $m_F = 0$ substate. As the atoms still have kinetic energy left, they will move along the standing waves, hence they see the polarisation direction changing, i.e. e.g. if atoms move along the σ^+ beam, they see the linear polarisation changing clockwise. The dipole moment of each atom is therefore not parallel to the light polarisation anymore and follows it, although lacking behind the appropriate orientation. This deviation from a steady state situation causes, according to [10], a build up of population in the $m_F = +1$ state compared to the $m_F = -1$ as atoms are traveling towards σ^+ light and vice versa for σ^- (see fig: 6.9). Such a population redistribution also causes increased scattering of the opposing light, in the upper example σ^+ (see [8]), resulting in an effective force opposing the movement of the atoms, dissipating kinetic energy and therefore cooling. As this effect crucially depends on the energy splitting between the magnetic hyperfine levels and their light shifts, no distorting magnetic field must be apparent. Therefore the magnetic field in the MOT has to be switched off¹⁶ in order to achieve this process. But as polarisation gradient cooling does not confine the atomic cloud, this sort of cooling can only be maintained for a couple of micro seconds, before the atoms have to be either loaded back into the MOT or onwards into the dipole trap. The temperatures achieved with this sort of cooling can be calculated according to (see [8]):

$$k_B T = \frac{\hbar \gamma^2 I}{2|\delta|I_{sat}} \left(\frac{29}{300} + \frac{254}{\frac{300\delta^2}{\gamma^2} + 75} \right) \quad (6.38)$$

However indicated by this equation, the limiting temperature with this mechanism is given by recoil limit, which is the kinetic energy obtained by an atom, while absorbing/ emitting a single photon, hence [1]:

$$T_{recoil} = \frac{\hbar^2 k^2}{k_B M}$$

which is typically in the micro Kelvin regime, and for our setup supposed to be around $T_{recoil} \approx 0,36 \mu K$.

6.6 Loading of optical dipole trap

This section will deal shortly with the dependencies of the loading process for atoms from a MOT into an optical dipole trap. Although the influence of various trap parameters will be given, a proper explanation of them will be left out and the reader might be pointed out to references [12], [13] and [14]. So the following text only tends to provide some hints of what can be done, if the simple switching off of the MOT and switching on of the dipole trap does not succeed in sufficient loading rates. Considering the factors throwing atoms out of the traps during loading, one will end up finding heating effects to be responsible. In particular heating effects, like spontaneous scattering of dipole trap light (due to absorption of the latter),

¹⁶Reducing it basically to an optical molasses.

intensity fluctuations in the dipole trap's intensity as well as stability and proper alignment of the beam path are contributing. Even more severe collision effects between atoms in the trap, causing photoassociation¹⁷, spin exchange ground state hyperfine changing collisions¹⁸, radiative escape and collisions with background atoms provide loss mechanisms; for a further description of these effects, see [1], [12] and [8]. The first sort of losses are one body decays and hence proportional to the atom number, loaded in the dipole trap, N , whereas the second one (with exception of the background collisions) are two- body effects, whence proportional to $N(N - 1)$. With a loading rate R , a one- body loss rate γ and a two- body collision rate β , the loading rate for the dipole trap from the MOT can be written as [14]:

$$\frac{dN}{dt} = R - \gamma A - \beta N(N - 1) \quad (6.39)$$

The effective amount of atoms loaded strongly depends on the trapping parameters of both traps in the following way (see also [12]):

- The lower the re-pump intensity of the MOT I_r and the closer to resonance of the re-pumping transition ($5S(F = 1) \rightarrow 5P(F = 2)$), the lower β and the higher the loading rate R .
- The higher the MOT's cooling and trapping beam intensity I_{MOT} , the higher the collisional loss rate β . However for larger values of I_{MOT} (typically: $I_{MOT} \gtrsim 4 \frac{mW}{cm^2}$ [12]), β saturates.
- For large detunings in the magnetic field gradient, the MOT loss is strongly increased, resulting in a shorter loading time, hence a smaller N .
- The centre for the dipole trap's potential well is best positioned slightly longitudinally off centre with respect to the atomic cloud position in the MOT. This displacement for optimum loading increases, the deeper the potential pit of the dipole trap is.
- The deeper the dipole traps potential, the higher the loading rate R and the lower the collisional losses β .
- For larger beam waists of the trapping beam in the dipole trap, more atoms can be loaded into a single state within this trap.
- Deviations of the dipole trap's beam polarisation from linear result in a lower number of atoms loaded into the trap.

An explanation for all of these effects together with appropriate graphs, underlining the above stated trends, can be found in [12]. So in the case of the loading rate into the dipole trap being to small or to high, an optimisation according to the above stated behaviour can be

¹⁷Collision of one unperturbed and one excited atom with subsequent molecule formation and loss.

¹⁸Collisions causing transitions of the atoms from one ground state, which is trapped via the light- shift, into an untrapped one.

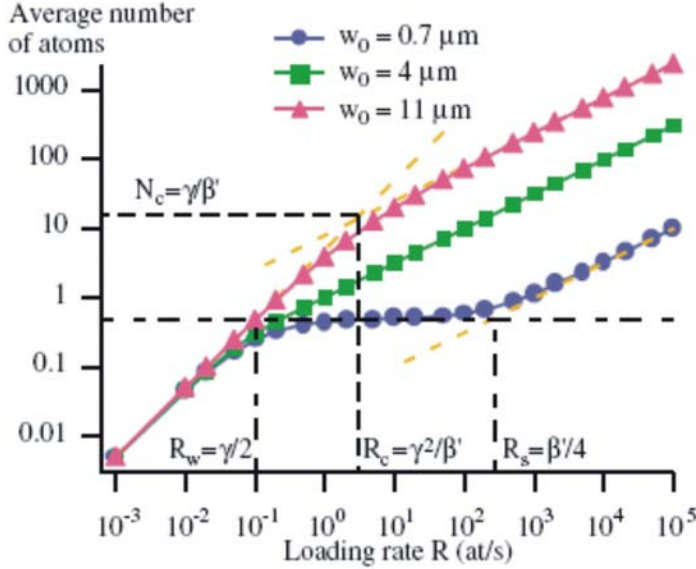


Figure 6.10: Average number of loaded atoms into a dipole trap bound state as a function of the loading rate and beam waist; from [14].

attempted. However as we try to trap only a single atom in the focus of the trap, one can also try to get out of the collisional blockade mechanism ([13], [14]): This effect basically shows up for quite deep dipole trap potentials, hence high laser intensities, and very narrow beam waists of $w_0 \lesssim 4 \mu\text{m}$ ([14]). It is based on the collisional loss mechanism being much superior than the one- body loss mechanisms. In general this happens, as the loaded number of atoms N is much larger than a critical atom number [14] $N_c = \frac{\gamma}{\beta}$, which is again proportional to a critical loading rate of $R_c = \frac{\gamma^2}{\beta}$. However for tight, intense dipole trap foci, the critical atom number gets into the region of $N_c \approx 1$, causing a collisional loss mechanism to appear as soon as more than a single atom is loaded into one trap state¹⁹. With a second atom loaded into the trap, it turns out ([13], [14]), that the collision between the two results in both being thrown out of the trap, hence the number of trapped atoms to be either 0 or 1. However this effect appears only for a certain loading rate range, as visible from fig. 6.10, since for quite small loading rates the average atomic number is small enough to provide neglectable probabilities of atom collisions. For higher loading rates however a Poissonian distribution of the loaded atom number appears, since the loss rate is simply succeeded by the loading rate.

In the collisional blockade regime, there is only one or none atom within a bound state in the dipole trap, loading a single atom appears to be easy in the first place. However the disadvantages are on the one hand the required activity of the MOT, since it has to be running to obtain this blockade effect. On the other hand there is a 50 percent probability of the dipole trap to remain empty completely during loading, which makes this way of atom transfer quite inefficient. An advantage can be seen in the relative long lifetimes of atoms, once loaded into

¹⁹One has to bear in mind here, that the trapping potential is equivalent to a quantum well, hence single bound states are generated within it.

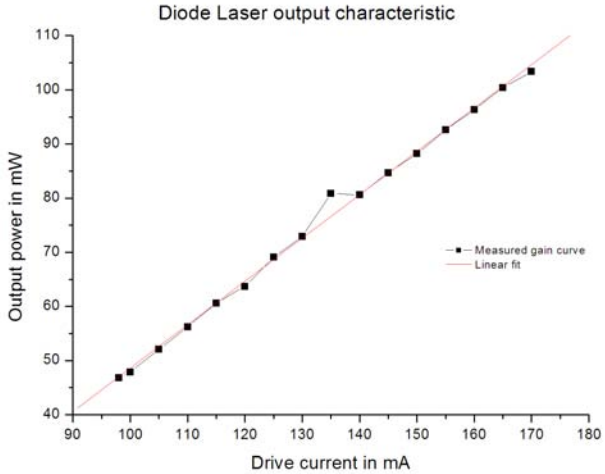


Figure 6.11: Power characteristic of the testing laser [17] showing the linear gain regime; the linear fit was done by using *Origin*[©].

the dipole trap, of a few seconds ([13]) in the case of low loading rates R . Furthermore one has to bare in mind here, that the collisional blockade mechanism works independently for each bound state within the trap's potential well; hence one could end up, for a sufficiently deep potential, with a many atoms loaded into the trap at its focus, although having only a single atoms for each state. Nevertheless this regime requires deep trapping potentials for the dipole trap, i.e. high light intensities; however we are not sure yet, whether the power from our laser, reflected by the active area of the DMD will be enough in order to reach this regime at all. Therefore the above discussion might seem to be somehow artificial, but it should just show the reader a possibility of achieving single atom trapping in a dipole trap.

6.7 Diode laser power characteristic

Before proceeding with the actual experiments, we first of all measured the power characteristic of the testing laser in our operating range, which can be seen in fig: 6.11.

We clearly see, that we are within the linear gain regime and the appropriate power characteristic can be fitted to ²⁰:

$$P = (0,80052 \pm 0,01387) \frac{mW}{mA} \cdot I - (31,44428 \pm 1,86716)mW \quad (6.40)$$

In our setups, we will drive the diode laser for the measuring runs with $I = 98\text{ mA}$, resulting in an output power of $P = 43,3\text{ mW}$.

²⁰Linear fit by *Origin*[©]

6.8 Additional plots for second experimental setup

6.8.1 Moving $50\mu m$ aperture in the transverse plane

Measured maximum and minimum beam waists

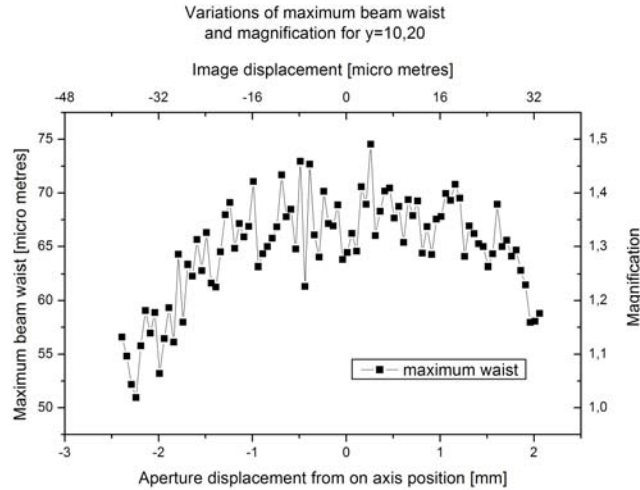


Figure 6.12: Variations of maximum beam waist along x- direction for $0,45\text{ mm}$ relative y displacement.

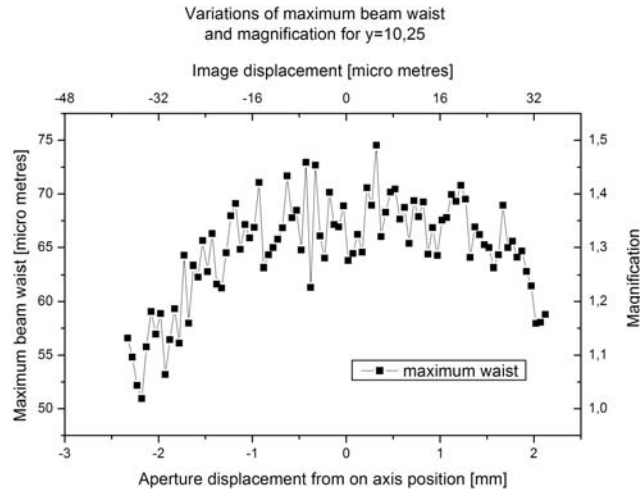


Figure 6.13: Variations of maximum beam waist along x- direction for $0,4\text{ mm}$ relative y displacement.

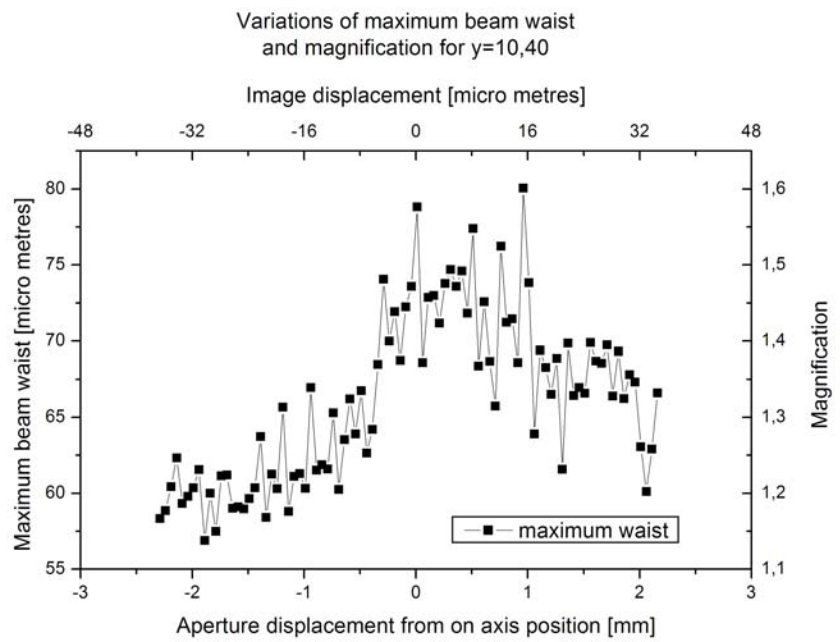


Figure 6.14: Variations of maximum beam waist along x- direction for $-0,25\text{ mm}$ relative y displacement.

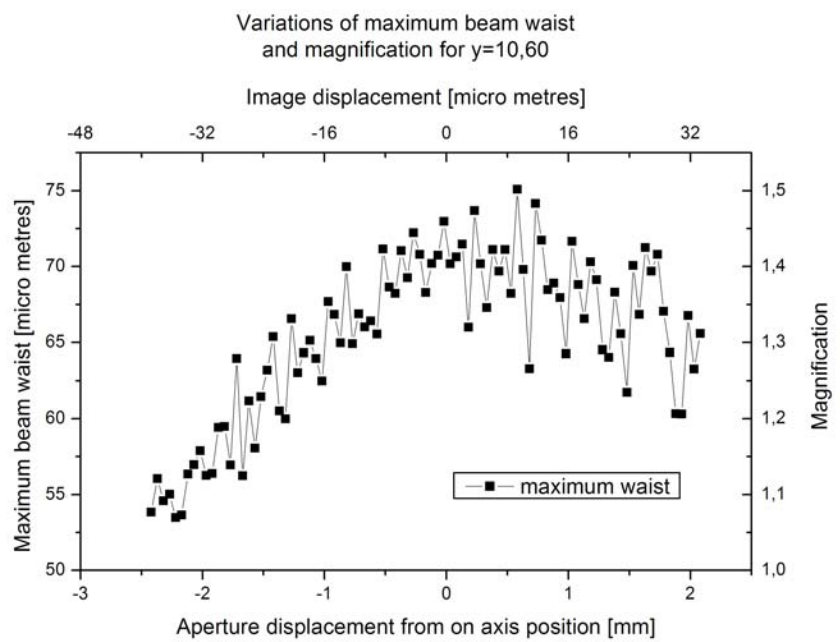


Figure 6.15: Variations of maximum beam waist along x- direction for $-0,05\text{ mm}$ relative y displacement.

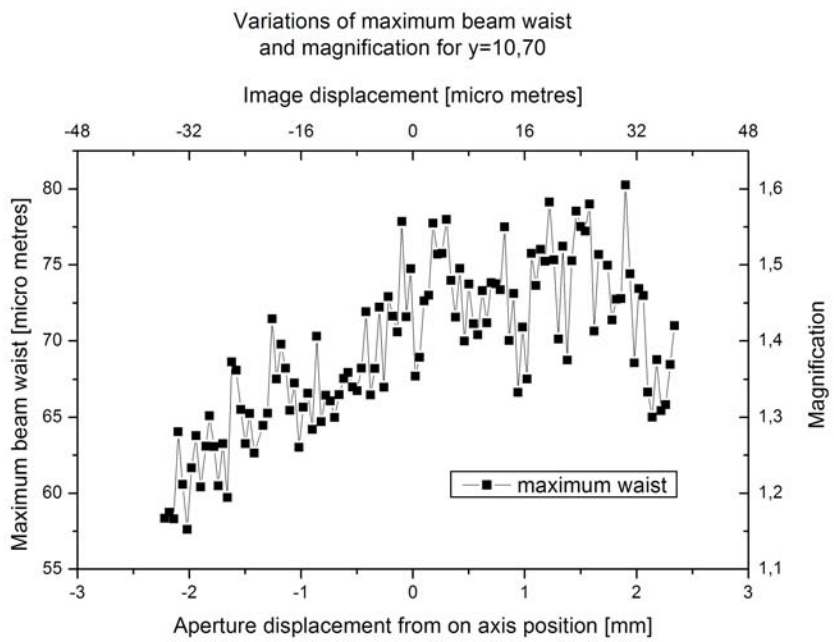


Figure 6.16: Variations of maximum beam waist along x- direction for 0,05 mm relative y displacement.

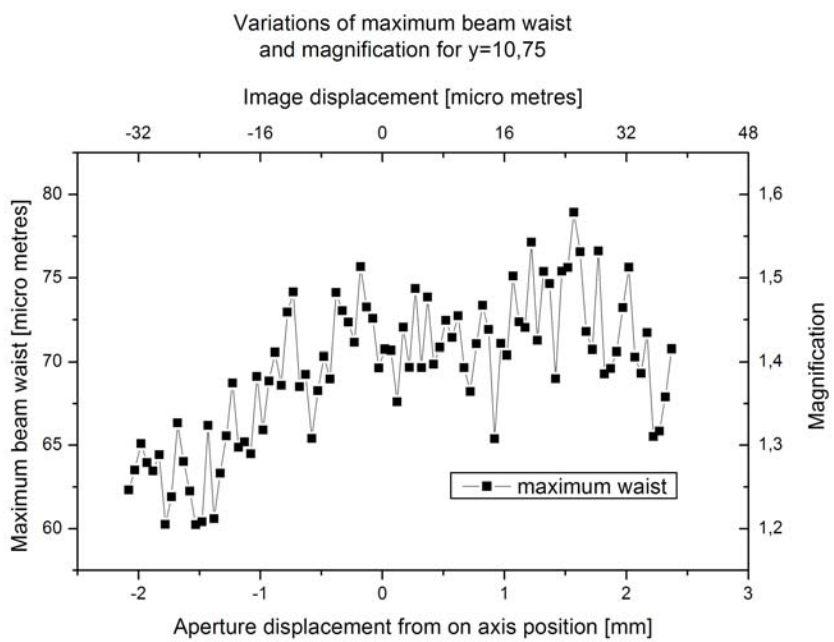


Figure 6.17: Variations of maximum beam waist along x- direction for 0,1 mm relative y displacement.

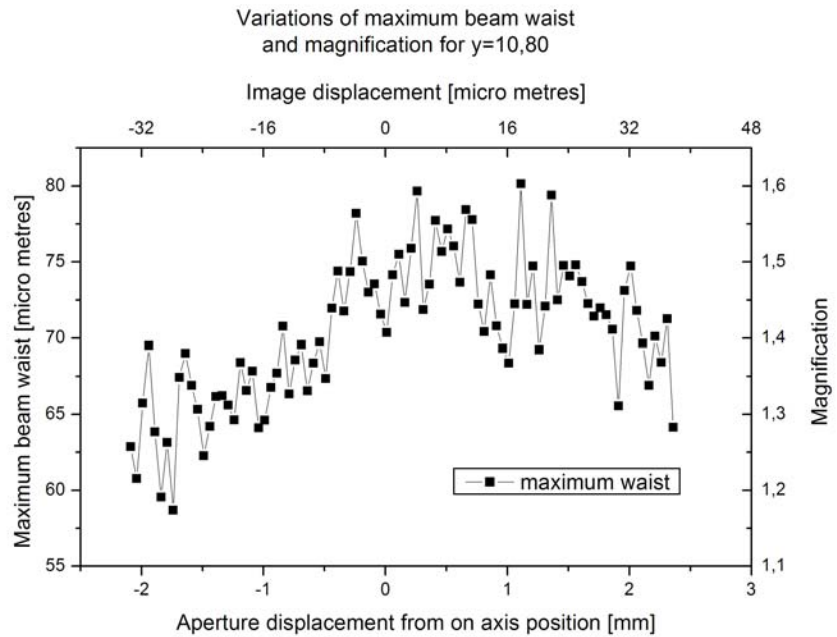


Figure 6.18: Variations of maximum beam waist along x- direction for 0,15 mm relative y displacement.

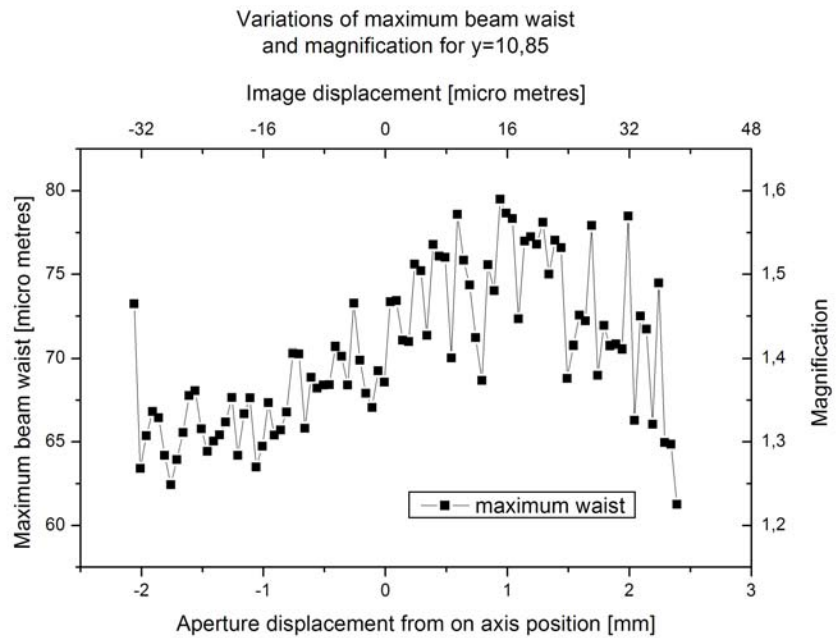


Figure 6.19: Variations of maximum beam waist along x- direction for 0,2 mm relative y displacement. Values for $x = -2,06\text{ mm}$ and $x = 2,39\text{ mm}$ were treated as spikes and hence neglected for further analysis.

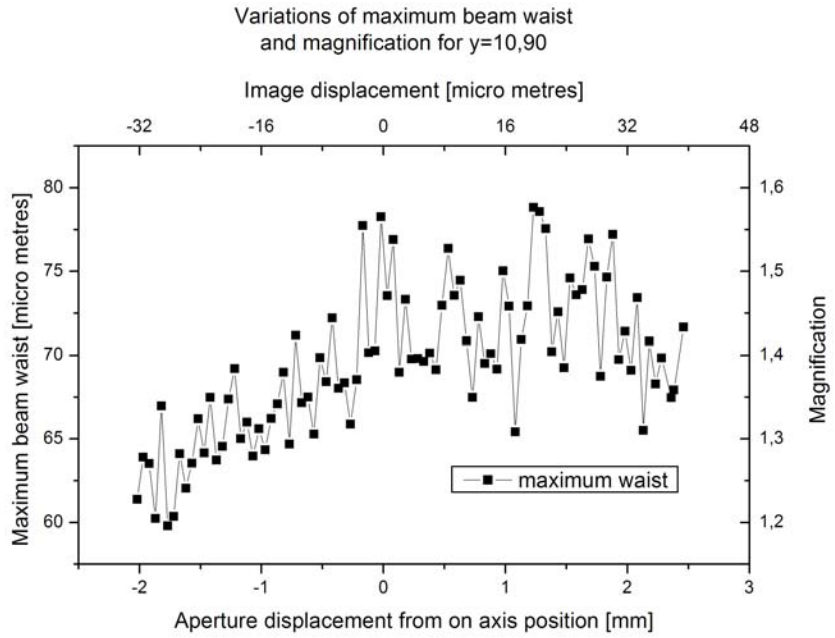


Figure 6.20: Variations of maximum beam waist along x- direction for 0,25 mm relative y displacement.

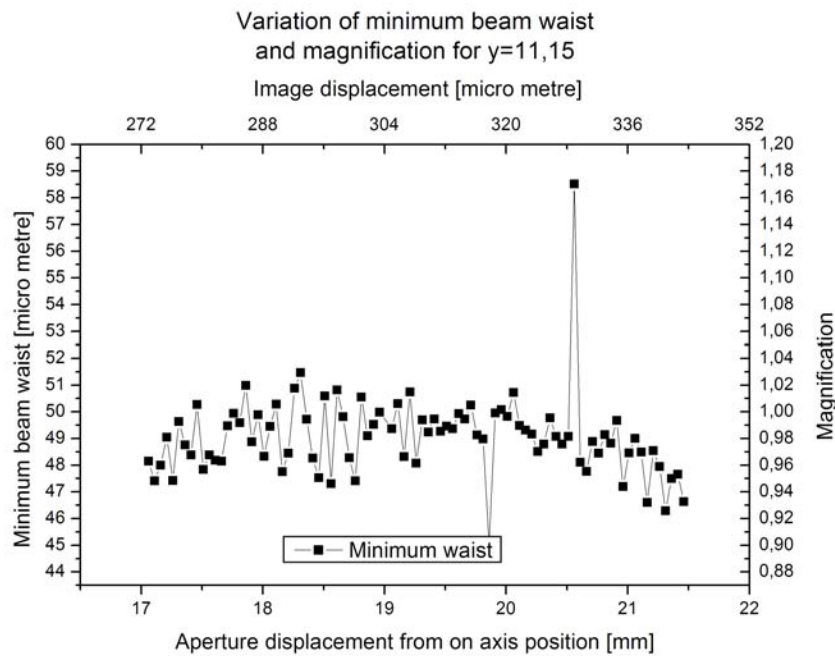


Figure 6.21: Variations of maximum beam waist along x- direction for 0,5 mm relative y displacement. Values for $x = -1,04 \text{ mm}$ and $x = -0,99 \text{ mm}$ were treated as spikes and hence neglected for further analysis.

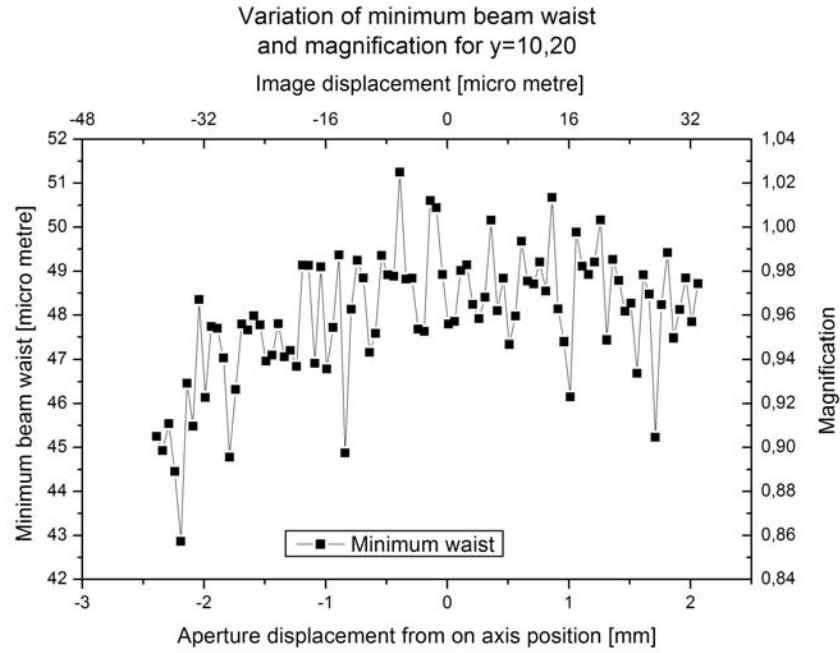


Figure 6.22: Variations of minimum beam waist along x- direction for 0,45 mm relative y displacement. The value for $x = -2,19 \mu m$ was treated as a spike and hence ignored for further analysis.

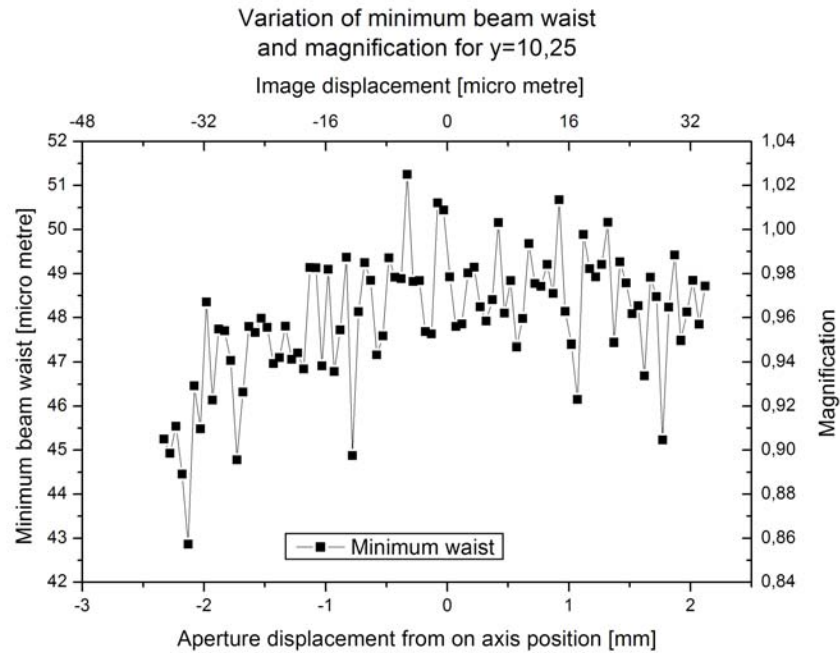


Figure 6.23: Variations of minimum beam waist along x- direction for 0,4 mm relative y displacement.

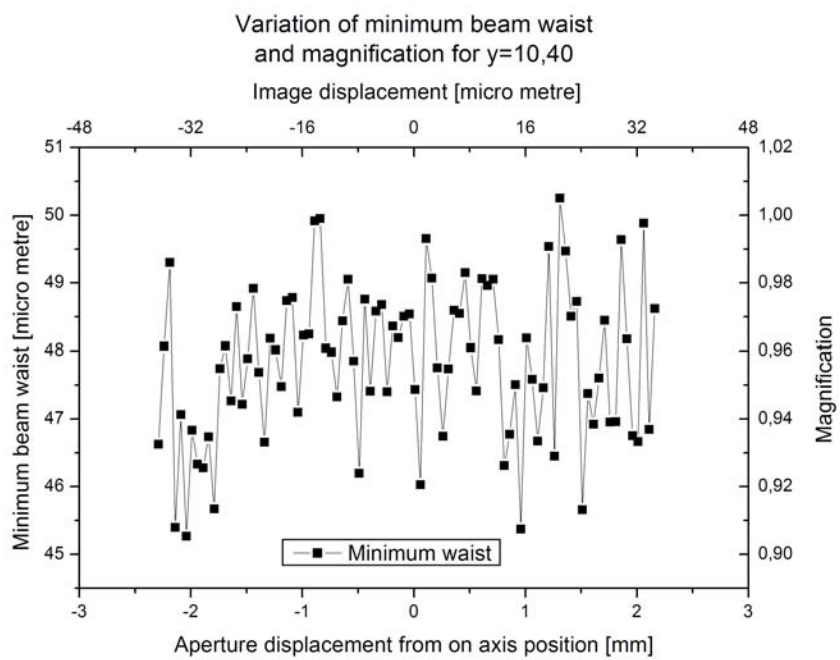


Figure 6.24: Variations of minimum beam waist along x- direction for $-0,25\text{ mm}$ relative y displacement.

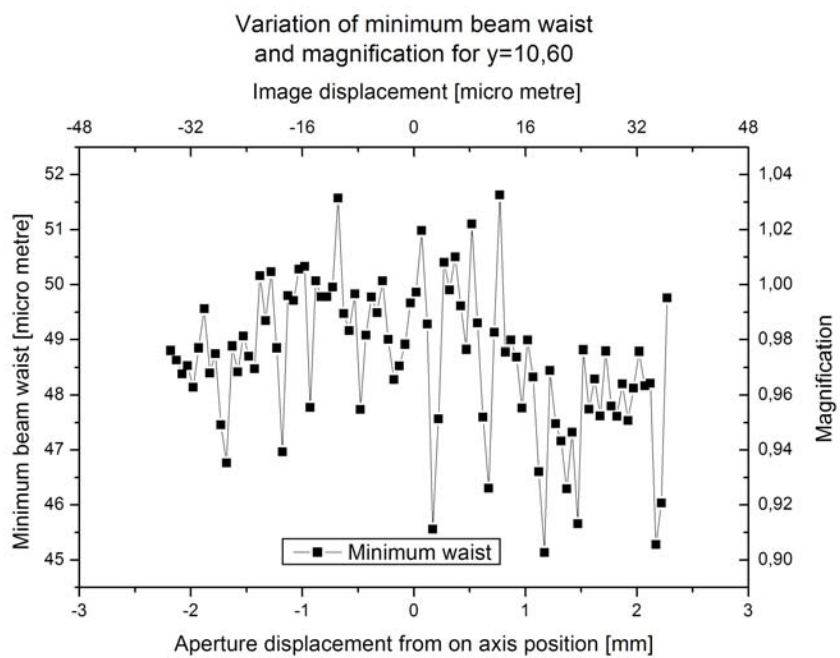


Figure 6.25: Variations of minimum beam waist along x- direction for $-0,05\text{ mm}$ relative y displacement.

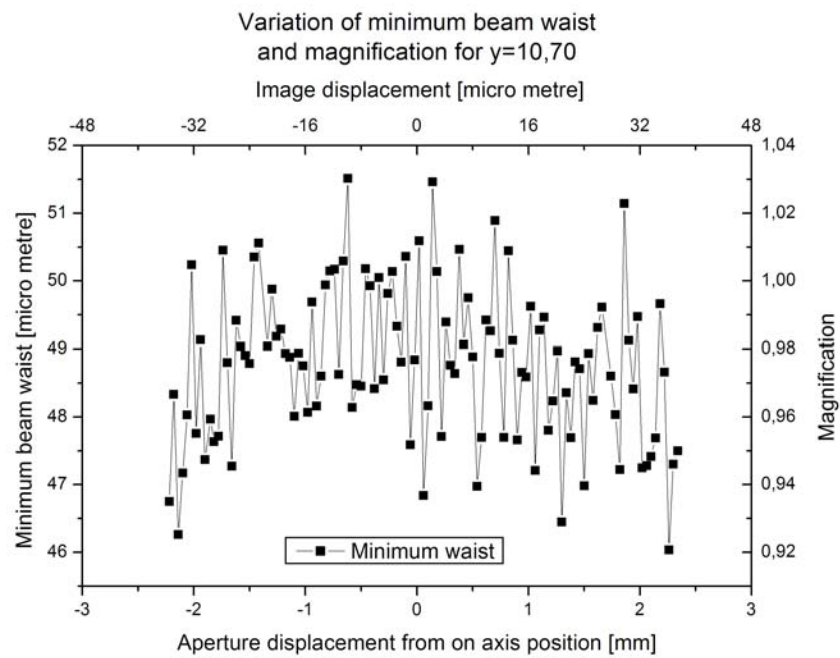


Figure 6.26: Variations of minimum beam waist along x- direction for 0,05 mm relative y displacement.

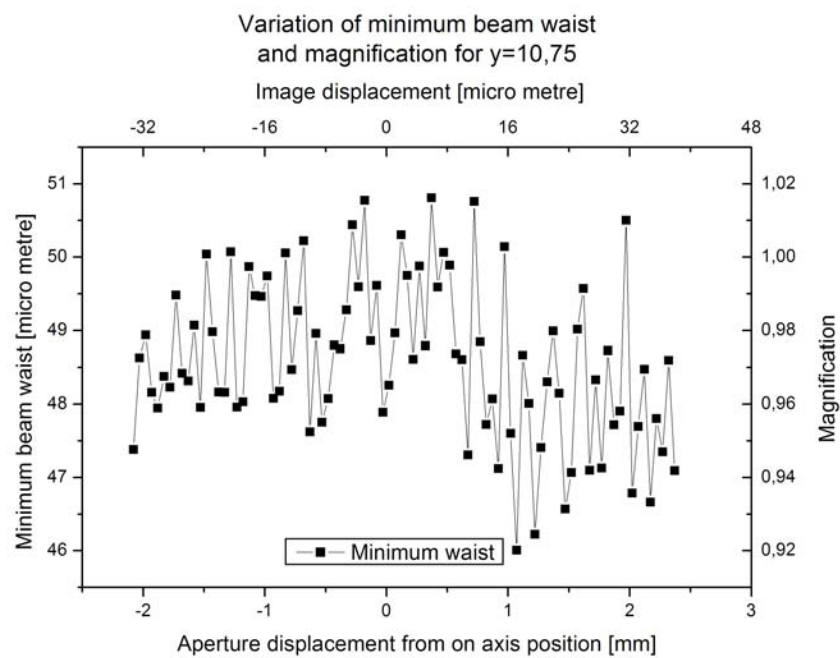


Figure 6.27: Variations of minimum beam waist along x- direction for 0,1 mm relative y displacement.

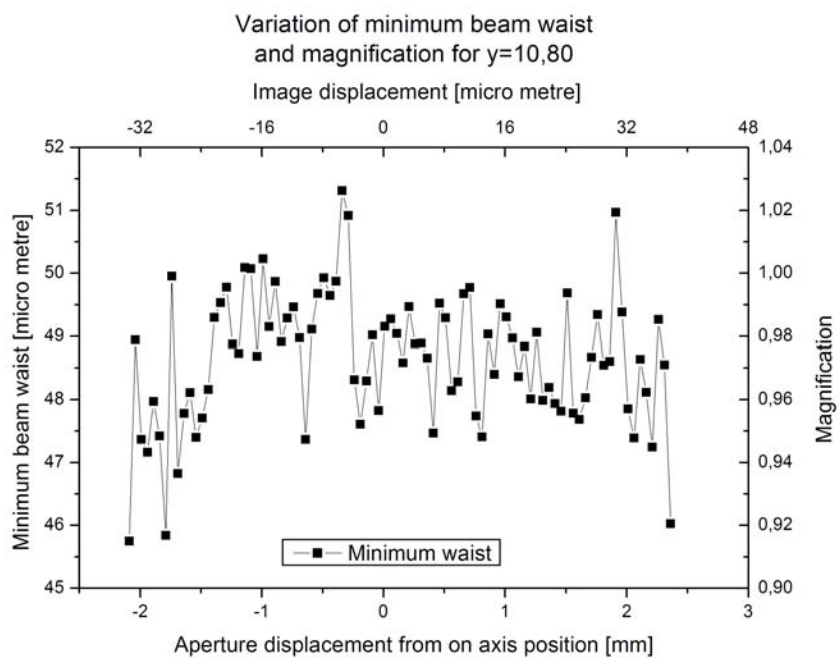


Figure 6.28: Variations of minimum beam waist along x- direction for 0,15 mm relative y displacement.

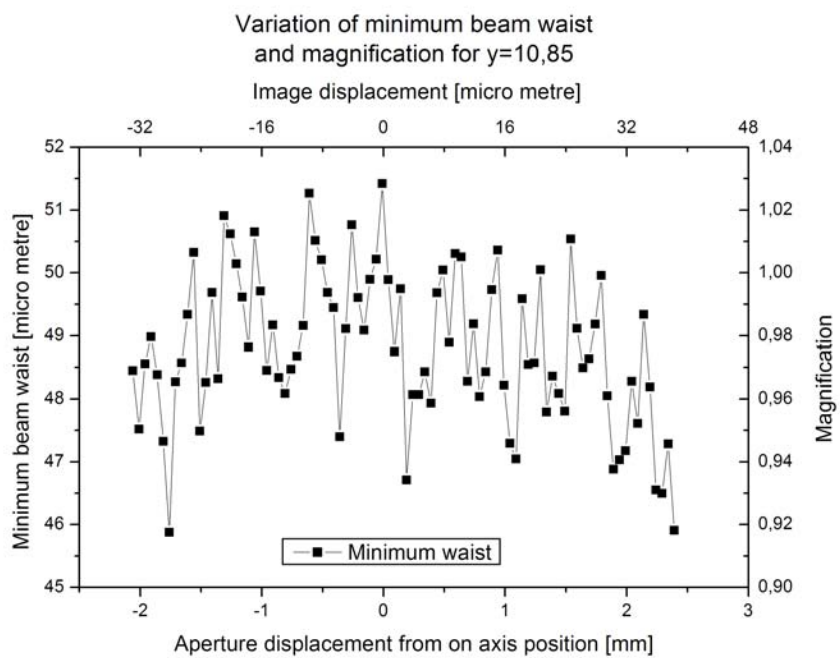


Figure 6.29: Variations of minimum beam waist along x- direction for 0,2 mm relative y displacement.

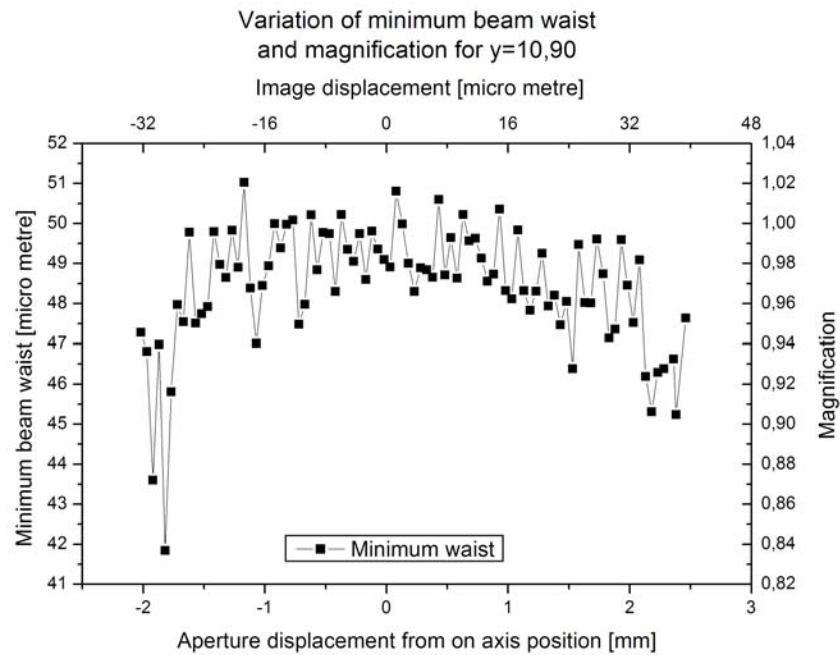


Figure 6.30: Variations of minimum beam waist along x- direction for 0,25 mm relative y displacement. Value for $x = -1,92 \mu m$, $x = -1,82 \mu m$ and $x = -1,77 \mu m$ were treated as spikes and hence ignored for further analysis.

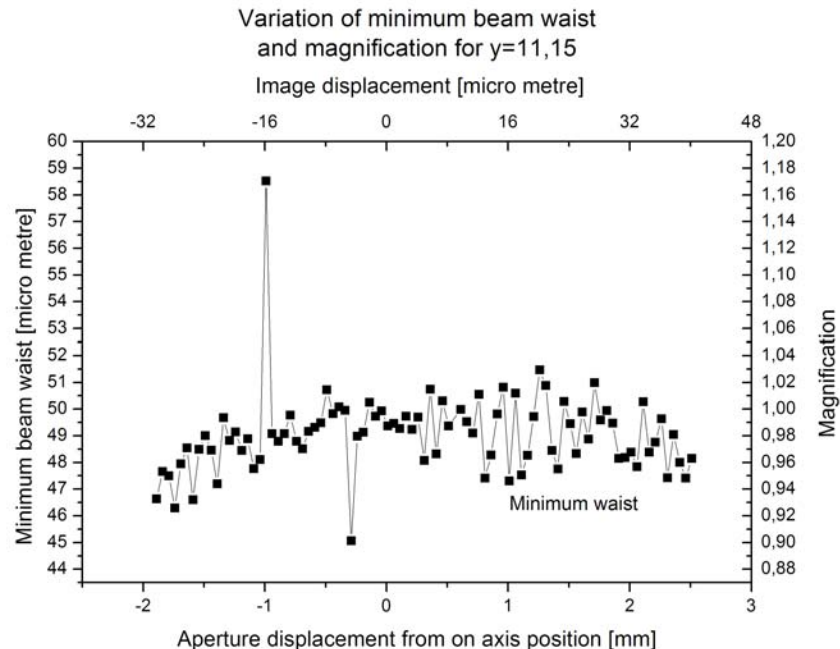


Figure 6.31: Variations of minimum beam waist along x- direction for 0,5 mm relative y displacement. Values for $x = -0,29 \mu m$ and $x = -0,99 \mu m$ were treated as spikes and hence ignored for further analysis.

6.8.2 Displacing aspheric lens along optical axis and restoring focus by collimator movement

Minimum and maximum beam waists

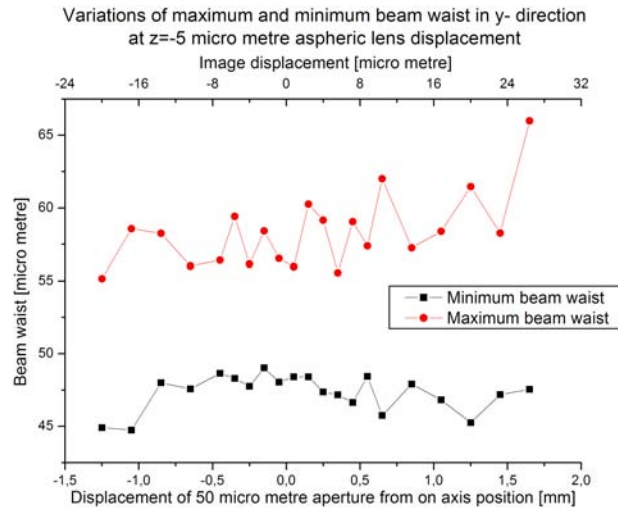


Figure 6.32: Maximum and minimum beam waists as a function of y- displacement with aspheric lens $z = -5 \mu\text{m}$ displaced.

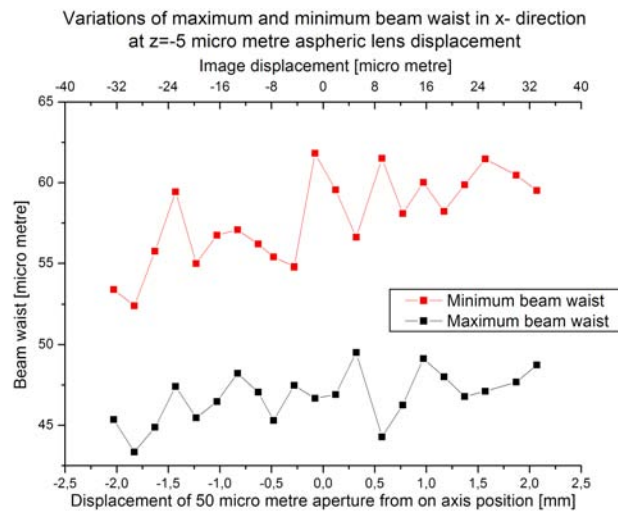


Figure 6.33: Maximum and minimum beam waists as a function of x- displacement with aspheric lens $z = -5 \mu\text{m}$ displaced.

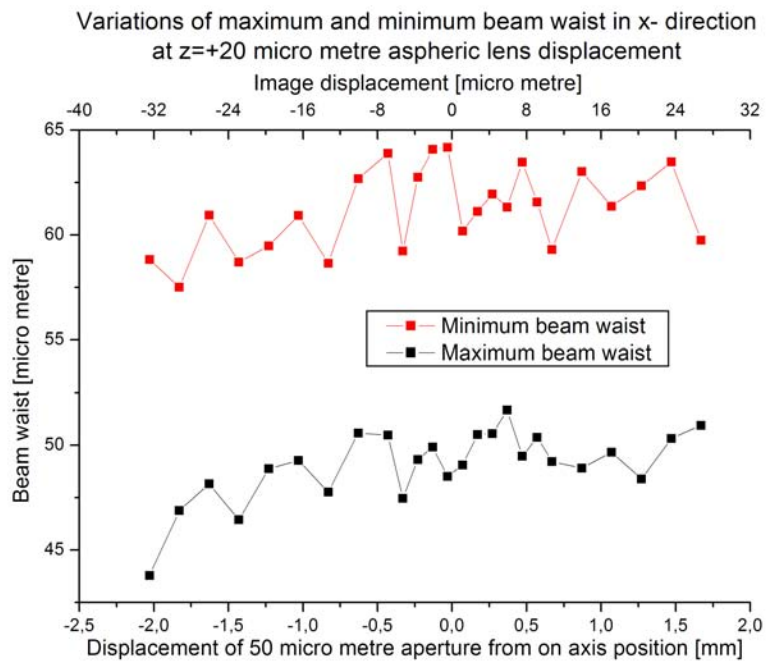


Figure 6.34: Maximum and minimum beam waists as a function of x- displacement with aspheric lens $z = +20 \mu\text{m}$ displaced.

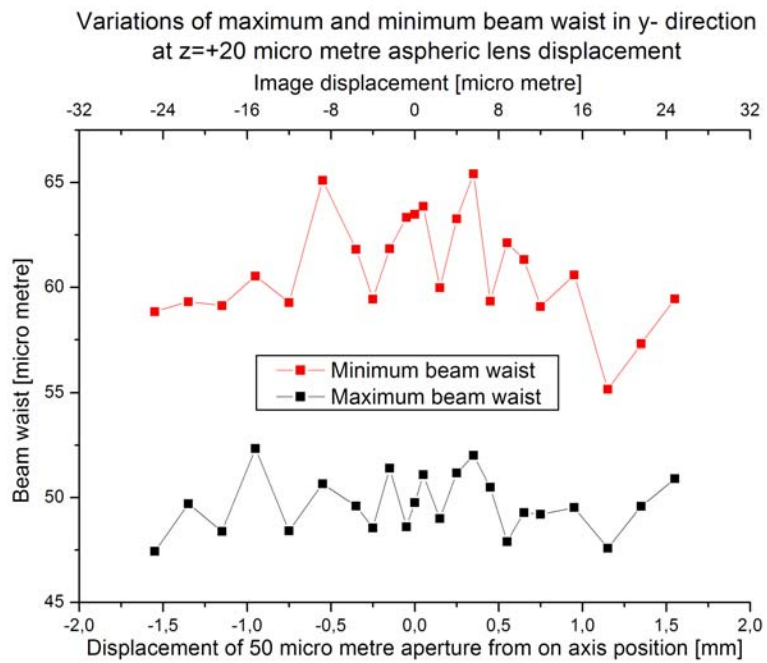


Figure 6.35: Maximum and minimum beam waists as a function of y- displacement with aspheric lens $z = 20 \mu\text{m}$ displaced.

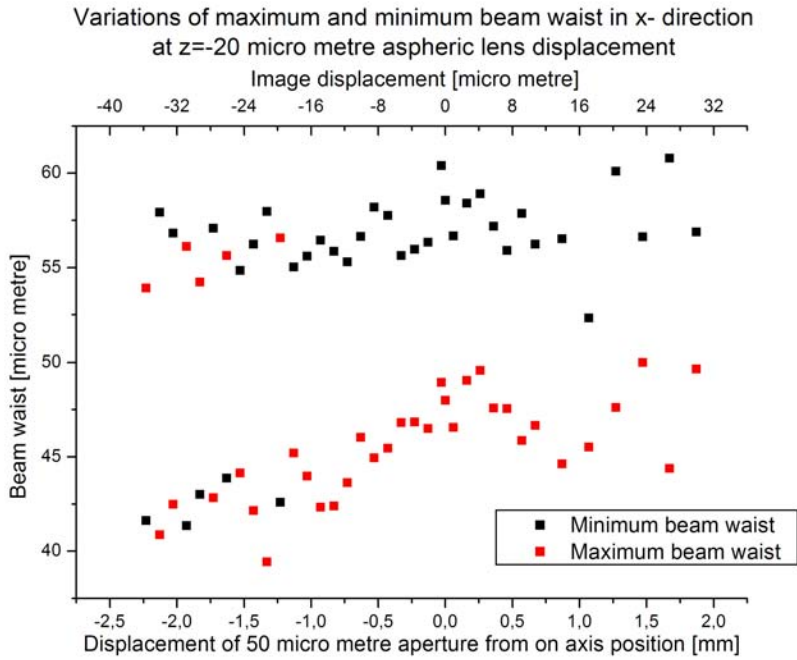


Figure 6.36: Maximum and minimum beam waists as a function of x- displacement with aspheric lens $z = -20 \mu\text{m}$ displaced. For some of the negative values our fitting routine had some problems to distinguish between the different waists once more, thus we did not join the various points with lines, as it is easier to see the real association without them.

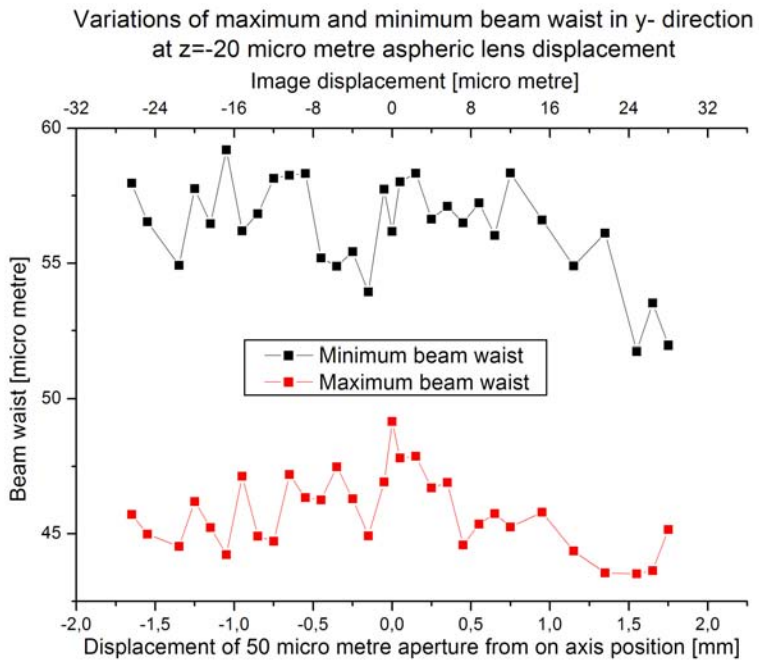


Figure 6.37: Maximum and minimum beam waists as a function of y- displacement with aspheric lens $z = -20 \mu\text{m}$ displaced.

Bibliography

- [1] H. J. Metcalf, P. v. d. Straten "Laser trapping and cooling" Springer Verlag 1999 ISBN 0-387-98728-1
- [2] C. Foot "Atomic physics" Oxford University Press 2006 ISBN 0-19-850696-1
- [3] F. Schwabl "Quantenmechanik 1" Springer Verlag 2004 ISBN 3-540-43106-3
- [4] F. Schwabl "Statistische Mechanik und Thermodynamik" 2006 2006 ISBN 3-540-31095-9
- [5] Y. Sortais, H. Marion, C. Tuchendler, Y. Lance, M. Lamare, P. Fournet, C. Armellin, R. Mercier, G. Messin, P. Granier "Diffraction- limited optics for single atoms manipulation" Physicsl Review A Vol. 75, pp. 01346-(1-7) 2007
- [6] E. Hecht "Optics" Addison Wesley 2003 ISBN 0321188780
- [7] Born and Wolf "Priciples of optics" Cambridge University Press ISBN 0-521-64222-1
- [8] C. S. Adams, E. Riis "Laser cooling and trapping of neutral atoms" Prog. Quant. Electr. Vol. 21, No. 1, pp. 1-79 1997
- [9] C. Cohen- Tannoudji "Laser cooling and trapping of neutral atoms: theory" Physics reports 219 Nos. 3-6, pp. 153- 164 1992
- [10] J. Dalibard, C. Cohen- Tannoudji "Laser cooling below the Doppler limit by polarisation gradients - Simple theoretical- models" J. Opt. Soc. Am. B Vol. 6, pp. 2023 - 2045 1989
- [11] Siegman "Lasers" University Science Books 1990 ISBN 0-935702-11-3
- [12] S. Kuppens, K. Corwin, K. Miller, T. Chupp, C. Wieman "Loading an optical dipole trap" Physical Review A Vol. 62, pp. 013406-(1-13) 2000
- [13] N. Schlosser, G. Reymond, I. Protsenko, P. Grangier "Sub- poissonian loading of single atoms in a microscopic dipole trap" Nature Vol. 411 pp. 1024- 1027 2001
- [14] N. Schlosser, G. Reymond, P. Grangier "Collisional blockade in microscopic optical dipole traps" Physical Review Letters Vol. 89, No. 2, pp. 023005-(1-4) 2002
- [15] Thorlabs AC508-750-B Spreadsheet available at: <http://www.thorlabs.com>

- [16] Asphericon 15-12HPX-B Spreadsheet available at: <http://www.asphericon.net>
- [17] Toptical DL- 100 diode laser Spreadsheet available at: <http://www.toptica.de>
- [18] Conrad CCD camera spreadsheet available at: <http://www.conrad.de>
- [19] Thorlabs LA- 1805 - B Spreadsheet available at: <http://www.thorlabs.com>
- [20] Thorlabs AC - 508 - B Spreadsheet available at: <http://www.thorlabs.com>
- [21] Thorlabs LA - 1484 - B Spreadsheet available at: <http://www.thorlabs.com>
- [22] Thorlabs LA - 1433 - B Spreadsheet available at: <http://www.thorlabs.com>
- [23] Thorlabs LA - 1509-B Spreadsheet available at: <http://www.thorlabs.com>
- [24] Photonic Solutions PBS:0201-780 <http://www.psplc.com/>
- [25] L. Novotny, B. Hecht "Principles of nano-optics" Cambridge University Press 2006 ISBN 0-521-83224-1
- [26] Goodman "Introduction to Fourier Optics" Roberts and Company Publishers 2005 0-9747077-2-4
- [27] <http://www.npl.co.uk>
- [28] <http://webphysics.davidson.edu>
- [29] <http://www.physics.ox.ac.uk/>